

**UCLA**

**UCLA Electronic Theses and Dissertations**

**Title**

Human Brain Glutamate, Glutamine,  $\gamma$ -Aminobutyric Acid Proton Magnetic Resonance Spectral Quantification with the Fast Pade Transform

**Permalink**

<https://escholarship.org/uc/item/1np12339>

**Author**

Zhang, Jingjing Michele

**Publication Date**

2013

Peer reviewed|Thesis/dissertation

UNIVERSITY OF CALIFORNIA

Los Angeles

Human Brain Glutamate, Glutamine,  $\gamma$ -Aminobutyric Acid

Proton Magnetic Resonance

Spectral Quantification with the Fast Padé Transform

A dissertation submitted in partial satisfaction of the

requirements for the degree Doctor of Philosophy

in Biomedical Physics

by

Jingjing Michele Zhang

2013

© Copyright by

Jingjing Michele Zhang

2013

# ABSTRACT OF THE DISSERTATION

Human Brain Glutamate, Glutamine,  $\gamma$ -Aminobutyric Acid

Proton Magnetic Resonance

Spectral Quantification with the Fast Padé Transform

by

Jingjing Michele Zhang

Doctor of Philosophy in Biomedical Physics

University of California, Los Angeles, 2013

Professor Jeffrey R. Alger, Chair

Glutamate, glutamine, and  $\gamma$ -Aminobutyric acid play important excitatory and inhibitory messenger role in neuronal signal transmissions. Perturbations in the delicate homeostatic balances between these three neurometabolites have significant implications in various psychiatric disorders. Proton magnetic resonance spectroscopy is a non-invasive analytical technique that allows the detection and quantification of *in vivo* chemical compound concentrations under the image guidance of MRI. A variety of MRS acquisition methods have been employed in the past to study the GABAergic and glutamatergic systems in the human brains, sometimes with conflicting reports in the metabolite levels. The variability in findings is



likely caused by the methodology differences in acquisition and quantification steps of these studies. In this thesis, I performed quantum mechanical based numerical simulations to investigate how the LCModel quantification accuracy varies with different acquisition parameters and baseline signals. The simulation results show that Gln cannot be reliably measured at 1.5 T and 3 T with the PRESS acquisition and the Spin Echo method. Glu can be reliably measured at 1.5 T, 3 T, and 7 T with both the PRESS and Spin Echo method. I also applied the MEGA-PRESS pulse sequence to measure GABA concentrations in both phantoms and healthy human controls. Two MRS quantification methods were used to quantify the C4 GABA resonances with the edited spectra. The results show that both the LCModel and peak integration techniques offer similar inter-subject CV in GABA signal quantifications. I also present a novel post-processing technique called the Fast Padé Transform to investigate its feasibility and accuracy as an alternative method to measure glutamate, glutamine, and GABA in human brains. The results show that the FPT algorithm is capable of quantifying resonance peaks of GABA, tNAA, tCr, and tCho with good agreement to the LCModel method, but there is no indication that FPT produces more accurate or precise concentrations. Performance of the FPT algorithm for Glu and Gln quantification is inferior to LCModel quantification.

The dissertation of Jingjing Michele Zhang is approved.

Katherine L. Narr

M. Albert Thomas

Jennifer Levitt

Joseph O'Neill

Henry Huang

Jeffery R. Alger, Committee Chair

University of California, Los Angeles

2013

I dedicate this dissertation to my fiancé Andrew B. Hurkett.

## Table of Contents

<b>Chapter 1 Glutamate, Glutamine, and GABA .....</b>	<b>1</b>
<b>Introduction .....</b>	<b>1</b>
<b>Neurotransmitters .....</b>	<b>2</b>
Glutamate .....	3
Glutamine .....	5
$\gamma$ -Aminobutyric Acid.....	6
Glutamate-Glutamine-GABA Cycle .....	8
<b>Implications in Psychiatric Disorders .....</b>	<b>9</b>
Major Depressive Disorder .....	10
Autism Spectrum Disorder .....	11
<b>Conclusion.....</b>	<b>12</b>
<b>References.....</b>	<b>13</b>
<b>Chapter 2 <math>^1\text{H}</math> Magnetic Resonance Spectroscopy.....</b>	<b>17</b>
<b>Basic Principles .....</b>	<b>17</b>
Introduction.....	17
Chemical Shift .....	18
Fourier Transform.....	19
Lineshape.....	20
Phase.....	21
J coupling .....	22
<b>MRS Signal Acquisition .....</b>	<b>24</b>
MR Pulse Sequence.....	24
PRESS .....	25
CSI .....	26
PEPSI.....	27
<b>References.....</b>	<b>28</b>
<b>Chapter 3 <math>^1\text{H}</math>-MRS of the Human Brain .....</b>	<b>30</b>
<b>Introduction .....</b>	<b>30</b>
<b><math>^1\text{H}</math>-MRS of Glu, Gln, and GABA .....</b>	<b>34</b>
Glutamate .....	34
Glutamine .....	34
GABA.....	36
<b>Spectral Quantification.....</b>	<b>37</b>
Overview.....	37
LCModel.....	38
<b><math>^1\text{H}</math>-MRS in Psychiatric Disorders .....</b>	<b>42</b>
Depression .....	42
Autism Spectrum Disorder .....	44
<b>Conclusion.....</b>	<b>45</b>
<b>References.....</b>	<b>46</b>

<b>Chapter 4 PEPSI Investigation in Children and Adolescents with Attention Deficit Hyperactivity Disorder .....</b>	<b>50</b>
<b>Introduction .....</b>	<b>50</b>
<b>Methods and Materials .....</b>	<b>52</b>
MRI/MRS Acquisition.....	52
Post-processing.....	53
Subjects.....	56
Statistical Analysis.....	57
<b>Results .....</b>	<b>57</b>
<b>Discussions .....</b>	<b>61</b>
<b>Conclusions.....</b>	<b>62</b>
<b>References.....</b>	<b>62</b>
<b>Chapter 5 Human Brain <sup>1</sup>H MR Spectral Simulation .....</b>	<b>66</b>
<b>Introduction .....</b>	<b>66</b>
<b>Methods and Materials .....</b>	<b>69</b>
Pulse Sequence Simulations.....	69
Spectra Simulation and Quantification.....	70
<b>Results.....</b>	<b>71</b>
SNR vs. SD.....	71
Linewidth vs. SD .....	72
Baseline vs. SD.....	73
<b>Discussions .....</b>	<b>73</b>
<b>Conclusions.....</b>	<b>75</b>
<b>References.....</b>	<b>88</b>
<b>Chapter 6 J-difference Editing for GABA .....</b>	<b>89</b>
<b>Introduction .....</b>	<b>89</b>
<b>J-difference Editing .....</b>	<b>91</b>
Overview of MEGA-PRESS.....	91
Siemens WIP.....	92
<b>GABA Resonance Quantification.....</b>	<b>93</b>
LCModel.....	93
Peak Integration .....	95
<b>Phantom Study .....</b>	<b>95</b>
Methods.....	95
Results.....	97
<b>In vivo Study .....</b>	<b>100</b>
Methods.....	100
Results.....	101
<b>Discussions .....</b>	<b>101</b>
<b>Conclusions.....</b>	<b>102</b>
<b>References.....</b>	<b>103</b>

<b>Chapter 7 A Padé Approximant Method for the Analysis of Proton Magnetic Resonance Spectroscopy Signals of the Human Brain.....</b>	<b>106</b>
<b>Introduction .....</b>	<b>106</b>
<b>Theory .....</b>	<b>107</b>
<b>Froissart Doublet.....</b>	<b>110</b>
<b>Software .....</b>	<b>111</b>
<b>Validation with Simulation.....</b>	<b>113</b>
<b>Validation with Phantoms .....</b>	<b>117</b>
<b>Comparison with LCModel.....</b>	<b>119</b>
<b>Glutamate, Glutamine, and GABA.....</b>	<b>121</b>
<b>Conclusions.....</b>	<b>125</b>
<b>References.....</b>	<b>125</b>

## List of Figures

Figure 1-1: Glutamatergic neurotransmission. ....	4
Figure 1-2: Glutamate-glutamine cycle. ....	5
Figure 1-3: GABAergic neurotransmission. ....	7
Figure 1-4: The Glutamate-Glutamine-GABA cycle. ....	9
Figure 2-1: Chemical shift of water and fat. ....	19
Figure 2-2: Time and frequency domain NMR signal. ....	20
Figure 2-3: Absorption and dispersion mode NMR spectrum. ....	21
Figure 2-4: Absorption and dispersion mode spectra with phase shifts. ....	22
Figure 2-5: Proton NMR spectrum of ethanol. ....	23
Figure 2-6: Pulse sequence diagram for single voxel PRESS acquisition. ....	25
Figure 2-7: Pulse sequence diagram of 2D CSI. ....	27
Figure 2-8: Pulse sequence diagram of 2D PEPSI acquisition. ....	28
Figure 3-1: Simulated brain proton NMR spectrum with PRESS TE 30 ms acquisition at 3 T... 32	32
Figure 3-2: Macromolecule baseline obtained from an inversion recovery acquisition in rat brain at 9.4 T. ....	33
Figure 3-3: Chemical structure and simulated proton NMR spectrum of glutamate. ....	34
Figure 3-4: Chemical structure and simulated proton NMR spectrum of glutamine. ....	35
Figure 3-5: Simulated proton spectra of glutamate and glutamine with PRESS TE 30 ms acquisition at 3T. ....	36
Figure 3-6: Simulated proton NMR spectrum of GABA. ....	37
Figure 3-7: An example output file from the LCModel software. ....	41

Figure 4-1: PEPSI slice placements in using a 3D whole brain T1-weighted MRI acquisition. ..	52
Figure 4-2: FreeSurfer VOIs overlaying T1-weighted MPRAGE images and the corresponding PEPSI acquisition volume.....	54
Figure 4-3: FSL FAST tissue segmentation and PEPSI acquisition volumes. ....	55
Figure 4-4: An example of the LCModel fitted PEPSI spectrum at the basal ganglia region.....	60
Figure 4-5: Histogram and density plots of the total choline concentration distribution between ADHD and healthy controls in the left posterior cingulate cortex. ....	61
Figure 5-1: VeSPA simulation software user interface. ....	76
Figure 5-2: VeSPA Priorset user interface.....	76
Figure 5-3: VeSPA simulated 1H MR spectrum with different levels of Gaussian noise with PRESS TE 30 at 3 T. ....	77
Figure 5-4: An example of LCModel analyzed VeSPA simulated MR spectrum with PRESS TE 80 at 3 T. ....	78
Figure 5-5: CRLB values of Glu, Gln, and GABA verses SNR at 1.5 T and 7 T .....	79
Figure 5-6: CRLB values of Glu, Gln, and GABA verses SNR at 3 T .....	80
Figure 5-7: CRLB values of tNAA, tCho, and tCr verses SNR. ....	81
Figure 5-8: CRLB values of tNAA, tCho, and tCr verses SNR at 3 T. ....	82
Figure 5-9: VeSPA Priorset simulated MR spectra with increasing linewidth values. ....	83
Figure 5-10: CRLB values of Glu, Gln, GABA, tNAA, tCho, and tCr verses linewidth.....	84
Figure 5-11: Simulated PRESS TE 30 spectra at 3T with added Gaussian noise and seven baseline signals. ....	85
Figure 5-12: Signal amplitudes of Glu, Gln, GABA, tNAA, tCho, and tCr verses baseline signals .....	86
Figure 5-13: Glu, Gln, and GABA LCModel %SD vs. SNR and linewidth at 3 T using single voxel TE 30 PRESS acquisition. ....	87
Figure 6-1: GABA C-2, C-3 and C-4 proton resonances are overlapping with Glu, NAA, and tCr signal peaks.....	90
Figure 6-2: Schematic diagram of MEGA-PRESS editing for 3-ppm GABA triplet signals. ....	92



Figure 6-3: Pulse sequence diagram of MEGA-PRESS acquisition with CHESS water suppression.....	93
Figure 6-4: An example of the LCModel fitted human brain MEGA-PRESS spectrum. ....	94
Figure 6-5: MEGA-PRESS acquisition on a phantom with 8 mMol of GABA.....	97
Figure 6-6: Braino phantom metabolite concentration measurement with TE 30 PRESS and MEGA-PRESS 'edit-off' TE 68 acquisition.....	98
Figure 6-7: GABA concentrations in phantoms .....	99
Figure 6-8: MEGA-PRESS single voxel acquisition in human brain in vivo at 3 T and its J-difference spectrum.....	100
Figure 6-9: GABA concentrations in ten human subjects and the measurement correlation between the LCModel and the peak integration method. ....	101
Figure 7-1: Froissart doublets present in the FPT analysis of in vivo MR spectrum from TE 30 PRESS acquisition .....	112
Figure 7-2: A flowchart diagram of the FPT algorithm implemented in MATLAB.....	113
Figure 7-3: PRESS simulated MRS frequency domain magnitude spectra at 3 T without noise, with noise SNR = 20, and the Froissart doublet denoised FPT spectrum. ....	115
Figure 7-4: Linear relationship between data SNR and the Zero-Pole Distance.....	115
Figure 7-5: FPT algorithm measurement percentage errors using simulated brain MR spectra at 3 T with TE 30 PRESS pulse sequence. ....	116
Figure 7-6: FPT algorithm measurement percentage errors using simulated brain MR spectra at 3 T with TE 30 PRESS pulse sequence. ....	117
Figure 7-7: FPT measured metabolite concentrations in Braino phantom. ....	118
Figure 7-8: FPT measured GABA concentrations in four phantoms with 4 to 20 mMol of GABA. ....	119
Figure 7-9: Single voxel PRESS acquisition at the AC region and the proton MR spectrum....	120
Figure 7-10: An example 3T TE 30 PRESS in vivo Padé component shape spectrum generated by the FPT algorithm .....	120
Figure 7-11: Comparison between FPT and LCModel measured mean concentration values for total NAA, total Cr and total Cho. ....	121
Figure 7-12: Bland-Atman correlation test between the FPT algorithm and LCModel. ....	121
Figure 7-13: FPT measured Glu values across ten healthy subjects.....	122

Figure 7-14: FPT measured Gln values across ten healthy subjects..... 122

Figure 7-15: An example of the Padé shape spectrum of an in vivo J-difference spectrum. .... 124

Figure 7-16: GABA concentration values measured by the FPT algorithm in comparison with values measured by LCModel and Peak Integration ..... 124

## List of Tables

Table 1-1: Neurotransmitter classification.....	2
Table 1-2: Chemical structure of glutamate, glutamine, and GABA .....	3
Table 3-1: <sup>1</sup> H Chemical shifts of neurometabolites and their in vivo concentrations. ....	31
Table 4-1: Anatomical VOIs and their cutoff values for each slab. ....	55
Table 4-2: SUPV, AC, and BG Slab metabolite level of ADHD and healthy control subjects. ..	58
Table 4-3: SUPV, AC, and BG Slab Glu, Glx, and Myo levels of ADHD and healthy control subjects.....	59
Table 5-1: Field Strength and TE values chosen for simulations. ....	76
Table 7-1: Summary of the relationships between dk, Ωk and MRS parameters for the kth metabolite.....	108
Table 7-2: Summary of the mean, standard deviation, and coefficient of variation values for the MEGA-PRESS GABA quantification made by the FPT, LCModel, and Peak Integration methods. ....	123

## ACKNOWLEDGEMENTS

The journey of completing my doctoral thesis has been a long and emotional endeavor. I am deeply grateful for the valuable guidance and unconditional support of my advisor, Dr. Jeffrey R. Alger. I must also express my sincere gratitude to Dr. Katherine Narr and Dr. Roger Woods. Without their constant trust and encouragement, this thesis would not have come to fruition. I would also like to thank Dr. Jennifer Levitt, Dr. Joseph O'Neill, and Dr. Karl Goodkin for their interim supports and supervisions in the first and second year of my projects.

The Ahmanson-Lovelace Brain Mapping Center has been a wonderful community for me to conduct my research projects. I am particularly grateful to Dr. Andy Frew, James Widanta, Marry Susselamn, Trent Thixton, Dr. JJ Wang and Dr. Liron Yan, and I own special thanks to Elizabeth Pierce. The personal and professional relationships that were built at the center will forever stay with me.

I would like to also acknowledge the helps and supports from Dr. Jonathon Furuyama, Ronald Ly and Victor Yee. I sincerely thank the faculties and the student affair officers at the department of Biomedical Physics. I thank 'Mike', my program director, for his valuable guidance and teaching through out all these years.

Last, but not least, I am very much indebted to my fiancé Andrew Hurkett, who has been my never-ending source of unconditional supports, love, and laughs. I dedicate this thesis to you, my love, without you, the completion of this thesis would not have been possible.

## VITA

### Education

M.S. **University of California, Los Angeles;**

*Master of Science in Biomedical Physics; December 2009*

B.A. **Auburn University;**

*Bachelor of Science in Physics; Magna Cum Laude, December 2006*

### Awards and Honors

The National Physics Honor Society Sigma Pi Sigma	2006
ISMARM Student Travel Award	2008
Biomedical Physics Student Travel Award	2011/2012
UCLA Annual Neurology Science Day Poster Award	2012
UCLA Dr. Ursula Mandel Fellowship	2012

### Publications and Presentations

- “Regular and Chaotic Motion of Anti-protons Through a Nested Penning Trap with Multipole Magnetic Fields” *C. L. Taylor, **Jingjing Zhang**, F. Robicheaux. J. Phys. B: At. Mol. Opt. Phys.* 39 4945, 2006
- “Cooling of Rydberg H-bar during Radiative Cascade” **Jingjing Zhang**, *C. L. Taylor, and F. Robicheaux. J. Phys. B: At. Mol. Opt. Phys.* 40 1019, 2006
- “Short-TE 2D Proton Echo Planar Spectroscopic Imaging (PEPSI) in Adolescents with

Attention-Deficit Hyperactivity Disorder" **Jingjing Zhang**, *et al. Medical Physics*, Vol. 38  
No. 6, 2011

- “Optimal Methodology for Glutamate and Glutamine Signal Quantification with Single Voxel MRS of the Human Brain" **Jingjing Zhang**, *S. Sheriff, A. A. Maudsley, K. Goodkin, J. R. Alger In: Proceedings of the 19<sup>th</sup> Annual Meeting of ISMRM, Montreal, Canada, 2011*
- “Neurochemical Changes in the Anterior Cingulate Cortex Mirror ECT Treatment Response in Major Depression” **Jingjing Zhang**, *K. L. Narr, R. P. Woods, O. R. Phillips, J. R. Alger, R. T. Espinoza. Molecular Psychiatry, in press, 2012*
- “Clinical utility of magnetic resonance spectroscopy to enhance diagnosis of HIV-associated mild neurocognitive disorder” *K. Goodkin, J. R. Alger, A. A. Maudsley, V. Govind, S. Sheriff, Jingjing Zhang, Neuropsychiatry 2:5, 379-383, 2012*

# Chapter 1 Glutamate, Glutamine, and GABA

## Introduction

Ancient Greeks believe that the human heart controls our consciousness and it is the heart that suffers from pain and melancholy. Unfortunately, modern sciences offer little sympathy towards this belief. The human brain, as the central command for both the physical body and our mental processes, can be viewed as a network of complex electrical circuits, with neurons serving as its principal communication subunits and neurotransmitters working as its chemical messengers. Any disruption in this complex biological communication system gives rise to abnormal psychological and behavioral pattern that deviates from what is commonly accepted as the state of normal. It is the goal of this dissertation to offer potential understanding and guidance in the detection and quantification of three of these chemical messengers, glutamate, glutamine, and gamma-Aminobutyric Acid (GABA), using a non-invasive analytical technique called the Magnetic Resonance Spectroscopy (MRS).

The work for this dissertation is three-fold. First, I performed quantum mechanical based computer simulations on two of the MR pulse sequences available at the UCLA Brain Mapping Center where I worked as a graduate student. The goal of the simulations is to generate MR spectra close to the experimental spectra collected *in vivo* so that they may serve as ground truths for signal quantification processes. The quantification results and measurement errors in return serve as the comparison standard for different MR acquisition methods at various magnetic field strengths and values of echo time (TE). Then, I compared simulation results with data collected from actual *in vivo* studies to validate my hypotheses. For the last part of my dissertation, I have implemented and validated a novel MR spectral quantification algorithm to investigate its

potential accuracy in the measurements of neurometabolite concentrations, especially the concentration measurements for glutamate, glutamine, and GABA.

This chapter introduces the biological concepts for neurotransmitters and their functions in the human brain, and overviews of how glutamate, glutamine, and GABA *in vivo* concentration are affected in psychiatric disorders, including the Major Depressive Disorder and the Autism Spectrum Disorder.

## Neurotransmitters

There are many different types of neurotransmitters, but they all more or less function as signal exchange messengers between neurons. Each neuron can produce one or more different kinds of neurotransmitters, which can be released at various frequencies during cell signaling. Neurotransmitters can be classified by their chemical structure as well as by their functions. Table 1-1 lists some of the important neurotransmitters and their classifications. Chemically, neurotransmitters can be divided into six categories, namely acetylcholine, amino acids, neuropeptides, monoamines, gases and lipids, and purines. Functionally, they can be classified into inhibitory and excitatory neurotransmitters. Due to the scope of this study, only three of the neurotransmitters of interest will be discussed in this chapter.

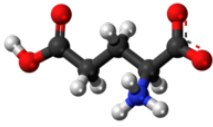
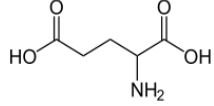
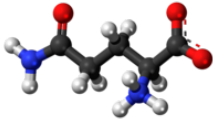
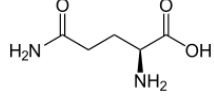
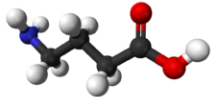
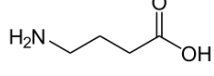
<i>Chemical Classification of Neurotransmitters</i>	
Acetylcholine	Acetylcholine
Amino Acids	<b>Glutamate, GABA, Aspartate</b>
Neuropeptides	Endorphin, Somatostatin
Monoamines	Serotonin, Dopamine, Norepinephrine, Epinephrine
Purines	Adenosine
Gases and Lipids	Nitric Oxide, Carbon Monoxide
<i>Functional Classification of Neurotransmitters</i>	
Inhibitory (Hyperpolarization)	<b>GABA</b>
Excitatory (Depolarization)	<b>Glutamate</b>

**Table 1-1: Neurotransmitter classification.**



## Glutamate

Glutamate (Glu) or glutamic acid is the most abundant excitatory neurotransmitter in the mammalian central nervous system. It is considered to be the principal excitatory neuronal signaling transmitter for many important normal brain functions, including memory, learning, and cognition (Platt, 2007). Table 1-2 lists its detailed chemical formula and structure. Glu has a 5-carbon chain structure with two carboxyl groups, two methylene groups, one methine group, and one amine functional group.

Ball-and-stick Model	Chemical Structure	Molecular Formula
		<b>Glutamate</b> (C <sub>5</sub> H <sub>9</sub> NO <sub>4</sub> )
		<b>Glutamine</b> (C <sub>5</sub> H <sub>10</sub> N <sub>2</sub> O <sub>3</sub> )
		<b>GABA</b> (C <sub>4</sub> H <sub>9</sub> NO <sub>2</sub> )

**Table 1-2: Chemical structure of glutamate, glutamine, and GABA**

Glu in human brain tissue is ubiquitous. Approximately 5-15 mMol/kg of Glu is present in the neuronal cytoplasm (Osen et al, 1995; Danbolt, 2001). The axon terminals of a neuron contain 2-3 times higher Glu concentration than the neuron cell bodies as well as the dendrites (Ottersoen, 1989). This localization of Glu distribution at the axon terminals is due to the involvement of mitochondria during Glu synthesis (Fisher, 2007). Namely, Glu is produced inside of the mitochondria, which are centrally located at axon terminals. After synthesis, Glu is packed away neatly inside of synaptic vesicles to a concentration of 100 mMol or more (Shupliakov et al, 1992). When the synaptic vesicles fuses with the presynaptic plasma membrane,

Glu is released into the synaptic cleft and is free to interact with nearby postsynaptic receptors, which in turn triggers subsequent intracellular second-messenger cascades (Shown in Figure 1-1).

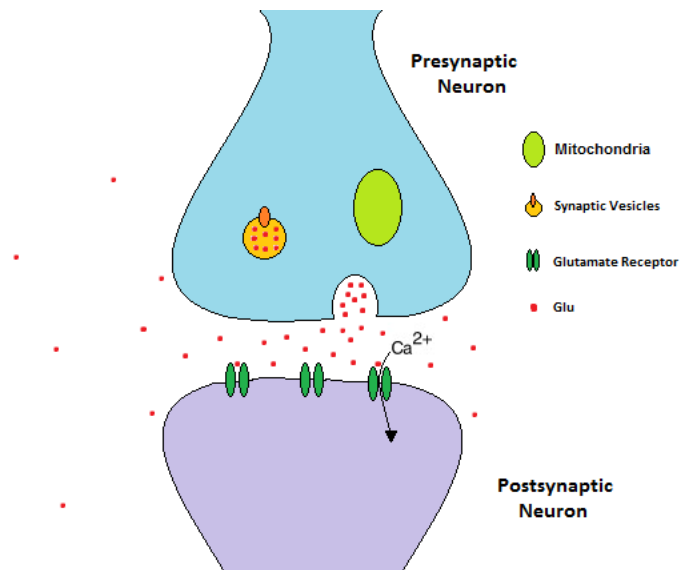


Figure 1-1: Glutamatergic neurotransmission.

Release of Glu by one synaptic vesicle creates one excitatory postsynaptic potential (EPSP) event (Meldrum, 2000). An excitatory postsynaptic electrical current is generated by the depolarization of postsynaptic cell membrane potential, causing the influx of cations (Ca<sup>2+</sup>) into the cell body. When several synaptic vesicles containing Glu are released simultaneously, multiple excitatory postsynaptic potential events will be triggered. The summation of these events can generate an action potential across an entire neuron when the neuron's trigger threshold is reached. Action potentials or nerve impulses are all-or-nothing events that can propagate cell signals over both short and long distances. The binary information exchange between neurons can be carried out by either fast synaptic potentials or slow synaptic potentials (Nolte, 2009). Fast synaptic transmissions are used for rapid cell-to-cell communications by simply opening and closing the ligand operated ion channels; slow synaptic transmissions on the other hand are much complicated in nature and require facilitation of many proteins and secondary messengers in complex orders of biochemical processes (Greengard, 2001).

## Glutamine

Glutamine (Gln) is a non-essential amino acid present in the human brain, but it is an important immediate precursor of the major excitatory neurotransmitter Glu. Table 1-2 lists its detailed chemical formula and structure. Very similar to Glu in chemical structure, Gln also has a 5-carbon chain structure with two methylene groups, one methine group, one amine group, one carboxyl group, and an amide functional group, which is absent in the Glu.

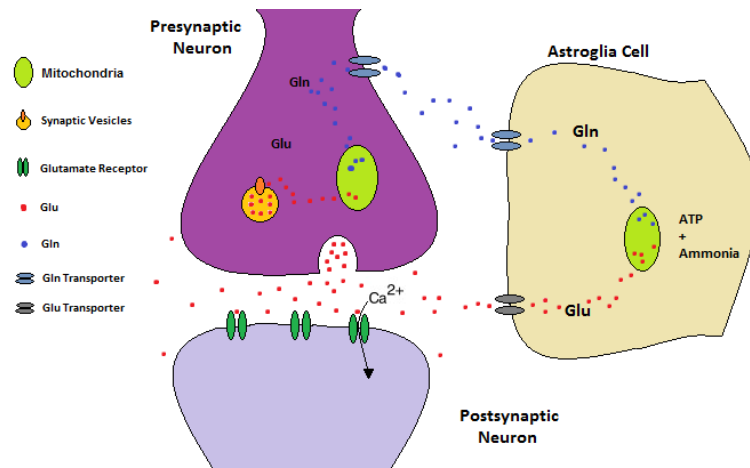


Figure 1-2: Glutamate-glutamine cycle.

Glu is synthesized from glucose in nearly all cells in the human body other than in neurons (Bak et al. 2006). This is due to the lack of pyruvate carboxylase in neurons (Patel 1974; Shank et al. 1985; Hertz et al. 1999). The inability of *de novo* synthesis of Glu in neurons causes the formation of an important neuronal Glu resupply pathway via the glutamate-glutamine cycle (illustrated in Figure 1-2). After Glu has been released into the synaptic cleft by the presynaptic neuron, excess Glu is actively transported into the astroglial cells by glutamate transporters. This process ensures that the Glu concentration in the extracellular space remains at the ideal 1  $\mu\text{Mol}$  level (Anderson and Swanson 2000), since excessive amounts of Glu can cause excessive neurotransmission, which can in turn result in extra calcium cation influx into the neurons and eventually causes cell death (Platt 2007). Astrocytes synthesize Gln from Glu via enzyme

glutamine synthetase and then actively transport Gln back into the extracellular space. This cycle prevents excessive Glu-driven neurotransmission because Gln does not activate postsynaptic Glu receptors. The cycle is completed by transport of Gln into the presynaptic neurons and into mitochondria where Glu is resynthesized with ammonia being formed as a byproduct (Cooper 2001). This recycling process not only assures the replenishment of Glu transmitters in the cytoplasm for subsequent presynaptic secretion and signal transmission, but also lowers the excitotoxicity caused by the high Glu concentration level in the extracellular space. Another important function of the glutamate-glutamine cycle is detoxification (Cooper 2001). Ammonia is toxic to the central nervous system. The formation of Gln from Glu and ammonia by astrocytes will reduce the amount of ammonia and lower its cytotoxicity by maintaining proper ammonia homeostasis. The synthesis of Gln from Glu by astrocytes requires energy derived from ATP. The glutamate-glutamine cycle consumes approximately 80% of the energy produced by the glucose oxidation process in the human brain cortex (Rothman 1999).

### **$\gamma$ -Aminobutyric Acid**

$\gamma$ -Aminobutyric Acid (GABA) is the major inhibitory neurotransmitter in the adult human brain. GABA is also a non-essential amino acid and has very specific neurotransmission functions. Table 1-2 lists its detailed chemical formula and structure. Structurally very similar to Glu and Gln, GABA also has a 5-carbon chain structure with one carboxyl group, one amine group, and three methylene functional groups. Most prominent functions of GABA include motor control, visual sensory, and anxiety regulation.

Neurons can be functionally classified as being inhibitory or excitatory. Inhibitory neurons and their synapses typically use GABA as the major transmitter and they are known as GABAergic neurons; excitatory neurons and their synapses use Glu as the major transmitter and

they are known as Glutamatergic neurons (Nolte 2007 page 192). GABA is synthesized by the GABAergic neurons, which accounts for about 25%-40% of the neurons in the brain (Li and Xu 2008). Glu is the principal precursor for GABA. GABA is produced through the process of decarboxylation of Glu with glutamate decarboxylase (CAD), which removes one carboxyl group from the Glu side chain.

The GABAergic neurotransmission is responsible for the postsynaptic inhibition activity. Namely, the GABA filled vesicles travel to the presynaptic membrane and release GABA into the synaptic cleft. The unbound GABA will either interact with GABA receptors located on the postsynaptic membrane or be transported into nearby neurons and astrocytes. GABA binding to postsynaptic transmembrane receptors opens up ion channels, leading to either anion influx or cation efflux (shown in Figure 1-3). Both actions will cause the hyperpolarization of postsynaptic membrane and inhibit the influx of calcium cations, which will result in decreased probability for a neuron to reach the action potential threshold.

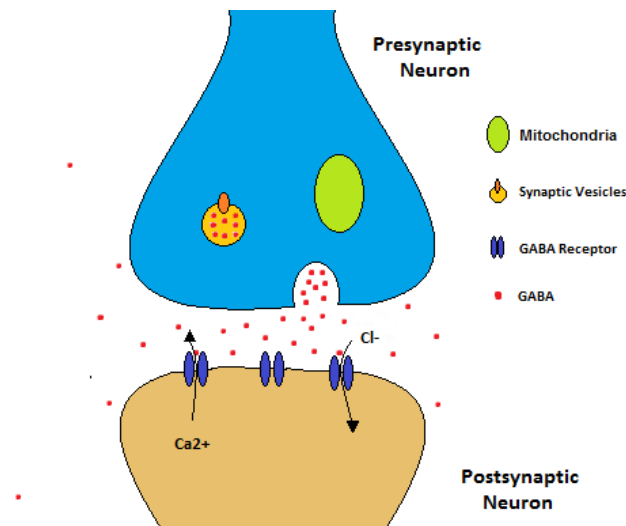


Figure 1-3: GABAergic neurotransmission.

Surprisingly, even though GABA is the major inhibitory neurotransmitter in the adult brain, it is believed to actually function as the primary excitatory neurotransmitter in the prenatal

and early postnatal brain. In the early developing mammalian brain, the concentration of chloride anion (Cl<sup>-</sup>) is higher in the intracellular space than the extracellular space. As the brain matures, the concentration of Cl<sup>-</sup> becomes lower in the intracellular space than the extracellular space (Miles 1999). The alteration of Cl<sup>-</sup> concentration levels in the developing central nervous system is hypothesized as the cause of the dramatic role switch for GABA (Rivera et al. 1999). Since GABAergic neurons mature faster than the glutamatergic neurons in some regions of the brain, GABA will serve as the primary excitatory neurotransmitter before Glu in the still developing CNS.

### Glutamate-Glutamine-GABA Cycle

In the GABAergic neurons, Glu facilitates the production of GABA. However, neurons are incapable of Glu synthesis *de novo*, the production of Glu requires the assistance of Gln. Gln on the other hand is transported into the interneurons after its creation in the astrocytes from Glu and ammonia with the purpose of producing GABA. This seemingly closed-loop feedback process suggests that GABAergic neurons require the presence of astrocytes to maintain a balanced supply of GABA transmitters, even though the majority of the GABA transmitters are reabsorbed by the GABAergic interneurons after their subsequent release into the extracellular space. The glutamatergic neurons also depend on the astrocytes for the replenishment of Glu via the astrocyte synthesized Gln. This dependence is much stronger than their GABAergic counterparts (Schousboe et al. 2004). Astrocytes are unique in the way that they possess the necessary enzymes for *de novo* synthesis of Glu in the mitochondrial TCA cycle. This is important since both Glu and GABA can be metabolized in the mitochondria of neurons and astrocytes (Yu et al. 1982). The *de novo* synthesis of Glu by astrocytes accounts for 30% of the loss of Glu in the glutamatergic neurons (Oz et al. 2004) and 50% of the loss of GABA in the

GABAergic neurons (Waagepetersen et al. 2001). The proper functioning of this exchange relationship between Gln, Glu, and GABA will ensure the homeostasis of these neurotransmitters in both the intra and extracellular space and the accurate signal communication between neurons. Figure 1-4 (Rowley et al. 2012) illustrates the synthesis, release, reuptake, and metabolism of GABA and Glu in the GABAergic and glutamatergic neurons with the close collaboration of a nearby astrocyte.

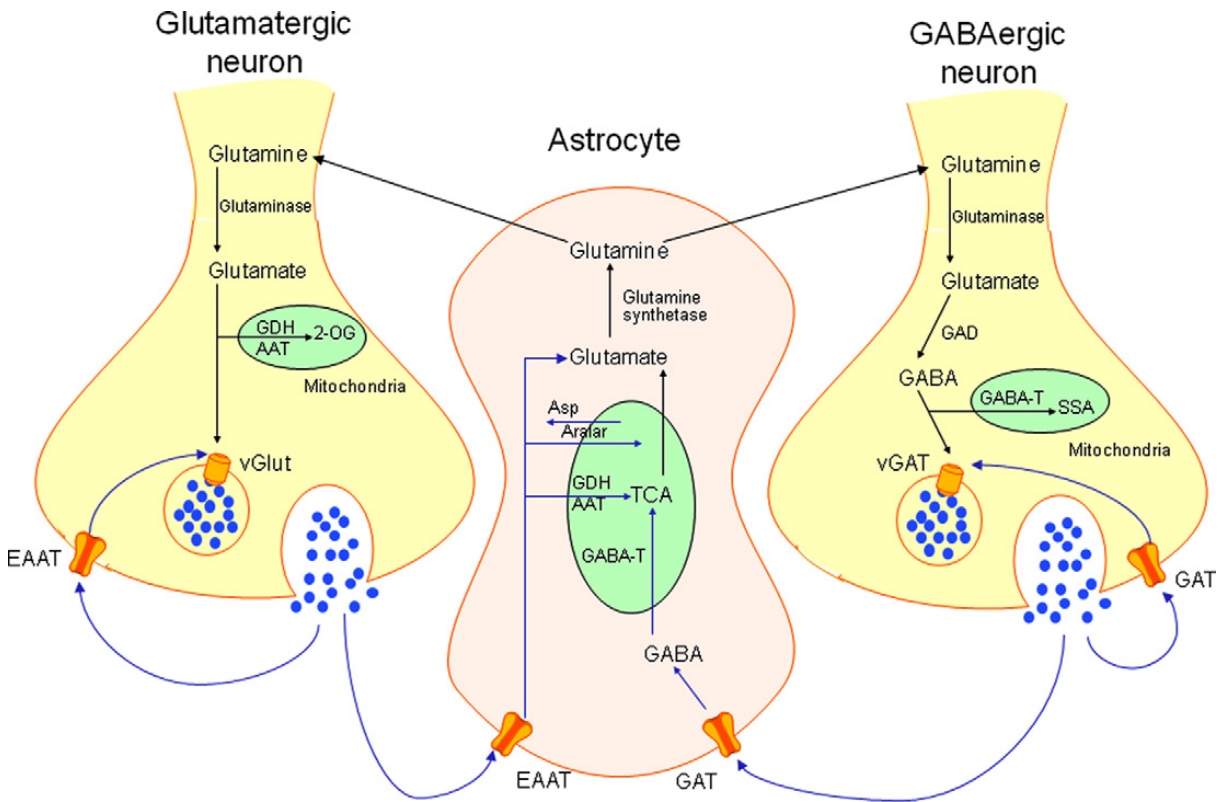


Figure 1-4: The Glutamate-Glutamine-GABA cycle.

(From “Glutamate and GABA synthesis, release, transport and metabolism as targets for seizure control,” by Rowley, N. M., Madsen, K. K., Schousboe, A., and Steve White, H., 2012, *Neurochemistry International*, 61, 546-58. Copyright 2012 by Elsevier. Reprinted with permission.)

## Implications in Psychiatric Disorders

Given the important roles of Glu, Gln, and GABA as the principal excitatory and inhibitory synapses, it is prudent to elucidate their status in various neurologic and psychiatric

disorders and also investigate how they will promote the development of potential pharmacological interventions in the future. Normal brain functions require a balanced execution of both the excitatory and the inhibitory neurotransmission, which further relies on a machinery of enzymes, transporters, and proteins down at the subcellular level. This section of the chapter serves as a basic introduction to two of the research projects I worked on in the field of psychiatry. These projects all share a common goal in that they promote a better understanding of the roles in which Glu, Gln, and, GABA plays in diseased human brains.

### **Major Depressive Disorder**

Major Depressive Disorder (MDD), also known as clinical depression, is characterized by prolonged periods of feeling of sadness, loss of interest, anger and frustration. Clinical depression is a serious mental illness that can interfere with a person's normal daily function as well as social behavior. According to the National Institute of Mental Health, approximately 6.7% of the adult population in the United States suffers from MDD and there is a chance of 20%-25% for an individual to experience MDD in his or her adult life. MDD can co-exist with many other mental disorders, including post-traumatic stress disorder (PTSD), attention-deficit and hyperactivity disorder (ADHD), obsessive-compulsive disorder (OCD), and other mood and anxiety disorders (Reigier et al. 1998; Devane et al. 2005). Other serious medical illnesses can also co-exist with MDD, such as heart disease, stroke, cancer, HIV/AIDS, and so on. Patients with MDD in combination with other serious medical conditions are less likely to respond to medical treatment and more likely to induce more treatment costs (Casano et al. 2002). Proper management of MDD offers potential improvement of treatment outcome for those co-existing medical conditions (Katon et al. 2002).



The exact cause of MDD is still unclear. It is commonly believed that MDD is triggered by a combination of factors related to environment, biology, physiology, psychology, and even genetics. Current common antidepressants used to treat MDD include monoamine oxidase inhibitors (MAOIs), selective serotonin reuptake inhibitors (SSRIs), serotonin norepinephrine reuptake inhibitors (SNRIs), and bupropion (acts as a norepinephrine dopamine reuptake inhibitor). These antidepressants effectively increase synaptic cleft concentrations of the monoamine neurotransmitters, which include serotonin, dopamine, and norepinephrine. The long term increased intrasynaptic concentrations of monoamines will further regulate the functions of monoamine receptors, transporters, and second messengers. Thus, prolonged administration of these antidepressants is required for their effectiveness. The treatment success rate of these medications has been estimated at 65% to 70% (Paul and Skolnick, 2003). Alternatively, a growing interest in the glutamatergic system as potential MDD treatment target has been reported in recent years (Paul and Skolnick, 2003; Maeng and Zarate 2007; Hashimoto 2009; Mathews et al. 2012). In particular, recent reports indicating that ketamine treatment produces a rapid and enduring reduction of MDD symptoms suggest that the glutamatergic neurotransmission system plays an important role in MDD and that more effective treatments might be developed from glutamatergic agents.

### **Autism Spectrum Disorder**

Autism Spectrum Disorder (ASD) is a neurodevelopmental disorder, which is composed of autistic disorder (autism), Asperger's disorder (ASP), and pervasive developmental disorder not otherwise specified (PDD- NOS). These disorders are characterized by problems in social interaction, verbal and nonverbal communication and repetitive behaviors (American Psychiatric Association, DSM-IV TR, 2000). ASD affects approximately 1 in 100 children in the developed

nations (Brugha et al. 2011). U.S. Centers for Disease Control and Prevention (CDC) estimates ASD affects about 1 in 88 American children, with boys four times more likely to be diagnosed with ASD. Clinical signs commonly emerge between 2 to 3 years of age.

The exact cause of ASD is still poorly understood. Cumulative evidence suggests that autistic phenotype is the result of a variety of factors, including genomic abnormalities, environmental risk factors and epigenetic factors. Several lines of evidence indicate that a functional imbalance of glutamatergic and GABAergic neurotransmission may play important roles in the development of ASD (Cook et al, 1998; Fatemi et al, 2008; Polleux et al, 2004; McDougle et al, 2005, Pardo & Eberhart 2007, Rubinstein & Merzenich 2003). During the fetal developmental stage, GABA functions temperately as the major excitatory transmitter. It is believed that GABAergic signal transmission during development regulates the branching and shaping of the neuronal circuits. Understanding the effects of this multifaceted neurotransmission imbalance early in developing infant brains may lead to efficient treatment of this disorder as well as the potential to also lower the lifetime costs associated with caring for individuals with ASD.

## **Conclusion**

Glu, Gln, and GABA play important excitatory and inhibitory messenger role in neuronal signal transmissions. Perturbations in the delicate homeostatic balances between these three neurometabolites have significant implications in various psychiatric disorders. Currently, the glutamatergic and GABAergic neurotransmission systems have been underexploited as alternative treatment targets in various psychiatric disorders. It is important to be able to measure these neurotransmitter concentrations directly in living human brains, since the *in vivo*

concentrations of these neurotransmitters can potentially serve as biomarkers for treatment efficacy evaluations.

## References

- Anderson, C. M., & Swanson, R. A. (2000). Astrocyte glutamate transport: review of properties, regulation, and physiological functions. *Glia*, *32*, 1-14.
- Bak, L. K., Schousboe, A., & Waagepetersen, H. S. (2006). The glutamate/GABA-glutamine cycle: aspects of transport, neurotransmitter homeostasis and ammonia transfer. *J Neurochem*, *98*, 641-53.
- Brugha, T. S., McManus, S., Bankart, J., Scott, F., Purdon, S., Smith, J., Bebbington, P., Jenkins, R., & Meltzer, H. (2011). Epidemiology of autism spectrum disorders in adults in the community in England. *Arch Gen Psychiatry*, *68*, 459-65.
- Cassano, P., & Fava, M. (2002). Depression and public health: an overview. *J Psychosom Res*, *53*, 849-57.
- Cook, E. H., Jr., Courchesne, R. Y., Cox, N. J., Lord, C., Gonen, D., Guter, S. J., Lincoln, A., Nix, K., Haas, R., Leventhal, B. L., & Courchesne, E. (1998). Linkage-disequilibrium mapping of autistic disorder, with 15q11-13 markers. *Am J Hum Genet*, *62*, 1077-83.
- Cooper, A. J. (2001). Role of glutamine in cerebral nitrogen metabolism and ammonia neurotoxicity. *Ment Retard Dev Disabil Res Rev*, *7*, 280-6.
- Danbolt, N. C. (2001). Glutamate uptake. *Prog Neurobiol*, *65*, 1-105.
- Devane, C. L., Chiao, E., Franklin, M., & Kruep, E. J. (2005). Anxiety disorders in the 21st century: status, challenges, opportunities, and comorbidity with depression. *Am J Manag Care*, *11*, S344-53.
- Diazgranados, N., Ibrahim, L., Brutsche, N. E., Newberg, A., Kronstein, P., Khalife, S., Kammerer, W. A., Quezado, Z., Luckenbaugh, D. A., Salvatore, G., Machado-Vieira, R., Manji, H. K., & Zarate, C. A., Jr. (2010). A randomized add-on trial of an N-methyl-D-aspartate antagonist in treatment-resistant bipolar depression. *Arch Gen Psychiatry*, *67*, 793-802.
- Fatemi, S. H., Reutiman, T. J., Folsom, T. D., & Thuras, P. D. (2009). GABA(A) receptor downregulation in brains of subjects with autism. *J Autism Dev Disord*, *39*, 223-30.
- Greengard, P. (2001). The neurobiology of slow synaptic transmission. *Science*, *294*, 1024-30.
- Hashimoto, K. (2009). Comments on "An innovative design to establish proof of concept of the antidepressant effects of the NR2B subunit selective N-methyl-D-aspartate antagonist,

- CP-101,606 in patients with treatment-refractory major depressive disorder". *J Clin Psychopharmacol*, 29, 411-2; author reply 12.
- Hertz, L., Dringen, R., Schousboe, A., & Robinson, S. R. (1999). Astrocytes: glutamate producers for neurons. *J Neurosci Res*, 57, 417-28.
- Katon, W., & Ciechanowski, P. (2002). Impact of major depression on chronic medical illness. *J Psychosom Res*, 53, 859-63.
- Li, K., & Xu, E. (2008). The role and the mechanism of gamma-aminobutyric acid during central nervous system development. *Neurosci Bull*, 24, 195-200.
- Maeng, S., & Zarate, C. A., Jr. (2007). The role of glutamate in mood disorders: results from the ketamine in major depression study and the presumed cellular mechanism underlying its antidepressant effects. *Curr Psychiatry Rep*, 9, 467-74.
- Mathews, D. C., Henter, I. D., & Zarate, C. A. (2012). Targeting the glutamatergic system to treat major depressive disorder: rationale and progress to date. *Drugs*, 72, 1313-33.
- McDougle, C. J., Erickson, C. A., Stigler, K. A., & Posey, D. J. (2005). Neurochemistry in the pathophysiology of autism. *J Clin Psychiatry*, 66 Suppl 10, 9-18.
- Meldrum, B. S. (2000). Glutamate as a neurotransmitter in the brain: review of physiology and pathology. *J Nutr*, 130, 1007S-15S.
- Miles, R. (1999). Neurobiology. A homeostatic switch. *Nature*, 397, 215-6.
- Nolte, J. (2009). *The Human Brain: An Introduction to Its Functional Anatomy*. Philadelphia, PA: Mosby.
- Osen, K. K., Storm-Mathisen, J., Ottersen, O. P., & Dihle, B. (1995). Glutamate is concentrated in and released from parallel fiber terminals in the dorsal cochlear nucleus: a quantitative immunocytochemical analysis in guinea pig. *J Comp Neurol*, 357, 482-500.
- Ottersen, O. P. (1989). Postembedding immunogold labelling of fixed glutamate: an electron microscopic analysis of the relationship between gold particle density and antigen concentration. *J Chem Neuroanat*, 2, 57-66.
- Oz, G., Berkich, D. A., Henry, P. G., Xu, Y., LaNoue, K., Hutson, S. M., & Gruetter, R. (2004). Neuroglial metabolism in the awake rat brain: CO<sub>2</sub> fixation increases with brain activity. *J Neurosci*, 24, 11273-9.
- Pardo, C. A., & Eberhart, C. G. (2007). The neurobiology of autism. *Brain Pathol*, 17, 434-47.
- Patel, A. B., de Graaf, R. A., Mason, G. F., Rothman, D. L., Shulman, R. G., & Behar, K. L. (2005). The contribution of GABA to glutamate/glutamine cycling and energy

- metabolism in the rat cortex in vivo. *Proc Natl Acad Sci U S A*, 102, 5588-93
- Paul, I. A., & Skolnick, P. (2003). Glutamate and depression: clinical and preclinical studies. *Ann N Y Acad Sci*, 1003, 250-72.
- Platt, S. R. (2007). The role of glutamate in central nervous system health and disease--a review. *Vet J*, 173, 278-86.
- Polleux, F., & Lauder, J. M. (2004). Toward a developmental neurobiology of autism. *Ment Retard Dev Disabil Res Rev*, 10, 303-17.
- Regier, D. A., Rae, D. S., Narrow, W. E., Kaelber, C. T., & Schatzberg, A. F. (1998). Prevalence of anxiety disorders and their comorbidity with mood and addictive disorders. *Br J Psychiatry Suppl*, 24-8.
- Rivera, C., Voipio, J., Payne, J. A., Ruusuvuori, E., Lahtinen, H., Lamsa, K., Pirvola, U., Saarma, M., & Kaila, K. (1999). The K<sup>+</sup>/Cl<sup>-</sup> co-transporter KCC2 renders GABA hyperpolarizing during neuronal maturation. *Nature*, 397, 251-5.
- Rothman, D. L., Sibson, N. R., Hyder, F., Shen, J., Behar, K. L., & Shulman, R. G. (1999). In vivo nuclear magnetic resonance spectroscopy studies of the relationship between the glutamate-glutamine neurotransmitter cycle and functional neuroenergetics. *Philos Trans R Soc Lond B Biol Sci*, 354, 1165-77.
- Rowley, N. M., Madsen, K. K., Schousboe, A., & Steve White, H. (2012). Glutamate and GABA synthesis, release, transport and metabolism as targets for seizure control. *Neurochem Int*, 61, 546-58.
- Rubenstein, J. L., & Merzenich, M. M. (2003). Model of autism: increased ratio of excitation/inhibition in key neural systems. *Genes Brain Behav*, 2, 255-67.
- Schousboe, A., Sarup, A., Larsson, O. M., & White, H. S. (2004). GABA transporters as drug targets for modulation of GABAergic activity. *Biochem Pharmacol*, 68, 1557-63.
- Shank, R. P., Bennett, G. S., Freytag, S. O., & Campbell, G. L. (1985). Pyruvate carboxylase: an astrocyte-specific enzyme implicated in the replenishment of amino acid neurotransmitter pools. *Brain Res*, 329, 364-7.
- Shupliakov, O., Brodin, L., Cullheim, S., Ottersen, O. P., & Storm-Mathisen, J. (1992). Immunogold quantification of glutamate in two types of excitatory synapse with different firing patterns. *J Neurosci*, 12, 3789-803.
- Waagepetersen, H. S., Sonnewald, U., Gegelashvili, G., Larsson, O. M., & Schousboe, A. (2001). Metabolic distinction between vesicular and cytosolic GABA in cultured GABAergic neurons using <sup>13</sup>C magnetic resonance spectroscopy. *J Neurosci Res*, 63, 347-55.

Yu, A. C., Schousboe, A., & Hertz, L. (1982). Metabolic fate of <sup>14</sup>C-labeled glutamate in astrocytes in primary cultures. *J Neurochem*, *39*, 954-60.

Zarate, C. A., Jr., Singh, J. B., Quiroz, J. A., De Jesus, G., Denicoff, K. K., Luckenbaugh, D. A., Manji, H. K., & Charney, D. S. (2006). A double-blind, placebo-controlled study of memantine in the treatment of major depression. *Am J Psychiatry*, *163*, 153-5.

## Chapter 2 $^1\text{H}$ Magnetic Resonance Spectroscopy

### Basic Principles

#### Introduction

The field of spectroscopy generally investigates the interaction between matter and electromagnetic radiation (EMR). All matter is made of nuclei and electrons. Nuclei (protons and neutrons) are further made of quarks, which belong to a family of fermion elementary particles with half-integer spin characteristics. In this context, spin is a form of quantum mechanical angular momentum. Spin one-half nuclei are of particular importance because they possess interesting magnetic properties. Proton magnetic resonance spectroscopy ( $^1\text{H}$ -MRS) is the study of the magnetic properties and energies of spin one-half protons in various chemical compounds. MRS is based on the physical phenomenon of nuclear magnetic resonance (NMR), in which nuclei of matter in a magnetic field absorb and emit EMR in the radiofrequency (RF) range.

In 1938, Isidor Rabi first investigated the NMR phenomenon in molecular beams (Rabi et al. 1938). Eight years later, two independent groups of physicists led by Purcell and Bloch extended Rabi's method to determine the properties of nuclei magnetic moments in liquids and solids (Purcell et al. 1946; Bloch and Hansen 1946). In 1950, Protor and Yu from Stanford, as well as Dickinson from Cambridge, simultaneously discovered that nuclei from the same chemical compound absorb and emit RF energy at different frequencies depending on the chemical environment surrounding the nuclei (Protor and Yu 1950; Dickinson 1950). Ernst and Anderson laid down the foundation of modern NMR in 1966 by introducing the concepts of pulsed NMR and Fourier transform NMR (Ernst and Anderson 1996). In 1973, Lauterbur pioneered the technique of *in vivo* magnetic resonance imaging (MRI) using not only the static

magnetic fields but also the spatially variant gradient magnetic fields to create an image of an object by its water content. His works have become the cornerstones to many modern MRI and MRS acquisition techniques.

This chapter first focuses on the basic physical principles of MRS that are of particular importance to my research thesis. Then, a brief introduction to some of the MRS pulse sequences I encountered and investigated for my studies are presented in the second half of this chapter to serve as background information for the upcoming chapters.

## Chemical Shift

In the presence of an external magnetic field, two spin states exist for a group of protons: spin up and spin down. The difference in energy between these two spin states is proportional to the applied external magnetic field strength  $\mathbf{B}_0$ , as well as a constant called the gyromagnetic ratio  $\gamma$ , which depends on the type of nucleus. Since energy is directly proportional to precessional frequency  $\omega_0$ , we can derive the famous Larmor equation as:  $\omega_0 = \left(\frac{\gamma}{2\pi}\right) \mathbf{B}_0$ . Even though a group of protons all have the same gyromagnetic ratio, they don't necessarily share the same Larmor frequency. Protons in molecules form various chemical bonds with other nuclei through the interactions of electrons. In other words, because of the distribution of electrons in a molecule, proton nuclei can be shielded from the applied external magnetic field by nearby electron clouds surrounding them. The cloud of electrons mitigates the overall magnetic field protons might experience inside of a molecule. This shielding effect causes a shift in the precessional frequency away from the Larmor frequency and this phenomenon is called the chemical shift. As a result, resonance signals from different functional groups containing proton nuclei can be distinguished and detected due to the different chemical environments. Figure 2-1 shows a proton NMR spectrum of water and fat molecules. Fatty acid contains a large quantity of



methylene in chain structures and its protons are more shielded than the protons in a simple water molecule. Therefore, water protons process about 3.5 ppm faster than the methylene protons in fat and they are located more up field on the ppm axis than the methylene protons in fat.

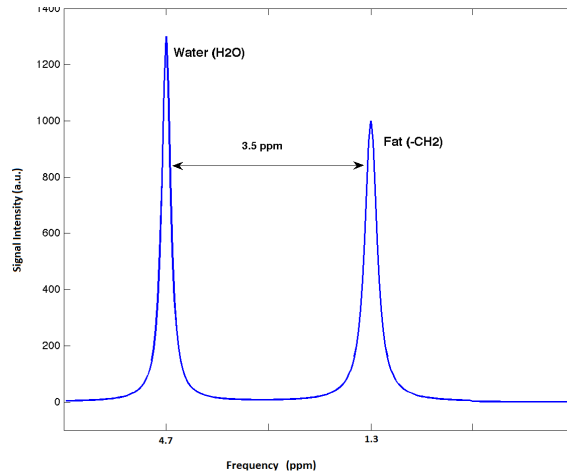


Figure 2-1: Chemical shift of water and fat.

## Fourier Transform

The Fourier transform is a reversible mathematical operation named after its prominent investigator Joseph Fourier. It is the generalization of the complex Fourier series as the limit of approximation approaches infinity. The following equations represent the basic mathematical procedures of the Fourier transform. Equation 2-1 is the forward Fourier transform of  $f(x)$  into function  $F(k)$  and equation 2-2 is the inverse Fourier transform of  $F(k)$ .

$$F(k) = \int_{-\infty}^{\infty} f(x)e^{-2\pi ikx} dx \quad (2-1)$$

$$f(x) = \int_{-\infty}^{\infty} F(k)e^{2\pi ikx} dk \quad (2-2)$$

In pulsed NMR spectroscopy, the resonance signal is measured as a function of time and it is called the time domain signal or the free induction decay (FID). This signal is digitized at

certain intervals by the computer so it is actually not continuous, but for aesthetic and simplicity reasons, they are generally plotted as continuous functions, as shown in Figure 2-2. Any time domain signal function can be represented by the summation of cosine or sine wave functions of different frequencies and amplitudes. After applying the Fourier transform to this complex time domain function, a spectrum, or a function of frequencies is generated. This spectrum reveals the characteristic frequency and amplitude information associated with a proton resonance more naturally than its time domain counterpart. Mathematically, we can write the Fourier transform operation of a complex time domain function  $S(t)$  compactly as:

$$S(t) = S_0 e^{-i\Omega t} e^{-Rt} \xrightarrow{FT} S(\omega) = \frac{S_0 R}{R^2 + (\omega - \Omega)^2} + i \frac{-S_0 (\omega - \Omega)}{R^2 + (\omega - \Omega)^2}, \quad (2-3)$$

where  $S(\omega)$  is a function of frequencies with unit of  $\text{rad s}^{-1}$ .  $\Omega$  is the offset frequency with unit of  $\text{rad s}^{-1}$  and it is generally offset in reference to the resonance frequency of water protons.  $R$  is the first-order decay rate constant with unit of Hz and it equals to the inverse value of the transverse magnetization decay constant  $T_2$ .  $S_0$  is a constant proportional to the equilibrium magnetization.

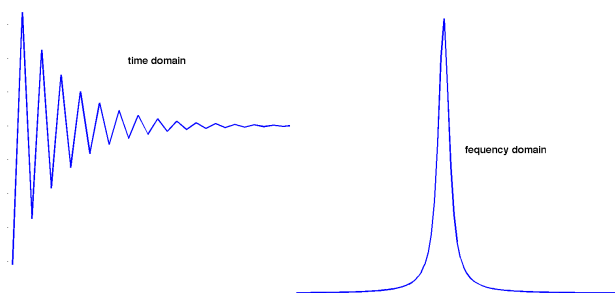


Figure 2-2: Time and frequency domain NMR signal.

## Lineshape

As shown in equation 2-3, Fourier transform of an exponentially decaying time domain function gives a complex frequency domain function in pulsed NMR spectroscopy. The real part of the frequency domain function is called the absorption mode spectrum with a Lorentzian lineshape; the imaginary part of the function is called the dispersion mode spectrum also with

Lorentzian lineshape. As shown in Figure 2-3, the absorption mode spectrum is always positive, but the dispersion mode spectrum has both positive and negative parts. There are two key parameters associated with both modes of spectrum. The first one is the value at which the height of the signal equals to half of its maximum and we call this parameter the full width at half maximum (FWHM); the second parameter is the height of the spectrum peak. Both featured parameters are shown in Figure 2-3 and it is shown that both FWHM and the peak height is related to the decay rate constant R.

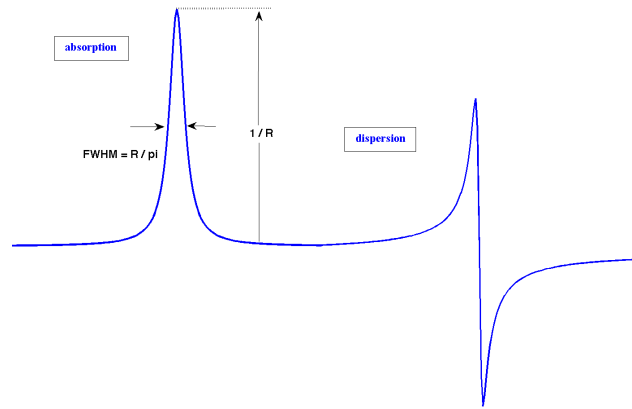


Figure 2-3: Absorption and dispersion mode NMR spectrum.

## Phase

The time domain signal detected by a spectrometer does not always correspond to the magnetization induced by the RF system. Generally, there is an unavoidable phase term associated with the signal function and this phase term results from the design of the signal detection hardware system used by most MRI scanners and is essentially arbitrary. Mathematically, to take into account the effect of this arbitrary phase term  $\phi$ , we can rewrite equation 2-3 into the following form:

$$S(t) = S_0 e^{-i\Omega t} e^{-Rt} e^{i\phi} \xrightarrow{FT} S(\omega) = \left( \frac{S_0 R}{R^2 + (\omega - \Omega)^2} + i \frac{-S_0 (\omega - \Omega)}{R^2 + (\omega - \Omega)^2} \right) e^{i\phi}. \quad (2-4)$$

This equation basically tells us that the real and imaginary part of the frequency domain signal function is a mixed state of both absorption and dispersion mode spectrum. And the phase  $\phi$  decides the relative contribution of the absorption and dispersion mode in the frequency domain signal. Examples of how phase ( $\phi=0$ ,  $\phi=\pi/4$ ,  $\phi=\pi/2$ ,  $\phi=\pi$ ) influences the frequency domain lineshape are shown in Figure 2-4. In the case of  $\phi=\pi$ , a phase shift of  $180^\circ$  is presented and the spectrum is simply inverted on both absorption and dispersion mode.

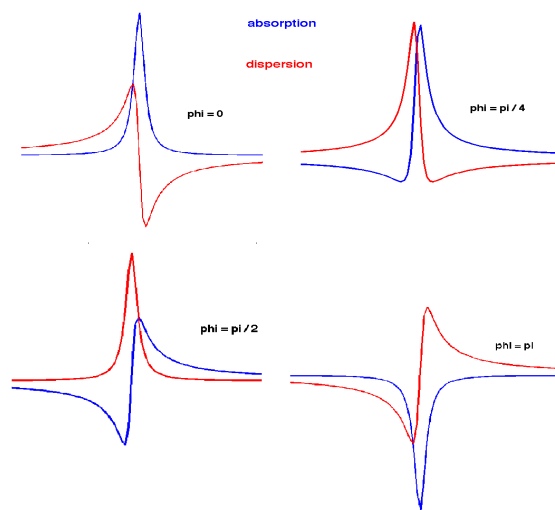


Figure 2-4: Absorption and dispersion mode spectra with phase shifts.

## J coupling

Nuclear spins in chemical compounds can interact with each other not only through the direct dipole-dipole coupling, but they also can interact with each other through electrons in the chemical bonds. This interaction mediated by chemical bonds is called the scalar coupling, or J coupling. Such interactions give rise to the multiplet signal patterns commonly seen in a NMR spectrum. An example of the proton MRS spectrum of ethanol is shown in Figure 2-5. In general, if a spin is coupled with a nearby N equivalent nucleus, its peak is split into N+1 multiplets. The intensity ratios of the multiplet peaks follow the Pascal's triangle rule. If this same spin is coupled with additional spins, its multiplet peaks will further split into additional complex

components. The signal peak from protons in the  $\text{-CH}_3$  group of ethanol splits into a triplet because of the two protons in the adjacent  $\text{-CH}_2$  group; the signal peak from protons in the  $\text{-CH}_2$  group splits into a quartet because of the three equivalent protons in the  $\text{-CH}_3$  group. The proton from the  $\text{-OH}$  group does not couple with any of the nearby protons because of rapid exchange with solvent water protons. However, all we have described about the multiplets is limited to the scope of weak coupling spin systems, where the separation in frequency of two coupled spins is much larger than the value of the  $J$  coupling constant between these two spins. Conversely, if the separation in frequency is comparable to the value of the  $J$  coupling constant, then the assumptions of peak splitting and intensity ratios are not governed by what we have just described. This condition is referred to as the strongly coupled spin system. Under such circumstances, the frequencies and intensity values of the multiplets cannot be predicted without resorting to quantum mechanical calculations (Keeler 2010). In either case,  $J$  coupling phenomenon provides useful information and it is used to determine the structure of a molecule by revealing the connectivity of the atoms within itself.

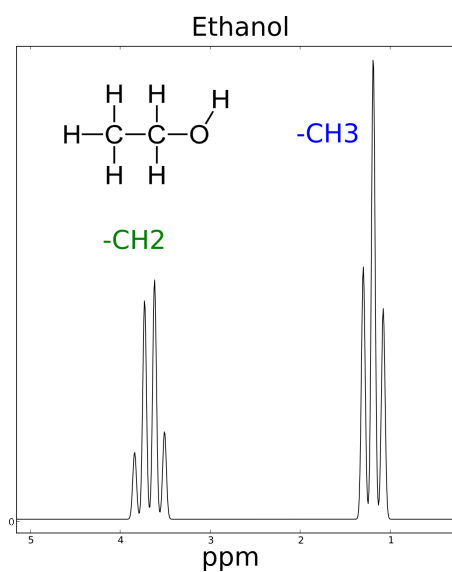


Figure 2-5: Proton NMR spectrum of ethanol.

## MRS Signal Acquisition

### MR Pulse Sequence

A pulsed experiment in MRS is performed by the execution of a MR pulse sequence by a MRI scanner. A  $^1\text{H}$ -MRS or MRI pulse sequence is a combination of RF pulses and gradient pulses arranged in a specific order to excite, encode, and detect resonance signals. Computers then record these resonance signals, which will be further processed into images or spectra that reflect properties of the object of interest. Since NMR signals are actually rather weak, it is often necessary to increase the signal-to-noise ratio (SNR) by repeating a MR pulse sequence multiple times. In  $^1\text{H}$ -MRS, there are two major categories of acquisition schemes: the single voxel method and the multi-voxel method. The multi-voxel method is also known as the magnetic resonance spectroscopic imaging (MRSI) technique. Voxel localization is very important in MRS and it is generally achieved with the help of volumetric T1-weighted or T2-weighted MRI images. In 1986, Ordidge et al introduced the image selected *in vivo* spectroscopy (ISIS) localization scheme, in which three frequency selective  $180^\circ$  RF pulses are turned on and off to achieve 3D localization in eight scans (Ordidge et al. 1986). This method is limited by many factors, including  $B_0$  and  $B_1$  field inhomogeneity, 'T1 smearing' (Lawry et al. 1989), incomplete water suppression, and motion artifacts due to the long acquisition time for *in vivo* applications. One year later, Frahm et al introduced the stimulated echo acquisition mode (STEAM) method to achieve 3D localization in a single scan using three frequency selective  $90^\circ$  RF pulses. STEAM method is actually a lot more complicated than ISIS or other acquisition methods because of the utilization of multiple  $90^\circ$  pulses. Multiple  $90^\circ$  pulses can induce multiple quantum coherence transfer effect in J coupled spins (de Graaf 2007). Although the STEAM method is very useful in

detecting resonance signals from many metabolites, this section will focus mainly on three other MRS or MRSI pulse sequences I have studied for my dissertation.

## PRESS

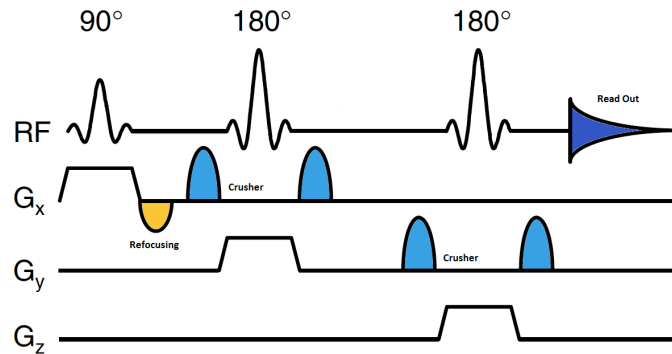


Figure 2-6: Pulse sequence diagram for single voxel PRESS acquisition.

Figure 2-6 shows the pulse sequence diagram of a point resolved spectroscopy (PRESS) acquisition method, known otherwise as the double spin echo method (Bottomley, 1987), because two slice selective  $180^\circ$  refocusing pulses are used in this technique. Similar to the STEAM method, the PRESS method is also capable of single voxel localization in a single scan, but offer superior SNR than the STEAM method. Time variant gradients along three orthogonal axis X, Y, and Z are used with three RF pulses to achieve 3D localization. The first RF pulse is a  $90^\circ$  slice selective excitation pulse, and the second and third pulses are also slice selective but they function as refocusing pulses. A negative refocusing gradient is necessary right after the  $90^\circ$  excitation pulse to refocus the phase evolution. Due to the imperfections of the  $180^\circ$  pulse profile, a pair of crusher gradient pulses surrounding the  $180^\circ$  pulse is usually used to eliminate undesired spin coherences. The first  $90^\circ$  and  $180^\circ$  pulses produce the first spin echo signal, which comes from the intersection of two orthogonal planes selected by these two RF pulses and gradient pulses. The second spin echo signal comes from an area where all three orthogonal planes intersect. Therefore, the second spin echo signal is what the analog-to-digital convertor (ADC)

will detect and it is also what the scanner computer will record as the time domain signal. Paul A. Bottomley first introduced this technique in 1987 and his PRESS acquisition technique has since been widely accepted as a popular  $^1\text{H}$ -MRS method for both researchers and clinicians.

## CSI

In the presence of phase encoding gradient pulses, a single voxel acquisition technique can be modified into a multi-voxel acquisition technique. This phase encoding procedure is very similar to that used in MRI. As shown in Figure 2-7, a pulse sequence diagram of a 2D chemical shift imaging (CSI) sequence, the multi-voxel capability is achieved by extending the single voxel PRESS sequence with additional phase encoding gradients in the X and Y directions. The set of phase encoding gradient pulses shown in Figure 2-7 is composed of multiple time variant magnetic field gradient pulses, whose amplitude increases with subsequent scans to encode for spatial information in either the X or the Y direction. Instead of only performing Fourier transform in the time domain axis, this operation will need to be extended to the other two phase encoding directions. We can write down the complete Fourier transformation process in the time direction, X and Y spatial direction as the following mathematical representation

$$f(x, y, \omega) = \iiint_{-\infty}^{\infty} F(k_x, k_y, t) e^{-i(k_x x + k_y y)} dk_x dk_y dt, \quad (2-5)$$

where  $k_x = \gamma G_x t$ ,  $k_y = \gamma G_y t$ ,  $G_x$  and  $G_y$  are the gradient amplitudes in the X and Y direction. This equation provides spectral information  $f(x, y, \omega)$  from spatial position X and Y, and time. It is important to point out that the actual MRSI data is collected in a finite and discrete manner in both the time domain and spatial or k-space domain. As a consequence, the discrete version of the Fourier transform algorithm is often applied to the MRS and MRSI data. In 1982, Brown et al at the Bell Laboratories were the first to introduce the CSI acquisition approach and collected



a phosphorylated metabolite image of human brain with 2 cm spatial resolution (Brown et al 1982; Maudsley et al. 1983 ).

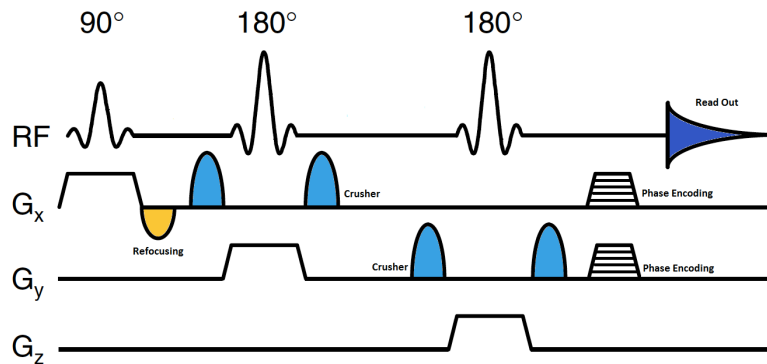


Figure 2-7: Pulse sequence diagram of 2D CSI.

## PEPSI

The major advantage of a multi-voxel MRSI method over a single voxel method is its ability to provide spatial distributions of metabolite information from an area of interests. However, the total scanning time for a CSI acquisition is very long when compared with a PRESS single voxel scan due to the time-consuming phase encoding procedures. To shorten the overall scanning time of a multi-voxel acquisition, more efficient k-space sampling schemes must be utilized. One such method is called the proton echo planar spectroscopic imaging (PEPSI). The echo planar based method was first proposed by Mansfield almost thirty years ago and further implemented by others (Mansfield 1984; Matsui et al 1985; Webb et al 1989; Posse et al 1994; Ebel et al 2001). Instead of sampling the time domain data voxel by voxel, the PEPSI method samples an entire column of time domain data in a single scan to achieve time reduction. This simultaneous spatial and spectral encoding is carried out by a series of bipolar trapezoidal gradients (as shown in Figure 2-8) and this encoding scheme forms a zigzag trajectory in the k-space. Unlike the CSI method, volume localization in PEPSI is attained by one  $90^\circ$  pulse and one  $180^\circ$  pulse only. Additionally, extra outer volume suppression (OVS) pulses are employed to

reduce contamination from lipid signals. The spatial resolution and spectral bandwidth of a PEPSI acquisition is limited by the scanner gradient performance and eddy current induced artifacts are more prominent in this type of acquisition. However, PEPSI sequence provides considerable amount of acceleration in acquisition time and the SNR per unit time is comparable to the conventionally acquired multi-voxel data with similar acquisition settings. Therefore, PEPSI method is suitable for fast whole brain MRSI acquisition in both healthy controls as well as in patients and children who are less likely to tolerate long scans.

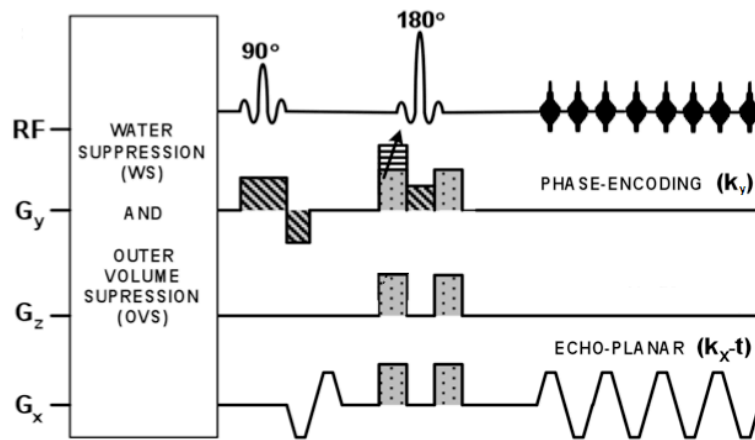


Figure 2-8: Pulse sequence diagram of 2D PEPSI acquisition.

## References

- Bloch, F. (1946). Nuclear Induction. *Physical Review*, 70, 460-74.
- Bottomley, P. A. (1987). Spatial localization in NMR spectroscopy in vivo. *Ann N Y Acad Sci*, 508, 333-48.
- Brown, T. R., Kincaid, B. M., & Ugurbil, K. (1982). NMR chemical shift imaging in three dimensions. *Proc Natl Acad Sci U S A*, 79, 3523-6.
- Dickinson, W. C. (1950). Dependence of the F19 Nuclear Resonance Position on Chemical Compound. *Physical Review*, 77, 736-37.
- Ebel, A., Soher, B. J., & Maudsley, A. A. (2001). Assessment of 3D proton MR echo-planar spectroscopic imaging using automated spectral analysis. *Magn Reson Med*, 46, 1072-8.

- Ernst, R. R., & Anderson, W. A. (1966). Application of Fourier Transform Spectroscopy to Magnetic Resonance. *Review of Scientific Instruments*, 37, 93-102.
- Frahm, J., Merboldt, K.-D., & Hänicke, W. (1987). Localized proton spectroscopy using stimulated echoes. *Journal of Magnetic Resonance*, 72, 502-08.
- Graaf, R. A. d. (2007). *In vivo NMR Spectroscopy: Principles and Techniques*: John Wiley & Sons, Ltd.
- Keeler, J. (2010). *Understanding NMR Spectroscopy*: John Wiley and Son, Ltd.
- Lawry, T. J., Karczmar, G. S., Weiner, M. W., & Matson, G. B. (1989). Computer simulation of MRS localization techniques: an analysis of ISIS. *Magn Reson Med*, 9, 299-314.
- Mansfield, P. (1984). Real-time echo-planar imaging by NMR. *Br Med Bull*, 40, 187-90.
- Matsui, S., Sekihara, K., & Kohno, H. (1985). High-speed spatially resolved high-resolution NMR spectroscopy. *Journal of the American Chemical Society*, 107, 2817-18.
- Maudsley, A. A., Hilal, S. K., Perman, W. H., & Simon, H. E. (1983). Spatially resolved high resolution spectroscopy by "four-dimensional" NMR. *Journal of Magnetic Resonance*, 51, 147-52.
- Ordidge, R. J., Connelly, A., & Lohman, J. A. B. (1986). Image-selected in Vivo spectroscopy (ISIS). A new technique for spatially selective nmr spectroscopy. *Journal of Magnetic Resonance*, 66, 283-94.
- Posse, S., Tedeschi, G., Risinger, R., Ogg, R., & Le Bihan, D. (1995). High speed 1H spectroscopic imaging in human brain by echo planar spatial-spectral encoding. *Magn Reson Med*, 33, 34-40.
- Proctor, W. G., & Yu, F. C. (1950). The Dependence of a Nuclear Magnetic Resonance Frequency upon Chemical Compound. *Physical Review*, 77, 717-17.
- Purcell, E. M., Torrey, H. C., & Pound, R. V. (1946). Resonance Absorption by Nuclear Magnetic Moments in a Solid. *Physical Review*, 69, 37-38.
- Rabi, I. I., Zacharias, J. R., Millman, S., & Kusch, P. (1938). A New Method of Measuring Nuclear Magnetic Moment. *Physical Review*, 53, 318-18.
- Webb, P., Spielman, D., & Macovski, A. (1989). A fast spectroscopic imaging method using a blipped phase encode gradient. *Magn Reson Med*, 12, 306-15.

## Chapter 3 $^1\text{H}$ -MRS of the Human Brain

### Introduction

Proton magnetic resonance spectroscopy ( $^1\text{H}$ -MRS) is a non-invasive analytical technique that allows the detection and quantification of *in vivo* chemical compound concentrations under the image guidance with MRI. The most prominent application of  $^1\text{H}$ -MRS is in the human brain due to its ability to directly measure neurotransmitter and neurometabolite concentrations at a localized anatomical region. Neurometabolites are the intermediates and products of neuronal cell metabolic activities. The change in neurotransmitter and neurometabolite concentrations due to pathological processes can vary and can even be well below the detection limits of modern whole-body MRI scanners. Hence, it is essential to be able to obtain and quantify  $^1\text{H}$ -MRS signals *in vivo* accurately with the most optimal acquisition techniques and the most suitable analytical software for post processing and concentration estimation.

In general, there are about 15 to 20 neurotransmitters and neurometabolites that can be detected from a short echo time (TE)  $^1\text{H}$ -MRS spectrum *in vivo* (Pfeuffer et al 1999). The detection sensitivity and accuracy increases with rising scanner field strength and improved scanner shim performance. Table 3-1 lists the major neurotransmitters, neurometabolites, and their measured concentration values commonly observed by  $^1\text{H}$ -MRS methods *in vivo*. Neurotransmitters and neurometabolites in human brain often have distinctive and identifiable resonance peaks in a MRS spectrum, as shown in Figure 3-1. They are easily recognizable even by the human eye, but a mathematical based fitting algorithm must be used to process the spectrum, so that strongly overlapping and J coupled spins can be distinguished from the larger and narrower peaks.

<b>Compound</b>	<b>Proton Position</b>	<b>Chemical Shift ( ppm )</b>	<b><i>In vivo</i> Concentration ( mMol )</b>
N-Acetyl Aspartate (NAA)	<sup>2</sup> CH <sub>3</sub>	2.009	7.5-17
N-Acetylaspartyl glutamate (NAAG)	<sup>2</sup> CH <sub>3</sub>	2.046	0.5-2.5
γ-Aminobutyric acid (GABA)	<sup>4</sup> CH <sub>2</sub>	3.01	1-2
	<sup>3</sup> CH <sub>2</sub>	1.89	
	<sup>2</sup> CH <sub>2</sub>	2.28	
Alanine (Ala)	<sup>3</sup> CH <sub>3</sub>	1.47	0.1-1.5
Aspartate (Asp)	<sup>2</sup> CH	3.89	1-2
	<sup>3</sup> CH <sub>2</sub>	2.80/2.65	
Choline (Cho)	(CH <sub>3</sub> ) <sub>3</sub>	3.19	0.5-2.5
	<sup>1</sup> CH <sub>2</sub>	4.05	
	<sup>2</sup> CH <sub>2</sub>	3.50	
Creatine (Cr)	CH <sub>3</sub>	3.0	4.5-10.5
	CH <sub>2</sub>	3.91	
Phosphocreatine (PCr)	CH <sub>3</sub>	3.03	3-5.5
Phosphorylcholine (PC)	(CH <sub>3</sub> ) <sub>3</sub>	3.21	0.2-1
Glutamate (Glu)	<sup>2</sup> CH	3.75	6-12.5
	<sup>3</sup> CH <sub>2</sub>	2.04/2.12	
	<sup>4</sup> CH <sub>2</sub>	2.34/2.35	
Glutamine (Gln)	<sup>2</sup> CH	3.76	3-6
	<sup>3</sup> CH <sub>2</sub>	2.14/2.12	
	<sup>4</sup> CH <sub>2</sub>	2.43/2.46	
Glycerophosphorylcholine (GPC)	<sup>1</sup> CH <sub>2</sub>	3.61/3.67	0.5-1.5
	<sup>2</sup> CH	3.90	
	<sup>3</sup> CH <sub>2</sub>	3.87/3.95	
Myo-Inositol (mI)	<sup>1,3</sup> CH	3.52	4-9
	<sup>2</sup> CH	4.05	
	<sup>4,6</sup> CH	3.61	
	<sup>5</sup> CH	3.27	
Lactate (Lac)	<sup>2</sup> CH	4.1	0.2-1
	<sup>3</sup> CH <sub>3</sub>	1.31	
Taurine (Tau)	<sup>1</sup> CH <sub>2</sub>	3.42	2-6
	<sup>2</sup> CH <sub>2</sub>	3.25	
Scyllo-Inositol (sI)	<sup>1-6</sup> CH	3.34	0.2-0.5

Table 3-1: <sup>1</sup>H Chemical shifts of neurometabolites and their *in vivo* concentrations.

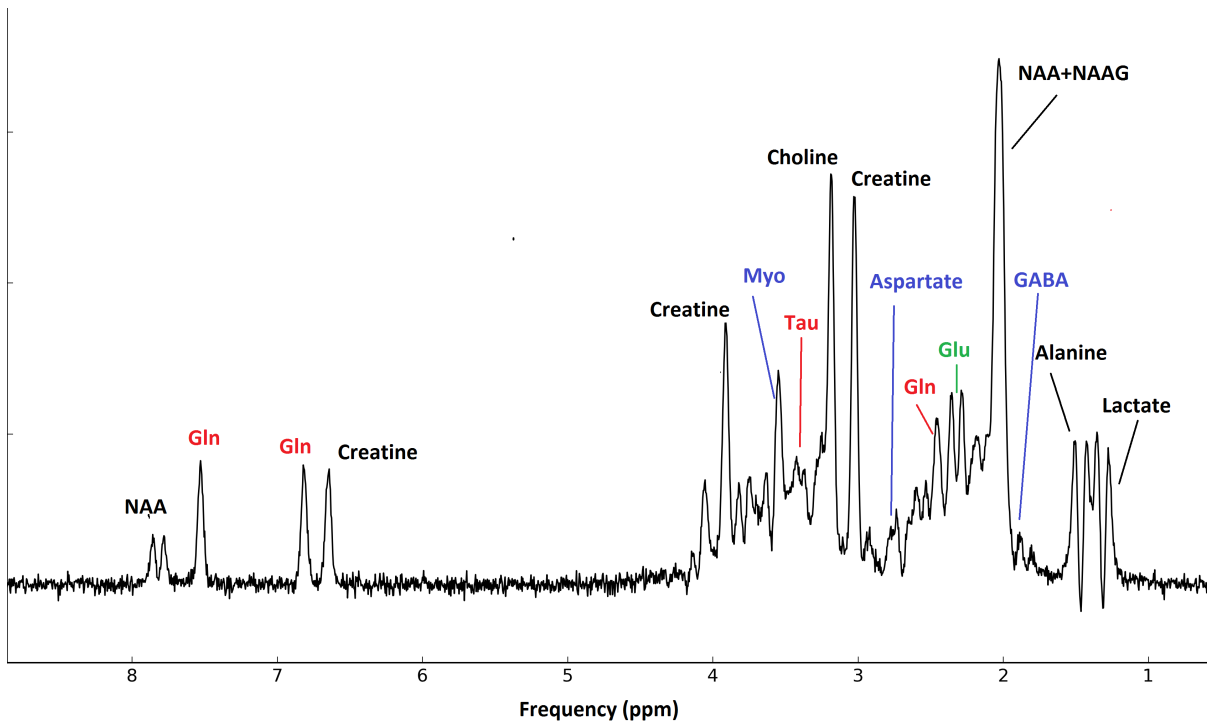
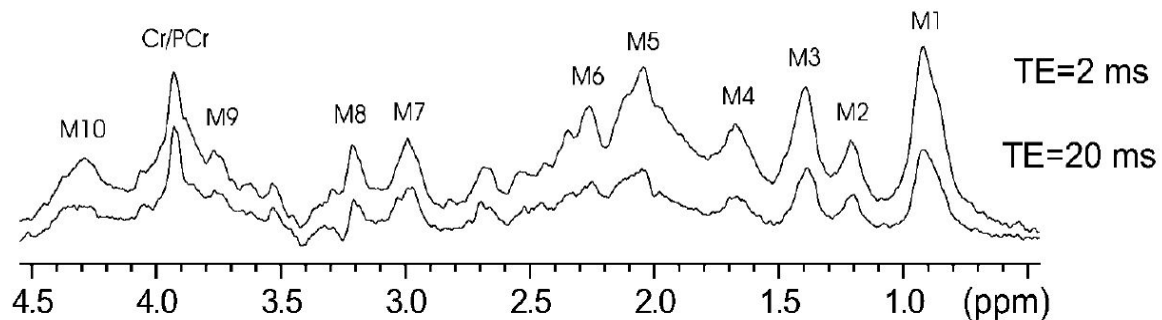


Figure 3-1: Simulated brain proton NMR spectrum with PRESS TE 30 ms acquisition at 3 T.

Another important factor influences in vivo  $^1\text{H}$ -MRS resonance peak recognition and quantification is the presence of short  $T_1$  and  $T_2$  macromolecule signals in a brain spectrum (Behar et al 1994;). The macromolecule  $T_2$  values are several times smaller than the metabolite  $T_2$  values, approximately 26 ms at 9.4 T (Pfeuffer et al 1999). Figure 3-2 also shows the macromolecule signals that are detected in rat brain at 9.4 T, using an inversion recovery method (Pfeuffer et al 1999). Major peaks are visible at 0.93 ppm (M1), 1.24 ppm (M2), 1.42 ppm (M3), 1.72 ppm (M4), 2.05 ppm (M5), 2.29 ppm (M6), 3.00 ppm (M7), 3.2 ppm (M8), 3.77 ppm (M9), and 4.29 ppm (M10). Because of the relative short  $T_2$  values, macromolecules have wider linewidths than the other metabolites. The  $T_2$  values of these macromolecules increase with reduced field strength, so they have significant contribution to the overall spectral shape at short TE acquisition. For instance, M5, M6, M7, and M8 signal peaks overlap with resonance signals

from NAA, NAAG, Glu, Gln, Cr, and tCho. If these macromolecule signals are not properly accounted for during spectral quantification, the concentration estimation for NAA, NAAG, Glu, Gln, Cr, and tCho can be either over or under estimated. As a result, a solution to the macromolecule problem is to use long TE (TE>100 ms) acquisitions to diminish their contamination. However, as TE increases, the SNR decreases due to the finite T<sub>2</sub> values of the regular neurometabolites. T<sub>2</sub> values of NAA, Cr, and Cho have been reported at 3 T, ranging from 137 ms to 264 ms (Zaaraoui et al. 2007). Also, low SNR results in poor spectral quantification for low amplitude signal peaks, such as Glu, Gln, GABA and others.



**Figure 3-2: Macromolecule baseline obtained from an inversion recovery acquisition in rat brain at 9.4 T.**

(From: “Toward an *in vivo* neurochemical profile: quantification of 18 metabolites in short-echo-time <sup>1</sup>H NMR spectra of the rat brain,” by Pfeuffer, J., Tkac, I., Provencher, S. W., and Gruetter, R., 1999, *Journal of Magnetic Resonance*, 141, 104-20. Copyright 2012 by Elsevier. Reprinted with permission.)

Chapter 2 is an introduction to the basic information related to neurotransmitters Glu, Gln, and GABA under the scope of <sup>1</sup>H-MRS. This chapter discusses *in vivo* <sup>1</sup>H spectral quantification with LCModel, a commercial software package that is often used for quantification of *in vivo* spectra. At the end of this chapter, we will revisit the topic of glutamatergic and GABAergic neurotransmission in the Major Depressive Disorder and the Autism Spectrum Disorder, with special focus on the reports of *in vivo* Glu, Gln and GABA concentrations measured with <sup>1</sup>H-MRS techniques.

## <sup>1</sup>H-MRS of Glu, Gln, and GABA

### Glutamate

Glu has three groups of <sup>1</sup>H-MRS observable resonance peaks and the C2 methine, C3 and C4 methylene protons produce these signal peaks, as illustrated in Figure 3-3. The C2 methine proton appears at 3.75 ppm as a triplet. The C3 and C4 methylene protons appear as complicated multiplets at the range of 2.04 ppm to 2.35 ppm due to the strong coupling between the two methylene groups and the methine group (Govindaraju et al 1998). As a consequence, the amplitudes of the proton resonance peaks are greatly reduced because of the J coupling effect. Even though Glu has an *in vivo* concentration of 6-12.5 mMol, which is slightly higher than the 4.5-10.5 mMol *in vivo* concentration of Creatine, the multiplets of Glu are spread across the spectrum just to the left shoulder of NAA peak and causing them to appear to be small.

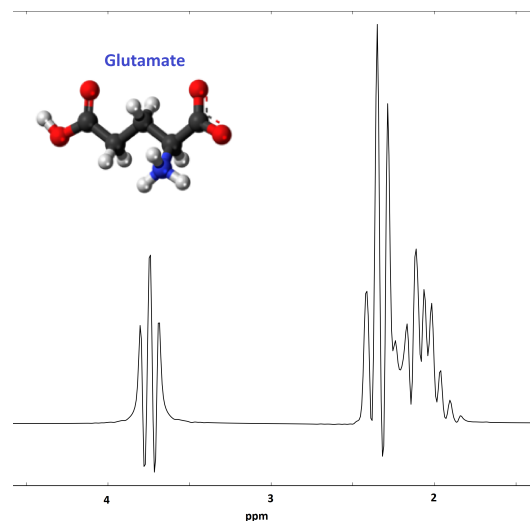


Figure 3-3: Chemical structure and simulated proton NMR spectrum of glutamate.

### Glutamine

The chemical structure of Gln is very similar to the structure of Glu, so the chemical shift values and J coupling interaction of resonance peaks of Gln are also very similar to that of Glu. As shown in Figure 3-3, Gln also has a strongly coupled AMNPQ spin system. The C2 methine



triplet appears at 3.76 ppm and the two groups of methylene multiplets spread across the range of 2.12 ppm to 2.46 ppm (Govindaraju et al 1998). Because of the presence of amide protons, two additional resonance peaks are produced in Gln at 6.82 ppm and 7.73 ppm, but they are not present in Glu. Due to the rapid chemical exchange rate with the water protons, the 6.82 ppm and 7.73 ppm resonance peaks of Gln are difficult to detect with  $^1\text{H}$ -MRS. Gln has an *in vivo* concentration of 2-4 mMol and this value is about one third of the Glu *in vivo* concentration in normal brain.

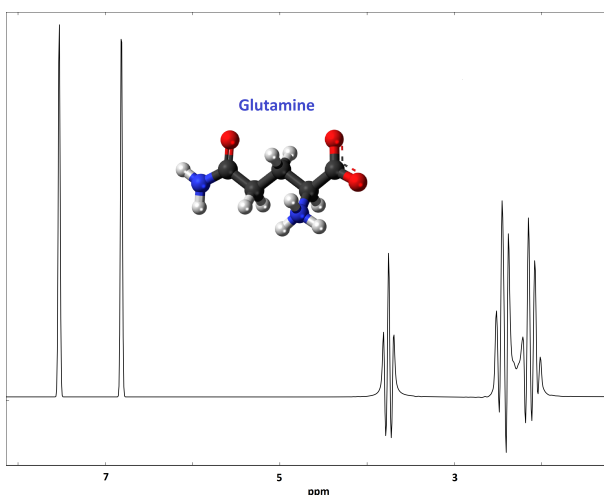


**Figure 3-4: Chemical structure and simulated proton NMR spectrum of glutamine.**

It is virtually impossible to separate Glu and Gln spectra due to their structural similarities, as shown in Figure 3-5. An enormous amount of magnetic field strength (18 T) is required for some of their protons to become weakly coupled and this condition is not applicable for *in vivo* studies. Nonetheless, with increasing magnetic field strength, the C4 methylene multiplets of Glu and Gln can be visually separated. At low field strength (1.5 and 3 T), Glu and Gln resonance signals are not reliably separated without using special pulse sequences, such as the multiple quantum filtering method (Thompson and Allen 1998), the spectral-selective

refocusing method (Choi et al. 2006), and the difference spectroscopy using PRESS asymmetry method (Snyder et al. 2010).

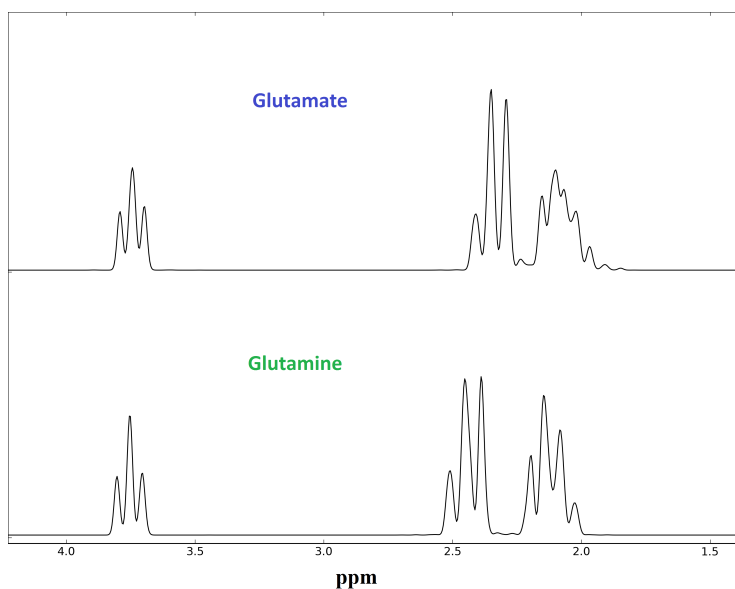


Figure 3-5: Simulated proton spectra of glutamate and glutamine with PRESS TE 30 ms acquisition at 3T.

## GABA

GABA can be considered as a weakly coupled  $A_2M_2P_2$  spin system at 3 T. It has three methylene groups that all produce observable resonance signal in the  $^1H$  spectrum. As shown in Figure 3-6, the C2 and C4 protons produce triplets at 2.28 ppm and 3.01 ppm; the C3 protons produce a quintet at 1.89 ppm. Unfortunately, all three multiplets overlap with other major metabolites. The C2 peaks overlap with Glu and Gln. The C4 peaks overlap with the creatine peak. The C3 peaks are towered over by the right shoulder of the NAA peak. GABA has an in vivo concentration of 1 mMol (de Graaf 2007), which makes it even more difficult to be detected and quantified.

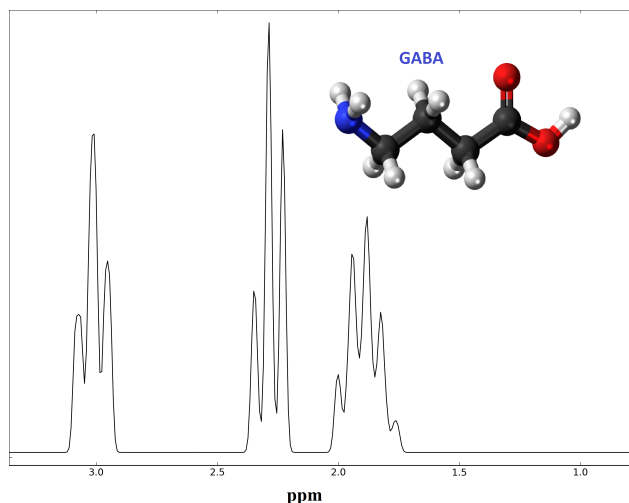


Figure 3-6: Simulated proton NMR spectrum of GABA.

## Spectral Quantification

### Overview

One important aspect of NMR spectroscopy is the post-processing of acquired resonance signals and the quantification of metabolite concentrations. This task remains as one the most challenging topics in the field of *in vivo* MRS despite the numerous publications already exist. Quantification methods can be divided into two primary categories: the time domain methods and the frequency domain methods. Under each of these categories, quantification methods can be further subdivided into the prior-knowledge or model based techniques and the black box or singular value decomposition (SVD) based techniques.

The most well-known time domain model based software package is the jMRUI (Naressi et al 2001). jMRUI is a JAVA based graphical interface that includes the AMARES (Vanhamme et al 1997) program, its predecessor VARPRO (Van der Veen et al 1988), and a quantum mechanical based simulation program called NMR-SCOPE (Graveron-Demilly et al. 1993). In

the time domain prior-knowledge based fitting methods, metabolite quantification is performed in the time domain using model spectra generated either *in vitro* or through computer simulations. The most popular frequency domain method is the LCModel software (Provencher 1993), which quantifies metabolite concentrations using frequency domain spectra and model basis-sets.

Model based time and frequency domain methods are very similar in performance, but the time domain methods offer more flexibility in fitting spectrum of non-Lorentzian lineshape. Frequency domain fitting methods require the fast Fourier transform (FFT) operation to the time domain data, hence, it is advantageous to avoid the FFT operation when the time domain data 1) have non-Gaussian noise, and 2) data sampling does not satisfy the Nyquist sampling condition (Poulet et al 2008). Few studies have compared the time and frequency domain methods and the results are often inconclusive (Kanowski et al 2004; van den Boogaart et al 1995). This section of the chapter will be devoted to the principles and applications of LCModel software package in human brain  $^1\text{H}$  NMR quantification.

## LCModel

The ‘LC’ in LCModel stands for linear combination. The concept of the linear combination modeling algorithm was first proposed by de Graaf and Bovee and was made commercially accessible by Provencher in the early 90s (de Graaf and Bovee 1990; Provencher 1993). The underlying assumption of this technique is that the NMR signal collected *in vivo* can be viewed as a linear combination of the NMR signals that are produced by individual chemical compounds. In practice, by using a complete set of model spectra of neurometabolites, either created *in vitro* or through density matrix simulations, the frequency domain data of an *in vivo*  $^1\text{H}$  NMR spectrum can be analyzed with LCModel with minimum user interaction. Because LCModel can automatically analyze  $^1\text{H}$  spectra, it is convenient to use this software to process a

large quantity of data with minimum human error. Hence, the resulting concentration outputs from LCModel can be compared between healthy and diseased population to reveal underlying biochemical differences in human brain.

Computationally, the NMR signal quantification in the frequency domain is carried out with the Levenberg-Marquart algorithm (LMA), which is also known as the damped least-square (DLS) method. The LMA is essentially a mathematical curve-fitting algorithm that provides solutions to the minimization problem of a non-linear function using another model function. Similarly, LCModel software utilizes the same mathematical principles to solve for concentration values or coefficients that provide the smallest least squares deviation between the frequency domain data and the model basis functions. Provencher discusses the LCModel algorithm in detail in the 1993 publication and its mathematical theory is also discussed in another paper from 1982 (Provencher 1993; Provencher 1982). One of the most important features of LCModel is the incorporation of a cubic B-spline function to represent *in vivo* macromolecule baseline. Since the completeness of the model functions dictates the accuracy in signal quantification, modeling the macromolecule baseline with cubic B-spline function offers a solution to this problem. Pfeuffer et al. further validated the robustness of LCModel in modeling macromolecule baseline using high field rat brain data (Pfeuffer et al. 1999). In addition to model basis functions, also known as hard constraints, LCModel also employs many soft constraints in its LMA implementation. These soft constraints include zero and first order phase correction, linewidth broadening parameter, frequency shift parameter to account for reference error, eddy current lineshape correction, and the cubic B-spline modeling for macromolecule baseline. Together, these soft constraints ensure the solution to the metabolite concentrations is as accurate as possible to the actual values obtained *in vivo*.

LCModel also offers quantification error estimation using the Cramer-Rao lower bounds (CRLB). De Graaf has argued that such error estimation techniques are less than ideal, since for *in vivo* NMR spectra, an exact set of model basis functions that matches each experimental data set does not exist due to the presence of macromolecules. The calculated CRLB values under such circumstances are merely the approximated error estimation (de Graaf 2007). Nonetheless, it is generally accepted that metabolite concentrations with less than 10% CRLB values are considered good measurements; values with greater than 10% but less than 20% are considered borderline measurements; values with greater than 20% are considered unreliable measurements. Figure 3-7 shows an example of the output file generated by LCModel. This  $^1\text{H}$  spectrum is collected with the PRESS acquisition technique at the anterior cingulate cortex of a human brain. It is shown that metabolites such as NAA, Cho, Cr, Glu, and Ins (Myo-Inositol) have fairly low CRLB values, whereas the quantification of Gln, GABA, NAAG, Ala, Asp, Tau, Lac, and Glucose have very high CRLB values. The high %SD values (CRLB) for Gln, GABA, and NAAG are mainly caused by the fact that their resonance peaks strongly overlap with other metabolites with higher signal amplitudes. Ala, Asp, Tau, Lac, and Glucose have very low *in vivo* concentrations, so the quantification of these metabolites is more challenging. Generally, for overlapping metabolite pairs like NAA and NAAG, Glu and Gln, Cr and PCr, GPC and Cho, the CRLB values are lower for the pairs than that of each individual metabolite. For instance, since Cr and PCr strongly overlap with each other, it is more accurate to quantify Cr and PCr together than just Cr or PCr by itself. As shown in Figure 3-7, the CRLB values for Cr and PCr are 23% and 12%, but the CRLB for Cr+PCr is only 3%, thus, it is more reliable to report the Cr+PCr concentration than just the Cr or PCr concentration. In the case of Glu and Gln, the CRLB values

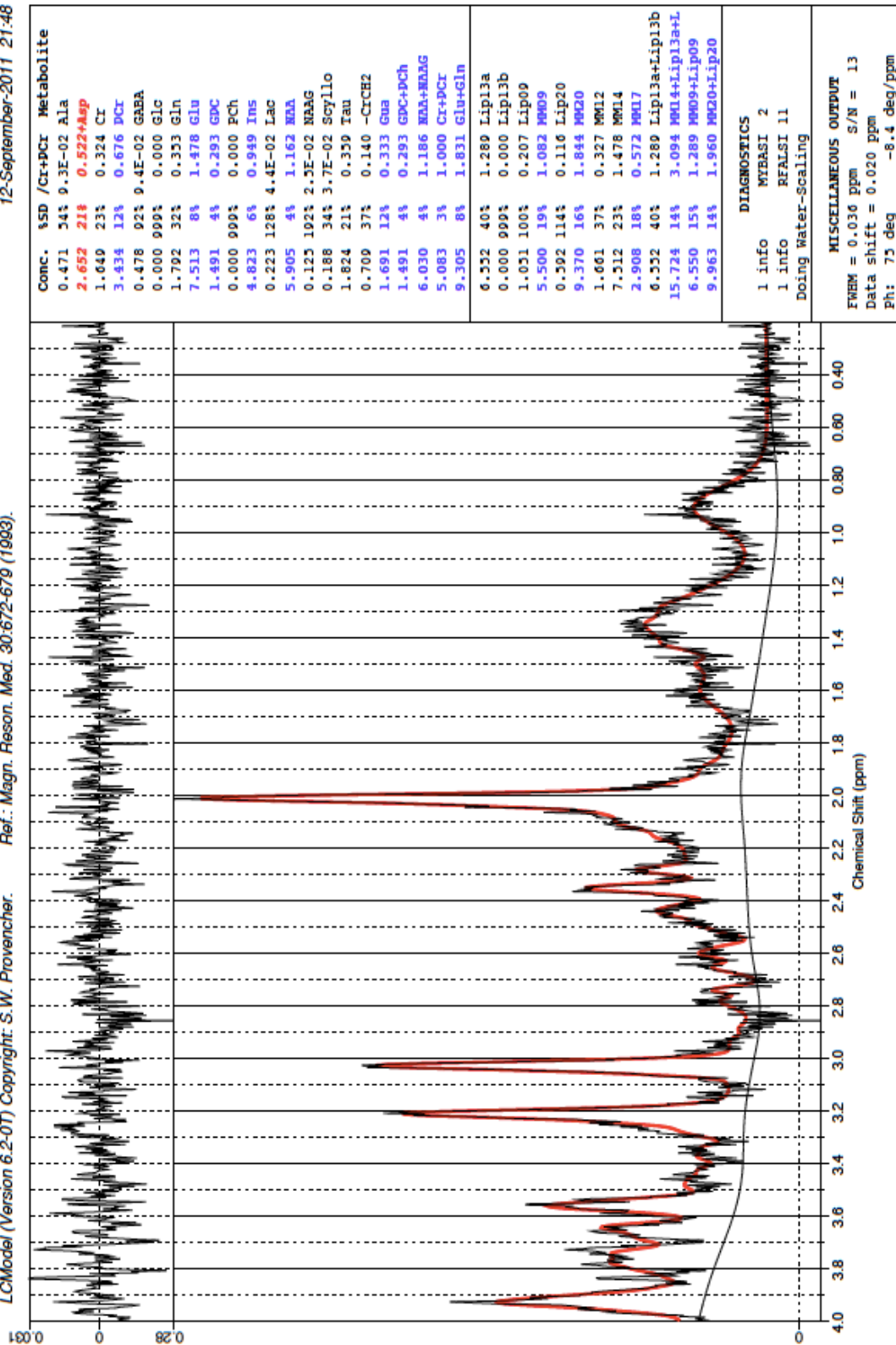


Figure 3-7: An example output file from the LCModel software.

for Glu and Gln are 8% and 32% and the CRLB value for Glu+Gln is also 8%, so one might be tempted to just subtract the Glu concentration from that of Glu+Gln to obtain Gln concentration. This subtraction practice is incorrect way of obtaining Gln values. The low CRLB value for Glu+Gln is because of the contribution from Glu, so one cannot perform simple subtractions to obtain overlapping metabolite concentrations. The 32% CRLB value of Gln indicates that the quantification of Gln is unreliable and there is simply nothing one can do about the high CRLB value.

## **<sup>1</sup>H-MRS in Psychiatric Disorders**

### **Depression**

<sup>1</sup>H-MRS has a variety of acquisition methods and reliable spectral quantification software suitable to detect and measure in vivo neurometabolite concentrations. Hence, it is a promising technique to evaluate neurometabolite concentration differences in various neurological and psychiatric diseases. Major Depressive Disorder (MDD) is a severe and prevalent medical condition with an unknown underlying disease mechanism. The hypothesis of Glutamatergic and GABAergic neurotransmission imbalance in MDD patients has been recently accepted as an encouraging proposition for the development of alternative pharmacological interventions for MDD.

There have been many <sup>1</sup>H-MRS studies on MDD. The majority of them have reported decreased Glu or Glu+Gln (Glx) levels in MDD patients (Auer et al. 2000; Pfeleiderer et al. 2003; Mirza et al. 2004); the Glu and Glx levels are reported to increase with either monoamine antidepressant or electroconvulsive therapy (ECT) treatments. Auer et al. reported a 10.4% decrease in Glu concentration and a 14.3% decrease in Glx concentration in patients with MDD compared to healthy controls in the anterior cingulate (AC) region using a PRESS (TE/TR =



35/2000 ms) single voxel technique on a 1.5 T GE scanner (Auer et al. 2000). Pfleiderer et al. also reported decreased levels of Glx in MDD patients at the AC region using a STEAM (TE/TR = 20/2500 ms) pulse sequence on a 1.5 T Siemens scanner; they also reported an increase of 70.6% on the Glx concentration in MDD patients who have responded to ECT treatments (Pfleiderer et al. 2003). This same group also reported decreased Glx levels at the amygdala and hippocampus regions in MDD patients using the same acquisition protocol (Michael et al. 2003). In 2004, Mirza et al. reported decreased Glx concentration in MDD pediatric patients at the AC region using a PRESS (TE/TR = 30/3000 ms) acquisition method on a 1.5 T GE scanner (Mirza et al. 2004). One year later, reduced AC region Glu concentration in pediatric MDD patients was again reported by Rosenberg et al. using a 1.5 T GE scanner with PRESS acquisition (Rosenberg et al. 2005).

Few have reported in vivo GABA concentrations in MDD patients due to its technical challenges. However, in 1999, Sanacora et al. first reported reduced GABA concentrations in the occipital cortex in MDD patients compared to normal controls using a homonuclear J-difference editing technique (TE/TR = 68/3390 ms) on a 2.1 T Bruker scanner (Sanacora et al. 1999). Three years later, the same group reported increased GABA level in MDD patients after treatments with antidepressants (Sanacora et al. 2002). In the subsequent year, this group also reported elevated GABA levels in MDD patients after ECT treatment with the same MRS acquisition protocol (Sanacora et al. 2003). More recently, Hasler et al., using also the J-difference editing technique (TE/TR = 68/1500 ms) on a 3 T GE scanner, measured GABA and Glx concentration in healthy controls and MDD patients and they reported both reduced amount of GABA and Glx at the dorsomedial prefrontal region (Hasler et al. 2007). Price et al. investigated GABA and Glx concentrations in treatment resistant MDD patients and they have shown that GABA is

decreased in the antidepressant treatment resistant MDD patients compared to healthy controls and nontreatment resistant MDD patients at the occipital lobe region (Price et al. 2009). Their findings suggest that amino acid neurotransmission modulating antidepressant could be a potential treatment to monoamine antidepressant resistant patients.

### Autism Spectrum Disorder

Despite numerous MRS studies on ASD, only one has reported GABA level reduction in pediatric ASD patients with detailed MRS acquisition description (Harada et al, 2010; Kubas et al, 2012), and few other have reported Glu or Glx (Glu + Gln) values in ASD (Page et al, 2006; DeVito et al, 2007; Bernardi et al, 2011; Bejjani et al, 2012; Joshi et al, 2012).

Of the above mentioned studies, DeVito et al reported **decreased** levels of Glx in medicated ASD children in the frontal lobe, cerebellum, and the occipital lobe using a multi-slice spin-echo MRSI sequence with slice-selective adiabatic inversion for extra-cranial lipid suppression at 3 T (TI/TE/TR = 230/135/1800 ms, field-of-view (FOV) = 280 mm, 35 x 35 circular k-space sampling, 2 kHz bandwidth, 512-msec readout; 30-min scan time); Bernardi et al reported **decreased** Glx in non-medicated ASD adults at the anterior cingulate (AC) using a MRSI sequence at 3 T (TE/TR = 30/2000 ms, FOV = 240 mm, 24 x 24 circular k-space sampling, 10 mm of slice thickness); Page et al reported **increased** Glx levels in ASD adults at the amygdala-hippocampus complex using single voxel PRESS sequence at 1.5 T (TE/TR = 35/30000, 160 averages); Bejjani et al reported **elevated** Glx level in both medicated and non-medicated ASD children at the AC region using single voxel PRESS sequence (TE/TR = 25/1500, 256 averages) and a MRSI sequence at 1.5 T (TE/TR = 30/1500). Joshi et al also reported **elevated** Glx levels in ASD adolescents in the AC region using a two-dimensional J-resolved PRESS sequence at 4 T (TE = 20 – 250 ms, step size 20 ms, TR = 2000 ms, 16 averages

per step). Harada et al reported reduced GABA concentrations in sedated ASD children at the frontal lobe region using a MEGA-PRESS sequence at 3 T (TE/TR = 68/2500 ms, 256 averages, 27 cc voxel size). Kubas et al has reported decreased frontal lobe GABA to creatine (Cr) ratios in autistic children using single voxel PRESS sequence at 1.5 T. In summary, out of total of five MRS studies on Glx, two have reported decreased Glx levels in human brain, and three have reported increased Glx levels instead.

A variety of MRS acquisition methods have been employed in the past to study the GABAergic and glutamatergic systems in ASD patients, sometimes with conflicting reports in the metabolite levels. The variability in findings is likely caused by the methodology differences in acquisition and quantification steps of these studies. Different acquisition parameters such as the TE and the magnetic field strength greatly affect the characteristics of a MR spectrum and hence disturb the accuracy of the quantification of certain metabolites. Thus, it is important to investigate and determine the accuracy and reproducibility of these MRS methods used to measure Glu, Gln, and GABA in the autistic pediatric population. This can be accomplished using numerical simulation and phantoms with known concentrations, so that systematic comparisons can be made to reveal an optimal method.

## Conclusion

This chapter identifies the commonly NMR observable neurometabolites and their *in vivo* concentrations. The presence of brain macromolecule resonance signals in a  $^1\text{H}$  NMR spectrum is also examined. Glu, Gln, and GABA  $^1\text{H}$  NMR spectra are introduced. A brief overview of the NMR signal quantification techniques is given in the second part of this chapter with specific focus on the frequency domain prior-knowledge based software LCModel. The last part of this chapter serves as a  $^1\text{H}$ -MRS application review in the detection of Glu, Gln, and GABA in MDD

and ASD. Various research groups using different MRS acquisition methods have made consistent reports of reduced GABA, Glu, and Glx levels in MDD patients. In contrast, different research groups have made conflicting reports on Glu and Glx concentrations in ASD studies using MRS.

## References

- Auer, D. P., Putz, B., Kraft, E., Lipinski, B., Schill, J., & Holsboer, F. (2000). Reduced glutamate in the anterior cingulate cortex in depression: an in vivo proton magnetic resonance spectroscopy study. *Biol Psychiatry*, *47*, 305-13.
- Behar, K. L., Rothman, D. L., Spencer, D. D., & Petroff, O. A. C. (1994). Analysis of macromolecule resonances in <sup>1</sup>H NMR spectra of human brain. *Magnetic Resonance in Medicine*, *32*, 294-302.
- Bejjani, A., O'Neill, J., Kim, J. A., Frew, A. J., Yee, V. W., Ly, R., Kitchen, C., Salamon, N., McCracken, J. T., Toga, A. W., Alger, J. R., & Levitt, J. G. (2012). Elevated glutamatergic compounds in pregenual anterior cingulate in pediatric autism spectrum disorder demonstrated by <sup>1</sup>H MRS and <sup>1</sup>H MRSI. *PLoS One*, *7*, e38786.
- Bernardi, S., Anagnostou, E., Shen, J., Kolevzon, A., Buxbaum, J. D., Hollander, E., Hof, P. R., & Fan, J. (2011). In vivo <sup>1</sup>H-magnetic resonance spectroscopy study of the attentional networks in autism. *Brain Res*, *1380*, 198-205.
- Choi, C., Coupland, N. J., Bhardwaj, P. P., Malykhin, N., Gheorghiu, D., & Allen, P. S. (2006). Measurement of brain glutamate and glutamine by spectrally-selective refocusing at 3 tesla. *Magnetic Resonance in Medicine*, *55*, 997-1005.
- De Graaf, A. A., Van Dijk, J. E., & BoéE, W. M. M. J. (1990). Quality: quantification improvement by converting lineshapes to the lorentzian type. *Magnetic Resonance in Medicine*, *13*, 343-57.
- DeVito, T. J., Drost, D. J., Neufeld, R. W., Rajakumar, N., Pavlosky, W., Williamson, P., & Nicolson, R. (2007). Evidence for cortical dysfunction in autism: a proton magnetic resonance spectroscopic imaging study. *Biol Psychiatry*, *61*, 465-73.
- Govindaraju, V., Basus, V. J., Matson, G. B., & Maudsley, A. A. (1998). Measurement of chemical shifts and coupling constants for glutamate and glutamine. *Magn Reson Med*, *39*, 1011-3.
- Govindaraju, V., Young, K., & Maudsley, A. A. (2000). Proton NMR chemical shifts and coupling constants for brain metabolites. *NMR Biomed*, *13*, 129-53.

- Graaf, R. A. d. (2007). *In vivo NMR Spectroscopy: Principles and Techniques*: John Wiley & Sons, Ltd.
- Graverondemilly, D., Diop, A., Briguët, A., & Fenet, B. (1993). Product-Operator Algebra for Strongly Coupled Spin Systems. *Journal of Magnetic Resonance, Series A*, *101*, 233-39.
- Harada, M., Taki, M. M., Nose, A., Kubo, H., Mori, K., Nishitani, H., & Matsuda, T. (2011). Non-invasive evaluation of the GABAergic/glutamatergic system in autistic patients observed by MEGA-editing proton MR spectroscopy using a clinical 3 tesla instrument. *J Autism Dev Disord*, *41*, 447-54.
- Hasler, G., van der Veen, J. W., Tumonis, T., Meyers, N., Shen, J., & Drevets, W. C. (2007). Reduced prefrontal glutamate/glutamine and gamma-aminobutyric acid levels in major depression determined using proton magnetic resonance spectroscopy. *Arch Gen Psychiatry*, *64*, 193-200.
- Joshi, G., Biederman, J., Wozniak, J., Goldin, R. L., Crowley, D., Furtak, S., Lukas, S. E., & Gonenc, A. (2012). Magnetic resonance spectroscopy study of the glutamatergic system in adolescent males with high-functioning autistic disorder: a pilot study at 4T. *Eur Arch Psychiatry Clin Neurosci*.
- Kanowski, M., Kaufmann, J., Braun, J., Bernarding, J., & Tempelmann, C. (2004). Quantitation of simulated short echo time 1H human brain spectra by LCMoDel and AMARES. *Magn Reson Med*, *51*, 904-12.
- Kubas, B., Kulak, W., Sobaniec, W., Tarasow, E., Lebkowska, U., & Walecki, J. (2012). Metabolite alterations in autistic children: a 1H MR spectroscopy study. *Adv Med Sci*, *57*, 152-6.
- Michael, N., Erfurth, A., Ohrmann, P., Gossling, M., Arolt, V., Heindel, W., & Pfleiderer, B. (2003). Acute mania is accompanied by elevated glutamate/glutamine levels within the left dorsolateral prefrontal cortex. *Psychopharmacology (Berl)*, *168*, 344-6.
- Mirza, Y., Tang, J., Russell, A., Banerjee, S. P., Bhandari, R., Ivey, J., Rose, M., Moore, G. J., & Rosenberg, D. R. (2004). Reduced anterior cingulate cortex glutamatergic concentrations in childhood major depression. *J Am Acad Child Adolesc Psychiatry*, *43*, 341-8.
- Naressi, A., Couturier, C., Castang, I., de Beer, R., & Graveron-Demilly, D. (2001). Java-based graphical user interface for MRUI, a software package for quantitation of in vivo/medical magnetic resonance spectroscopy signals. *Comput Biol Med*, *31*, 269-86.
- Page, L. A., Daly, E., Schmitz, N., Simmons, A., Toal, F., Deeley, Q., Ambery, F., McAlonan, G. M., Murphy, K. C., & Murphy, D. G. (2006). In vivo 1H-magnetic resonance spectroscopy study of amygdala-hippocampal and parietal regions in autism. *Am J Psychiatry*, *163*, 2189-92.

- Pfeuffer, J., Tkac, I., Provencher, S. W., & Gruetter, R. (1999). Toward an in vivo neurochemical profile: quantification of 18 metabolites in short-echo-time  $^1\text{H}$  NMR spectra of the rat brain. *J Magn Reson*, *141*, 104-20.
- Pfleiderer, B., Michael, N., Erfurth, A., Ohrmann, P., Hohmann, U., Wolgast, M., Fiebich, M., Arolt, V., & Heindel, W. (2003). Effective electroconvulsive therapy reverses glutamate/glutamine deficit in the left anterior cingulum of unipolar depressed patients. *Psychiatry Res*, *122*, 185-92.
- Pouillet, J. B., Sima, D. M., & Van Huffel, S. (2008). MRS signal quantitation: a review of time- and frequency-domain methods. *J Magn Reson*, *195*, 134-44.
- Price, R. B., Shungu, D. C., Mao, X., Nestadt, P., Kelly, C., Collins, K. A., Murrough, J. W., Charney, D. S., & Mathew, S. J. (2009). Amino acid neurotransmitters assessed by proton magnetic resonance spectroscopy: relationship to treatment resistance in major depressive disorder. *Biol Psychiatry*, *65*, 792-800.
- Provencher, S. W. (1982). A constrained regularization method for inverting data represented by linear algebraic or integral equations. *Computer Physics Communications*, *27*, 213-27.
- Provencher, S. W. (1993). Estimation of metabolite concentrations from localized in vivo proton NMR spectra. *Magn Reson Med*, *30*, 672-9.
- Sanacora, G., Mason, G. F., Rothman, D. L., Behar, K. L., Hyder, F., Petroff, O. A., Berman, R. M., Charney, D. S., & Krystal, J. H. (1999). Reduced cortical gamma-aminobutyric acid levels in depressed patients determined by proton magnetic resonance spectroscopy. *Arch Gen Psychiatry*, *56*, 1043-7.
- Sanacora, G., Mason, G. F., Rothman, D. L., Hyder, F., Ciarcia, J. J., Ostroff, R. B., Berman, R. M., & Krystal, J. H. (2003). Increased cortical GABA concentrations in depressed patients receiving ECT. *Am J Psychiatry*, *160*, 577-9.
- Sanacora, G., Mason, G. F., Rothman, D. L., & Krystal, J. H. (2002). Increased occipital cortex GABA concentrations in depressed patients after therapy with selective serotonin reuptake inhibitors. *Am J Psychiatry*, *159*, 663-5.
- Snyder, J., Thompson, R. B., & Wilman, A. H. (2010). Difference spectroscopy using PRESS asymmetry: application to glutamate, glutamine, and myo-inositol. *NMR Biomed*, *23*, 41-47.
- Thompson, R. B., & Allen, P. S. (1998). A new multiple quantum filter design procedure for use on strongly coupled spin systems found in vivo: Its application to glutamate. *Magnetic Resonance in Medicine*, *39*, 762-71.
- Van Boogaart, A. D., Howe, F. A., Rodrigues, L. M., Stubbs, M., & Griffiths, J. R. (1995). In vivo  $^31\text{p}$  mrs: absolute concentrations, signal-to-noise and prior knowledge. *NMR Biomed*,

8, 87-93.

van der Veen, J. W. C., de Beer, R., Luyten, P. R., & van Ormondt, D. (1988). Accurate quantification of in vivo  $^3\text{P}$  NMR signals using the variable projection method and prior knowledge. *Magnetic Resonance in Medicine*, 6, 92-98.

Vanhamme, L., van den Boogaart, A., & Van Huffel, S. (1997). Improved method for accurate and efficient quantification of MRS data with use of prior knowledge. *J Magn Reson*, 129, 35-43.

Zaaraoui, W., Fleysheer, L., Fleysheer, R., Liu, S., Soher, B. J., & Gonen, O. (2007). Human brain-structure resolved T2 relaxation times of proton metabolites at 3 tesla. *Magnetic Resonance in Medicine*, 57, 983-89.

## **Chapter 4 PEPSI Investigation in Children and Adolescents with Attention Deficit Hyperactivity Disorder**

### **Introduction**

Attention deficit hyperactivity disorder (ADHD) is the most commonly diagnosed psychiatric disorder in children. Symptoms of ADHD can persist into adolescence and adulthood causing debilitating dysfunctions in school performance, social relationships, employment status, substance abuse and other significant psychiatric conditions. There are three subtypes of ADHD: predominantly hyperactive-impulsive, predominantly inattentive, and predominantly hyperactive-impulsive and inattentive (DSM-IV). The worldwide prevalence of ADHD is estimated at about 5.3% in children and adolescents (Polanczyk et al. 2007). ADHD is more commonly diagnosed in boys than girls (Pastor and Reuben 2008). Approximately 20%-30% of the ADHD children and adolescents will continue to experience ADHD symptoms during their adulthood (Muglia et al. 2000) and estimates indicate that 2.5%-4.4% of the adult population meet the diagnostic criteria for ADHD (Kessler et al. 2006; Fayyad et al. 2007; Simon et al. 2009).

The underlying causes of ADHD are still poorly understood, but it is generally believed that ADHD is the result of both genetic and environmental factors. Studies have shown that maternal lifestyle in cigarette smoking and alcohol abuse are potential risk factors for children to develop ADHD (Mick et al. 2002; Linnet et al. 2003). ADHD has a high degree of comorbidity with other psychiatric disorders; such as childhood conduct disorder (Faraone et al. 2007), unipolar affective disorder (Biederman et al. 2009), bipolar disorder (Biederman et al. 2003; Masi et al. 2006), and autism spectrum disorder (Reiersen et al. 2008). Although the genetic



architecture of ADHD is complex, researchers have identified several monoamine neurotransmission related genes that are associated with ADHD (Faraone et al. 2005; Sharp et al. 2009). Currently, the abnormal dopaminergic and serotonergic neurotransmission in ADHD patients has been the main focus of the disease etiology (Biederman et al. 2005). Since dopamine plays central role in the regulation of glutamatergic and GABAergic neurotransmission, a hypofunctioning of the dopaminergic pathways should result in an altered *in vivo* concentration of Glutamate (Glu), Glutamine (Gln), and  $\gamma$ -Aminobutyric acid (GABA).

Proton magnetic resonance spectroscopy ( $^1\text{H-MRS}$ ) is the only non-invasive analytical technique that enables *in vivo* metabolite measurement and quantification in human brains. It is considered well suited for investigating the biochemical aspect of psychiatric disorders in children and adolescents. Traditional single voxel point resolved spectroscopy (PRESS) is the most frequently used MRS acquisition method for neuropsychiatric research in ADHD studies, Few studies have reported significant differences in concentration values in terms of absolute neurometabolite quantifications (Hesslinger et al. 2001; Carrey et al. 2007; Yang et al. 2010). We present here a study using a fast multi-voxel spectroscopic imaging technique based on the concept of echo planar acquisition method (Posse et al. 1995) called the proton echo planar spectroscopic imaging (PEPSI). PEPSI acquisition offers shorter acquisition time using echo planar read out gradients to simultaneously encode for both spatial and spectral information. We aimed to identify neurometabolite concentration differences between healthy control subjects and ADHD children and adolescents using short echo time single slice PEPSI acquisition at three brain regions: the anterior cingulate cortex (AC), the basal ganglia region (BG), and the supraventricular region (SUPV).

## Methods and Materials

### MRI/MRS Acquisition

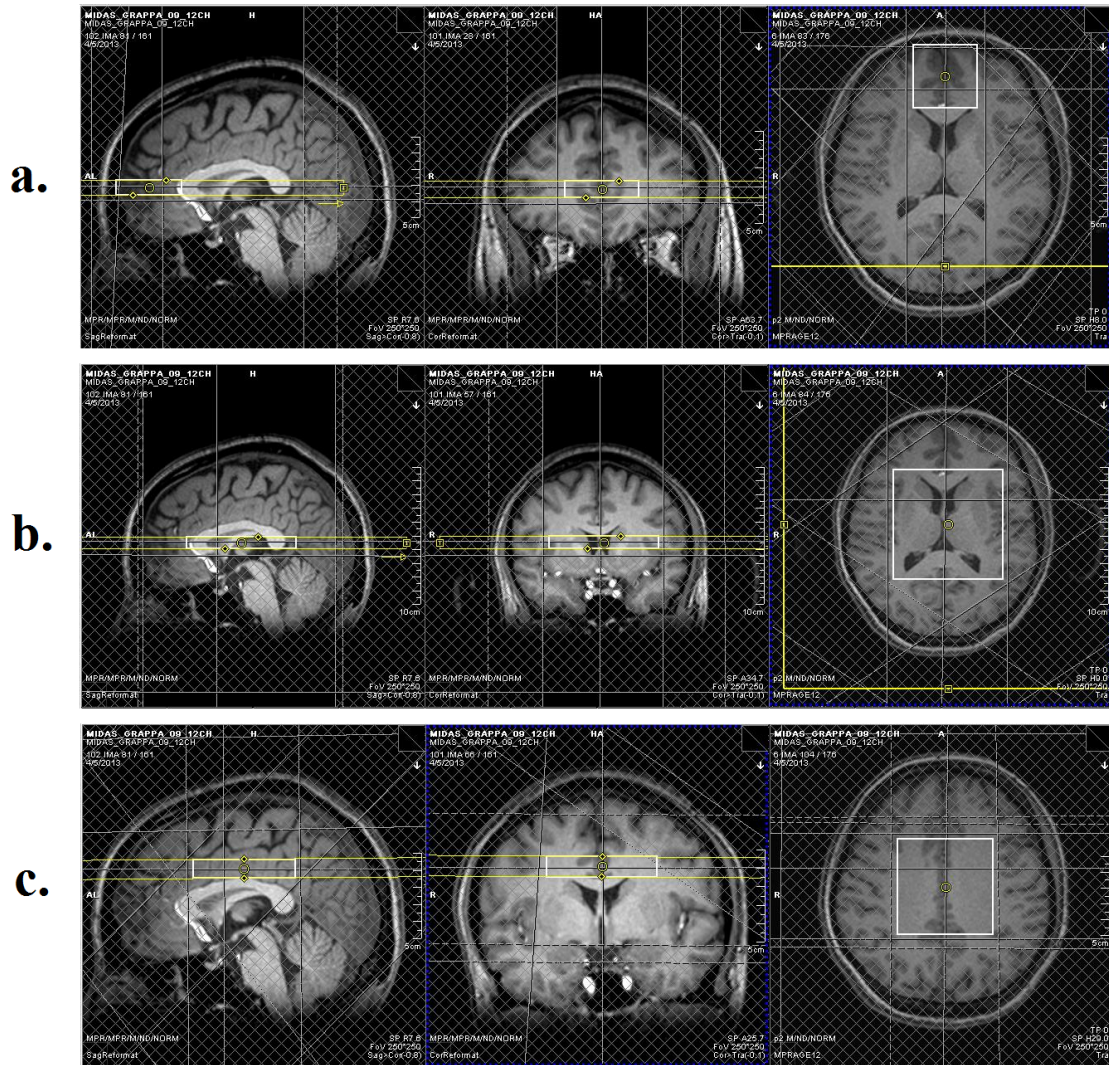


Figure 4-1: PEPSI slice placements in (a) the anterior cingulate cortex, (b) the basal ganglia region, and (c) the supraventricular region using a 3D whole brain T1-weighted MRI acquisition.

All MRI and MRSI data were collected on a Siemens MAGNETOM Trio Tim 3T scanner (Siemens Healthcare, Erlangen, Germany) with a 12-channel phased-array head coil. The study protocol includes an axial 3D whole-brain T1-weighted magnetization prepared gradient echo (MPRAGE) acquisition (TR/TE = 1900/3.26 ms, voxel size =  $1 \times 1 \times 1 \text{ mm}^3$ , iPAT mode =

GRAPPA, scan time of 4 minutes) and three sets of PEPSI water suppressed and water reference acquisitions at the AC, BG, and SUPV regions. The whole brain MPRAGE images were reformatted into the coronal and the sagittal orientations for PEPSI slice placement. Water suppressed PEPSI spectra (TR/TE=2000/15 ms, voxel size of 7.5x7.5x9 mm<sup>3</sup>, matrix size=32x32, 1024 spectral data points, scan time of 8 minutes) were acquired using automatic shim adjustment. Extra cranial lipid signals were suppressed using six outer volume suppression saturation bands in the axial plane and one in the sagittal plan. A one minute water-reference spectrum was also collected prior to each water-suppressed acquisition. Examples of the PEPSI slice placement at the AC, BG, and SUPV region are shown in Figure 4-1. The white box indicates the spectral acquisition volume and the shim adjustment volume.

### Post-processing

PEPSI raw data were collected to offline using the Siemens TWIX software. Raw spectral data were reconstructed with an in-house processing pipeline written in IDL (Exelis Visual Information Solution, Boulder, USA). The data reconstruction process includes phase correction, weighted phase array combination, and automatic spectroscopy slice registration with MRI volume of interests (VOIs). Automated brain VOI segmentation was done using the FreeSurfer software package (Dale et al. 1999; Fischl et al 2002). A list of the neuroanatomical VOIs segmented by FreeSurfer is presented in Table 4-1. Due to the larger PEPSI voxel size in contrast to the MRI voxel size, only voxels that contain high VOI percentages are selected in the PEPSI slices and the cutoff percentage values are also listed in Table 4-1. Using the FreeSurfer build-in atlas, four anatomical regions can be identified at the PEPSI AC slab acquisition. They are the left and right superior frontal lobe (SFL) and the left and right rostral anterior cingulate cortex (dACC). Six VOIs can be identified at the BG slice. They are the bilateral caudate nuclei,

putamen, and the thalamus. At the SUPV slice, six more VOIs can be identified. They are the left and right caudal anterior cingulate cortex (vACC), left and right posterior cingulate cortex (PCC), and the left and right precuneus (PC). Figure 4-2 shows examples of VOIs overlaying with the whole-brain MRI images at all three slabs. The final reconstructed time domain data were output into LCModel (Provencher 1993) raw file format for spectral quantification. To ensure that differences in tissue content did not account for metabolite effects between subject groups, the gray matter, white matter and CSF composition of each PEPSI voxel was determined by co-registering FSL FAST (Zhang et al. 2001) segmented whole brain tissue masks onto the PEPSI slab voxels, as shown in figure 4-3.

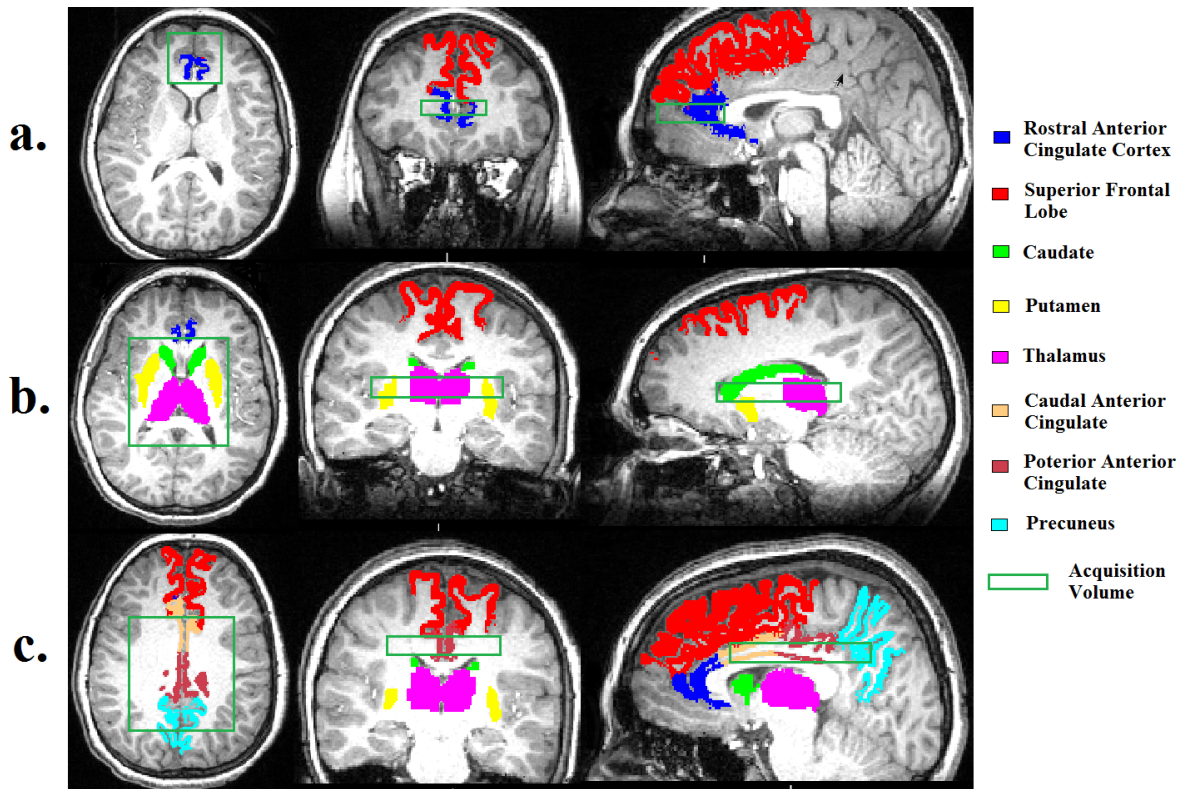


Figure 4-2: FreeSurfer VOIs overlaying T1-weighted MPRAGE images and the corresponding PEPSI acquisition volume.



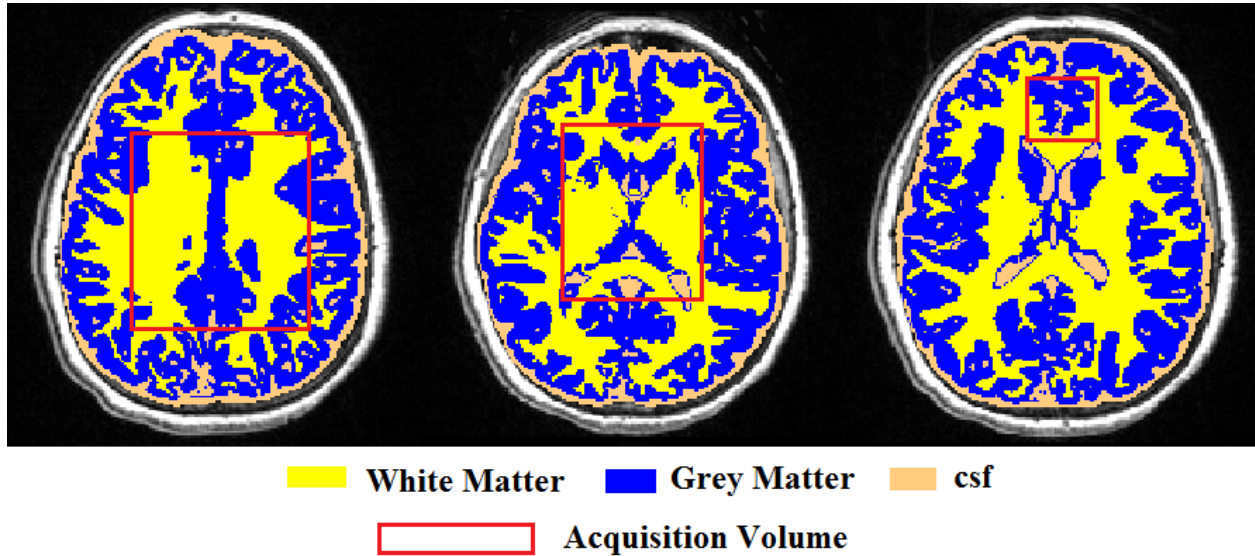


Figure 4-3: FSL FAST tissue segmentation and PEPSI acquisition volumes.

Slice Location	Anatomical VOI	Cutoff Percentage
AC	Left and Right Superior Frontal Lobe	30%
	Left and Right Rostral Anterior Cingulate Cortex	30%
BG	Left and Right Caudate	40%
	Left and Right Putamen	60%
	Left and Right Thalamus	70%
SUPV	Left and Right Caudal Anterior Cingulate Cortex	30%
	Left and Right Posterior Cingulate Cortex	30%
	Left and Right Precuneus	30%

Table 4-1: Anatomical VOIs and their cutoff values for each slab.

PEPSI spectral quantification was performed with LCModel (version 6.20) using GAMMA (Smith et al. 1994) simulated spin echo based TE15 basis-sets. Eddy current correction and water scaling were performed using the water non-suppressed PEPSI spectral data. Compounds that can be identified with PEPSI acquisition and LCModel with lower than 20% Cramer-Rao lower bound (CRLB) included the total NAA (N-acetylaspartate + Nacetylaspartylglutamate), total creatine (creatine + phosphocreatine), total choline (glycerophosphorylcholine + phosphorylcholine), Glu, Glx (glutamate + glutamine) and myo-

inositol (Myo). CSF corrected absolute metabolite concentrations were calculated voxel by voxel using the FSL tissue segmentation masks to obtain PEPSI voxel CSF content. Spectral quality control was performed by excluding voxel spectra having Cr signal with SNR < 4 and/or FWHM > 0.1 ppm. The LCModel absolute concentration values were averaged together for voxels that satisfied the quality control criteria and had CRLB values < 20%. Hence, Myo-inositol, Glu, and Glx concentration values were not included in group analysis due to the relatively high number of subjects who had CRLB values greater than 20%, which is considered as unreliable quantifications. The voxel concentrations was determined for all 16 anatomical VOIs listed in Table 4-1. Total three water-scaled absolute neurometabolite concentrations at 16 different anatomical regions are recorded for statistical analysis.

## Subjects

The participants of this study were neither sedated nor on medication during the time of their MRI scanning. The ADHD subjects were asked to be off of their medications 24 hours prior to their scheduled MRI scans. A total sample of 70 ADHD and 40 healthy control subjects were recruited from the community or referred by physicians at the University of California Los Angeles (UCLA). Subject age ranged from 6 to 18 years old. A psychologist or a psychiatrist diagnosed all ADHD patients according to the DSM-IV criteria for ADHD. Cognitive functioning of all subjects was assessed with Block design and Vocabulary subtest of the Wechsler Intelligence Scale for Children (WISC-III) or the Wechsler Adult Intelligence Scale (WAIS-III). Subjects who had any other type of neurological disorders, head injury resulting in concussion or unconsciousness, premature birth, estimated full scale IQ lower than 70, premature birth or any contradictions to MRI studies were excluded. A total of 43 males and 27 females were recruited for the ADHD group with a mean age of 12.4 years old (SD = 3.2 years old, age

ranged from 6 to 18 years old) and mean IQ score of 104 (SD = 16.4, IQ score ranged from 74 to 152). The control group was composed of 17 males and 23 females with a mean age of 13.1 years old (SD = 3.9 years old, age ranged from 8 to 17 years old) and a mean WASI IQ score of 110.4 (SD = 12.6, IQ score ranged from 83 to 138). This study was approved by the Institutional Review Board of UCLA. Informed consents were obtained from the parents or guardians of the child or adolescent participants.

### Statistical Analysis

Statistical analysis of diagnosis effects on absolute neurometabolite concentration was carried out in R 3.0.0 (R Development Core Team, 2012). Group differences in concentration were tested with analysis of covariance (ANCOVA) with age and age-by-diagnosis interaction covariates. A p-value threshold of 0.05 after post hoc false discovery rate (FDR) (Benjamin and Hochberg, 1995) multiple comparison adjustment was used as the criterion of statistical significance.

### Results

Table 4-2 and 4-3 summarizes the means and comparisons of absolute metabolite concentrations for the total choline, total creatine, total NAA, Glu, Glx, and Myo for ADHD and healthy control subjects by diagnosis effects. The levels of metabolites have the units of miller Molar (mMol). We found that the ADHD subjects have a significantly lower mean total choline concentration at the left posterior cingulate cortex region than the healthy controls ( $P = 0.042$ , FDR corrected). No other significant differences in metabolite levels were found between groups. Figure 4-4 shows an example PEPSI spectrum after being fitted by the LCModel software. Figure 4-5 shows the density and histogram plots of the total Choline level distribution between ADHD and healthy control subjects in the left posterior cingulate cortex.

PEPSI Slab Locations	Anatomical VOIs	Metabolites	ADHD Subjects (mMol)		Controls (mMol)		P-value	FDR P-value
			Mean	SD	Mean	SD		
SUPV	Left vACC	tCho	3.55	0.65	3.72	0.61	0.840	0.875
		tCr	12.79	2.33	13.58	1.49	0.875	0.875
		tNAA	13.43	3.41	16.19	1.46	0.718	0.875
	Right vACC	tCho	3.45	0.68	3.68	0.54	0.683	0.875
		tCr	12.72	2.36	13.59	0.85	0.863	0.875
		tNAA	13.15	3.37	15.68	0.79	0.805	0.875
	Left PCC	tCho	<b>2.89</b>	<b>0.41</b>	<b>3.08</b>	<b>0.32</b>	<b>0.002</b>	<b>0.042</b>
		tCr	12.35	1.31	12.92	1.19	0.310	0.784
		tNAA	14.62	3.18	15.95	2.90	0.324	0.784
	Right PCC	tCho	2.82	0.45	3.12	0.45	<b>0.039</b>	0.348
		tCr	12.05	1.63	13.15	1.45	0.658	0.875
		tNAA	14.18	3.07	15.84	2.75	0.303	0.784
	Left PC	tCho	2.60	0.54	2.69	0.24	0.260	0.784
		tCr	13.37	2.31	13.38	1.09	0.829	0.875
		tNAA	16.27	3.98	16.89	3.46	0.527	0.875
	Right PC	tCho	2.69	0.46	2.78	0.39	0.093	0.560
		tCr	12.97	1.80	13.41	1.69	0.858	0.875
		tNAA	15.49	3.78	16.62	3.41	0.348	0.784
AC	Left SFL	tCho	3.44	1.03	3.54	0.73	0.523	0.784
		tCr	12.26	2.35	12.53	2.31	0.890	0.890
		tNAA	11.53	4.41	10.12	2.14	0.529	0.706
	Right SFL	tCho	3.56	0.64	3.57	0.88	0.105	0.420
		tCr	13.73	3.80	12.52	1.56	0.825	0.899
		tNAA	10.75	4.91	10.43	0.79	0.574	0.689
	Left dACC	tCho	3.68	1.19	3.87	0.85	0.220	0.528
		tCr	12.19	2.35	12.79	2.22	0.400	0.687
		tNAA	10.32	3.91	10.82	2.87	<b>0.032</b>	0.389
	Right dACC	tCho	3.65	0.74	3.85	0.94	0.242	0.484
		tCr	11.38	2.12	12.30	2.83	0.153	0.459
		tNAA	9.54	3.74	9.27	3.07	0.043	0.257
BG	Left Putamen	tCho	2.70	0.53	2.88	0.40	0.772	0.829
		tCr	11.28	1.27	11.95	1.58	0.771	0.829
		tNAA	9.07	2.36	10.33	3.08	0.257	0.829
	Right Putamen	tCho	2.78	0.51	2.92	0.39	0.334	0.829
		tCr	10.78	1.60	11.89	1.57	0.471	0.829
		tNAA	8.99	2.61	9.46	3.58	0.477	0.829
	Left Caudate	tCho	3.26	0.74	3.20	0.71	0.783	0.829
		tCr	12.24	2.68	11.57	3.03	0.998	0.998
		tNAA	9.26	3.11	9.44	3.58	0.692	0.829
	Right Caudate	tCho	3.37	0.62	3.17	0.80	0.674	0.829
		tCr	12.06	2.10	11.86	2.57	0.370	0.829
		tNAA	9.43	2.77	8.36	3.25	0.529	0.829
	Left Thalamus	tCho	3.16	0.61	3.53	0.65	<b>0.014</b>	0.252
		tCr	10.35	2.05	11.47	2.25	0.389	0.829
		tNAA	8.68	2.54	10.71	3.50	0.115	0.829
	Right Thalamus	tCho	3.22	0.46	3.44	0.47	0.143	0.829
		tCr	10.63	1.60	11.52	2.01	0.588	0.829
		tNAA	8.92	2.55	10.81	3.02	0.228	0.829

Table 4-2: SUPV, AC, and BG Slab metabolite level of ADHD and healthy control subjects.



PEPSI Slab Locations	Anatomical VOIs	Metabolites	ADHD Subjects (mMol)		Controls (mMol)		P-value
			Mean	SD	Mean	SD	
<b>SUPV</b>	Left vACC	Glu	NA	NA	NA	NA	NA
		Glx	17.23	5.04	21.35	3.58	0.595
		Myo	11.75	2.52	13.43	1.70	0.331
	Right vACC	Glu	13.27	3.31	14.40	1.94	0.757
		Glx	17.91	4.03	21.35	2.75	0.735
		Myo	12.23	3.24	13.00	2.46	0.648
	Left PCC	Glu	15.05	2.54	15.07	2.71	0.145
		Glx	19.50	3.54	20.03	4.13	0.242
		Myo	11.36	1.51	11.88	1.98	0.713
	Right PCC	Glu	14.63	2.33	15.35	2.23	<b>0.045</b>
		Glx	18.70	3.39	20.32	3.62	0.157
		Myo	11.21	1.75	12.08	1.36	0.941
	Left PC	Glu	16.58	3.71	16.80	2.66	0.205
		Glx	21.51	5.01	21.36	3.10	0.068
		Myo	11.75	1.91	12.32	1.19	0.408
	Right PC	Glu	15.43	2.99	15.55	2.62	0.085
		Glx	20.30	3.95	19.97	3.67	0.053
		Myo	11.73	2.14	12.22	1.73	0.892
<b>AC</b>	Left SFL	Glu	13.43	4.26	10.90	1.48	0.778
		Glx	16.88	4.82	13.08	3.09	0.500
		Myo	12.67	6.40	13.01	3.79	0.990
	Right SFL	Glu	12.18	3.46	12.58	1.22	0.721
		Glx	15.05	4.88	13.82	1.15	0.278
		Myo	12.35	4.85	10.23	2.49	0.484
	Left dACC	Glu	NA	NA	NA	NA	NA
		Glx	13.88	4.15	18.07	4.23	0.196
		Myo	10.89	4.05	11.64	3.15	0.900
	Right dACC	Glu	10.96	2.75	12.70	3.53	<b>0.020</b>
		Glx	14.69	3.41	16.49	4.19	0.209
		Myo	10.13	3.61	11.65	3.53	0.342
<b>BG</b>	Left Putamen	Glu	10.13	2.26	10.73	2.55	0.720
		Glx	13.55	3.20	15.08	3.73	0.609
		Myo	6.73	1.15	6.33	0.60	0.203
	Right Putamen	Glu	9.87	2.40	10.33	2.35	0.479
		Glx	13.31	4.13	12.52	3.21	0.260
		Myo	7.51	0.75	6.72	0.93	0.654
	Left Caudate	Glu	NA	NA	NA	NA	NA
		Glx	15.10	4.57	13.39	4.19	0.546
		Myo	8.86	1.94	7.74	0.31	0.608
	Right Caudate	Glu	11.14	2.85	10.66	2.83	0.168
		Glx	14.58	3.52	13.57	3.85	0.568
		Myo	9.82	2.44	8.62	2.49	0.222
	Left Thalamus	Glu	9.52	1.99	11.87	3.57	0.775
		Glx	12.76	3.14	14.42	4.12	0.649
		Myo	7.87	1.96	8.93	1.74	0.136
	Right Thalamus	Glu	9.81	1.72	11.35	2.89	0.113
		Glx	12.45	2.74	14.93	3.58	0.238
		Myo	7.89	1.33	8.92	1.24	0.094

Table 4-3: SUPV, AC, and BG Slab Glu, Glx, and Myo levels of ADHD and healthy control subjects.

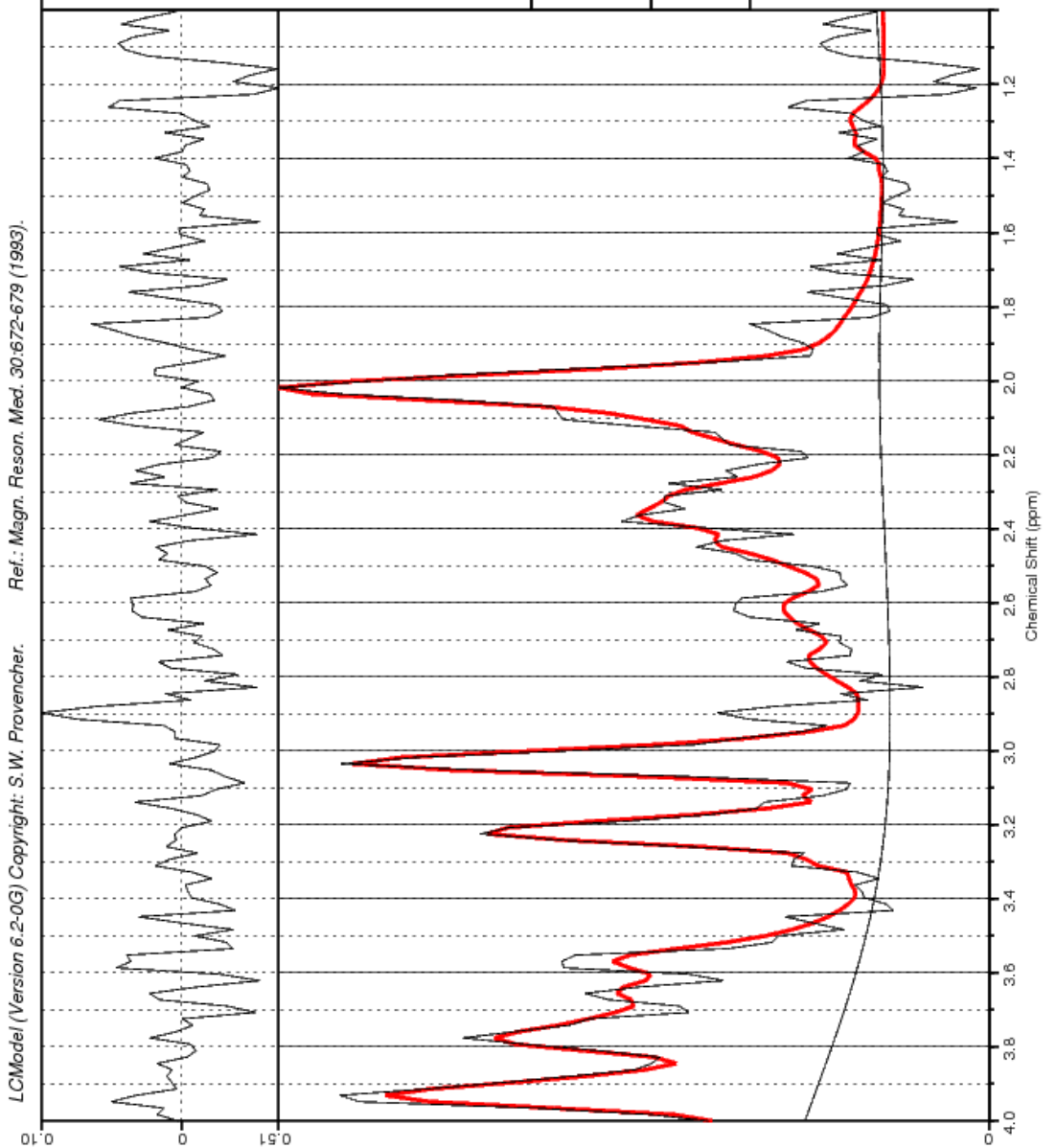
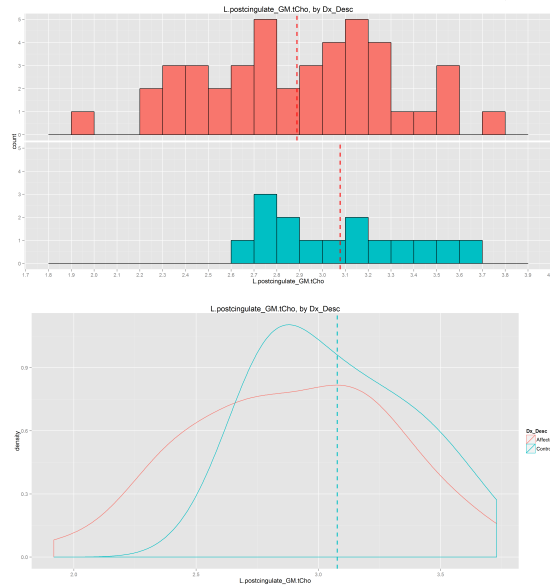


Figure 4-4: An example of the LCMODEL fitted PEPSI spectrum at the basal ganglia region.



**Figure 4-5: Histogram (Top) and density (Bottom) plots of the total choline concentration distribution between ADHD and healthy controls in the left posterior cingulate cortex.**

## Discussions

In this study, we have demonstrated the feasibility of using a fast echo planar based spectroscopic imaging sequence to evaluate the neurometabolite pattern in the AC, BG, and the SUPV brain regions in ADHD and healthy controls. The total acquisition time for both the water reference and the metabolite PEPSI acquisitions was under 10 minutes at each slab location. The primary finding of this study is the total choline concentration significantly lower in ADHD subjects at the left posterior cingulate cortex (highlighted in red in Table 4-2). In addition, we have found that the interaction between age and diagnosis also has a significant effect on the total choline concentrations. The total choline signal detected by *in vivo*  $^1\text{H}$ -MRS is mainly composed of glycerophosphocholine, phosphocholine, and also the free choline. Choline is generally known as a precursor to the principal neurotransmitter acetylcholine (ACh). In the central nervous system, ACh and its associated neurons form the cholinergic neurotransmission system, which has been shown to play an important role in sustaining attention (Himmelheber et

al. 2000). Choline containing compounds are also involved in the processes of cell membrane synthesis and degradation. In cancer, Alzheimer's disease and multiple sclerosis, increased total choline signal has been observed (Gillies and Morse 2005; Firbank et al. 2002; Narayana 2005). In contrast, decreased total choline signal has been detected in rats with cerebral ischemic stroke (Malisza et al. 1998). A decreased level of choline can potentially be an indication of cell loss or cortical thinning. Global cortical thinning has been shown to be a robust anatomical marker for ADHD (Narr et al. 2009; Shaw et al. 2006).

## Conclusions

In summary, in our efforts to investigate the pathobiochemical processes of ADHD using a fast short TE multi voxel PEPSI acquisition, we have found possible evidence of metabolite level differences between ADHD subjects and healthy controls in left posterior cingulate cortex total Choline. This finding could possibly support prior publications that there is a widespread cortical thickness decrease in ADHD children. However, we also consider the possibility that the pattern of metabolite differences might change with a larger and more balanced sampling size and more complex analysis should also be carried out based on the different subtypes of ADHD symptoms, age, gender and clinical environment.

## References

- Benjamini, Y., & Hochberg, Y. (1995). Controlling the False Discovery Rate: A Practical and Powerful Approach to Multiple Testing. *Journal of the Royal Statistical Society. Series B (Methodological)*, 57, 289-300.
- Biederman, J., & Faraone, S. V. (2005). Attention-deficit hyperactivity disorder. *Lancet*, 366, 237-48.
- Biederman, J., Mick, E., Wozniak, J., Monuteaux, M. C., Galdo, M., & Faraone, S. V. (2003). Can a subtype of conduct disorder linked to bipolar disorder be identified? Integration of findings from the Massachusetts General Hospital Pediatric Psychopharmacology Research Program. *Biol Psychiatry*, 53, 952-60.

- Biederman, J., Petty, C. R., Byrne, D., Wong, P., Wozniak, J., & Faraone, S. V. (2009). Risk for switch from unipolar to bipolar disorder in youth with ADHD: a long term prospective controlled study. *J Affect Disord*, *119*, 16-21.
- Carrey, N. J., MacMaster, F. P., Gaudet, L., & Schmidt, M. H. (2007). Striatal creatine and glutamate/glutamine in attention-deficit/hyperactivity disorder. *J Child Adolesc Psychopharmacol*, *17*, 11-7.
- Dale, A. M., Fischl, B., & Sereno, M. I. (1999). Cortical surface-based analysis. I. Segmentation and surface reconstruction. *Neuroimage*, *9*, 179-94.
- Faraone, S. V., Perlis, R. H., Doyle, A. E., Smoller, J. W., Goralnick, J. J., Holmgren, M. A., & Sklar, P. (2005). Molecular genetics of attention-deficit/hyperactivity disorder. *Biol Psychiatry*, *57*, 1313-23.
- Faraone, S. V., Wilens, T. E., Petty, C., Antshel, K., Spencer, T., & Biederman, J. (2007). Substance use among ADHD adults: implications of late onset and subthreshold diagnoses. *Am J Addict*, *16 Suppl 1*, 24-32; quiz 33-4.
- Fayyad, J., De Graaf, R., Kessler, R., Alonso, J., Angermeyer, M., Demyttenaere, K., De Girolamo, G., Haro, J. M., Karam, E. G., Lara, C., Lepine, J. P., Ormel, J., Posada-Villa, J., Zaslavsky, A. M., & Jin, R. (2007). Cross-national prevalence and correlates of adult attention-deficit hyperactivity disorder. *Br J Psychiatry*, *190*, 402-9.
- Firbank Mj Fau - Harrison, R. M., Harrison Rm Fau - O'Brien, J. T., & O'Brien, J. T. (2002). A comprehensive review of proton magnetic resonance spectroscopy studies in dementia and Parkinson's disease. *Dement Geriatr Cogn Disord*, *14*, 64-76.
- Fischl, B., Salat, D. H., Busa, E., Albert, M., Dieterich, M., Haselgrove, C., van der Kouwe, A., Killiany, R., Kennedy, D., Klaveness, S., Montillo, A., Makris, N., Rosen, B., & Dale, A. M. (2002). Whole brain segmentation: automated labeling of neuroanatomical structures in the human brain. *Neuron*, *33*, 341-55.
- Gillies, R. J., & Morse, D. L. (2005). In vivo magnetic resonance spectroscopy in cancer. *Annual Review of Biomedical Engineering*, *7*, 287-326.
- Hesslinger, B., Thiel, T., Tebartz van Elst, L., Hennig, J., & Ebert, D. (2001). Attention-deficit disorder in adults with or without hyperactivity: where is the difference? A study in humans using short echo 1H-magnetic resonance spectroscopy. *Neurosci Lett*, *304*, 117-9.
- Himmelheber, A. M., Sarter, M., & Bruno, J. P. (2000). Increases in cortical acetylcholine release during sustained attention performance in rats. *Cognitive Brain Research*, *9*, 313-25.
- Kessler, R. C., Adler, L., Barkley, R., Biederman, J., Conners, C. K., Demler, O., Faraone, S. V.,

- Greenhill, L. L., Howes, M. J., Secnik, K., Spencer, T., Ustun, T. B., Walters, E. E., & Zaslavsky, A. M. (2006). The prevalence and correlates of adult ADHD in the United States: results from the National Comorbidity Survey Replication. *Am J Psychiatry*, *163*, 716-23.
- Linnet, K. M., Dalsgaard, S., Obel, C., Wisborg, K., Henriksen, T. B., Rodriguez, A., Kotimaa, A., Moilanen, I., Thomsen, P. H., Olsen, J., & Jarvelin, M. R. (2003). Maternal lifestyle factors in pregnancy risk of attention deficit hyperactivity disorder and associated behaviors: review of the current evidence. *Am J Psychiatry*, *160*, 1028-40.
- Masi, G., Perugi, G., Millepiedi, S., Mucci, M., Toni, C., Bertini, N., Pfanner, C., Berloffia, S., & Pari, C. (2006). Developmental differences according to age at onset in juvenile bipolar disorder. *J Child Adolesc Psychopharmacol*, *16*, 679-85.
- Masi, G., Perugi, G., Toni, C., Millepiedi, S., Mucci, M., Bertini, N., & Pfanner, C. (2006). Attention-deficit hyperactivity disorder -- bipolar comorbidity in children and adolescents. *Bipolar Disord*, *8*, 373-81.
- Mick, E., Biederman, J., Faraone, S. V., Sayer, J., & Kleinman, S. (2002). Case-control study of attention-deficit hyperactivity disorder and maternal smoking, alcohol use, and drug use during pregnancy. *J Am Acad Child Adolesc Psychiatry*, *41*, 378-85.
- Muglia, P., Jain, U., Macciardi, F., & Kennedy, J. L. (2000). Adult attention deficit hyperactivity disorder and the dopamine D4 receptor gene. *Am J Med Genet*, *96*, 273-7.
- Narayana, P. A. (2005). Magnetic Resonance Spectroscopy in the Monitoring of Multiple Sclerosis. *Journal of Neuroimaging*, *15*, 46S-57S.
- Narr, K. L., Woods, R. P., Lin, J., Kim, J., Phillips, O. R., Del'Homme, M., Caplan, R., Toga, A. W., McCracken, J. T., & Levitt, J. G. (2009). Widespread Cortical Thinning Is a Robust Anatomical Marker for Attention-Deficit/Hyperactivity Disorder. *J Am Acad Child Adolesc Psychiatry*, *48*, 1014-22.
- Pastor, P. N., & Reuben, C. A. (2008). Diagnosed attention deficit hyperactivity disorder and learning disability: United States, 2004-2006. *Vital Health Stat* *10*, 1-14.
- Polanczyk, G., & Rohde, L. A. (2007). Epidemiology of attention-deficit/hyperactivity disorder across the lifespan. *Curr Opin Psychiatry*, *20*, 386-92.
- Posse, S., Tedeschi, G., Risinger, R., Ogg, R., & Le Bihan, D. (1995). High speed 1H spectroscopic imaging in human brain by echo planar spatial-spectral encoding. *Magn Reson Med*, *33*, 34-40.
- Provencher, S. W. (1993). Estimation of metabolite concentrations from localized in vivo proton NMR spectra. *Magn Reson Med*, *30*, 672-9.
- Reiersen, A. M., & Todd, R. D. (2008). Co-occurrence of ADHD and autism spectrum disorders:

- phenomenology and treatment. *Expert Rev Neurother*, 8, 657-69.
- Sharp, S. I., McQuillin, A., & Gurling, H. M. (2009). Genetics of attention-deficit hyperactivity disorder (ADHD). *Neuropharmacology*, 57, 590-600.
- Shaw P, L. J. G. D., & et al. (2006). Longitudinal mapping of cortical thickness and clinical outcome in children and adolescents with attention-deficit/hyperactivity disorder. *Arch Gen Psychiatry*, 63, 540-49.
- Simon, V., Czobor, P., Balint, S., Meszaros, A., & Bitter, I. (2009). Prevalence and correlates of adult attention-deficit hyperactivity disorder: meta-analysis. *Br J Psychiatry*, 194, 204-11.
- Spencer, T. J., Biederman, J., Madras, B. K., Faraone, S. V., Dougherty, D. D., Bonab, A. A., & Fischman, A. J. (2005). In vivo neuroreceptor imaging in attention-deficit/hyperactivity disorder: a focus on the dopamine transporter. *Biol Psychiatry*, 57, 1293-300.
- Workgroup, D.-I.-T. (2000). *The Diagnostic and Statistical Manual of Mental Disorders, Text Revision*. (4th ed.). Washington, DC: American Psychiatric Association.
- Yang, P., Wu, M. T., Dung, S. S., & Ko, C. W. (2010). Short-TE proton magnetic resonance spectroscopy investigation in adolescents with attention-deficit hyperactivity disorder. *Psychiatry Res*, 181, 199-203.
- Zhang, Y., Brady, M., & Smith, S. (2001). Segmentation of brain MR images through a hidden Markov random field model and the expectation-maximization algorithm. *IEEE Trans Med Imaging*, 20, 45-57.

## Chapter 5 Human Brain $^1\text{H}$ MR Spectral Simulation

### Introduction

According to the theories of quantum mechanics, molecule wavefunction ( $\psi$ ) contains all necessary information needed to describe the energy and the position of a molecule's spin system. An operator is used to extract the observable or measurable physical properties from the wavefunction. For example, when the position operator acts on a wavefunction, the output from the operator is the respective position of that particular state. Mathematically, an operator is simply a mathematical operation that turns a function into another function. The operator of principal importance is the Hamiltonian, which describes all observable energy levels of a system, commonly denoted by the symbol  $H$ .

In general, the wavefunction of a system is time dependent and how the wavefunction evolves with time according to the Hamiltonian is described by the time-dependent Schrödinger's equation (TDSE)

$$\frac{d\psi(t)}{dt} = -i\hat{H}\psi(t). \quad [5-1]$$

The solution to the TDSE enables us to find the expectation values of the Hamiltonian operator, which can be expressed explicitly in different forms to incorporate the conditions of free evolution, RF pulses, gradient pulses, J-coupling, chemical shift and so on.

What we are trying to observe in a single NMR experiment is the transverse magnetization, which is composed of signals not from one or two spins but from the ensemble of spins in the experimental sample. In the case of pure state, the TDSE in Eq. 5-1 is sufficient to track the entire spin evolution. Each spin in fact has a different wavefunction from the others. The wavefunction of a single spin is in general a linear combination of the eigenfunctions of the



Hamiltonian operator, which is also known as the mixed state or the superposition states. As a result, we require a modified framework that would allow us to keep track of the mixed states.

To overcome this tedious task, the density operator or density matrix is introduced to compute the ensemble average or the expectation values of the bulk magnetization. The density operator for an uncoupled spin system is defined as

$$\hat{\rho} = \begin{pmatrix} \overline{c_\alpha c_\alpha^*} & \overline{c_\alpha c_\beta^*} \\ \overline{c_\beta c_\alpha^*} & \overline{c_\beta c_\beta^*} \end{pmatrix}, \quad [5-2]$$

where  $c_\alpha$  and  $c_\beta$  are the coefficients of the superposition states, and  $c_\alpha^*$  and  $c_\beta^*$  are the complex conjugate of  $c_\alpha$  and  $c_\beta$ . The concept of ensemble averaging allows us to calculate the bulk magnetization using the elements of the density matrix, which represents the statistical distribution of the superposition states for a large quantity of spins. It is important to point out that the density operator is also a time dependent quantity because the coefficients of the superposition states are time variant functions.

In the case of the density matrix, the TDSE no longer satisfies the complexity of the ensemble problem. A new equation of motion derived from classical mechanics has been introduced to account for the density operator and this equation is known as the Liouville-von Neumann equation (LVNE):

$$\frac{d\hat{\rho}(t)}{dt} = -i(\hat{H}\hat{\rho}(t) - \hat{\rho}(t)\hat{H}). \quad [5-3]$$

The solution to the LVNE is

$$\hat{\rho}(t) = e^{-i\hat{H}t} \hat{\rho}(0) e^{i\hat{H}t}, \quad [5-4]$$

where  $\hat{H}$  is the Hamiltonian operator for energy and assumed to be time-independent,  $\hat{\rho}(t)$  is the density operator at time t, and  $\hat{\rho}(0)$  is the density operator at time zero. The term  $e^{-i\hat{H}t}$  can

actually be expressed in matrix form as well; hence the solution to the LVNE is simply the multiplication of three matrices.

As the number of spins in molecules increase, the size of the Hamiltonian matrix increases as well. To also account for complex J-coupling effects, the matrix size will eventually become too large to handle using just pencil and paper. As a result, numeric integration of the LVNE provides more advantageous platform to propagate the density operator through time. In addition, the expectation value of a particular observable  $\hat{A}$  can be obtained by a simple trace matrix operation:

$$\langle \hat{A} \rangle = Tr\{\hat{A}\hat{\rho}(t)\}. \quad [5-5]$$

Equation 5-3 and 5-4 form the basic operations to the numerical simulations of the NMR time domain signals. Many programs have been created to provide simulation solutions to NMR experiments since the early 1970's. One of the most popular simulation software package was introduced in 1993 by Smith et al and was named GAMMA (general approach to magnetic resonance mathematical analysis) (Smith et al. 1993). GAMMA was developed in the object oriented C++ programming language and contains a library of tools for creating and simulating NMR experiments. GAMMA has provided scientists in the NMR community a simulation platform that is flexible, reliable, and open source.

In 2007, Brian Soher et al. have introduced an application package that provides graphical user interface (GUI) for the GAMMA simulation library, which is called GAVA (GAMMA visual analysis) (Soher et al. 2007). Building on top of what they have already accomplished with GAVA, Soher et al. further introduced a comprehensive MRS software package that encapsulates four widely used MRS software packages into one easy to use, open source, GUI based platform named VeSPA (Versatile simulation, Pulses and Analysis for

Magnetic Resonance Spectroscopy). The four MRS software packages are the GAMMA/PyGAMMA simulation library, MatPulse for RF pulse design originally written by Dr. Gerald Matson (Matson et al. 1994), IDL\_Vespa, and Prioset. The latter two applications are both created by Brain Soher for the purpose of spectral analysis and spectral simulation in an open sourced format. Unlike MatPulse and IDL\_Vespa, VeSPA is developed in the open source Python language, so it is free and does not require substantial amount of software license fee to maintain and operate the programs.

The primary goal of this chapter is to apply the GUI based MRS simulation and visualization software VeSPA to simulate *in vivo*  $^1\text{H}$  NMR spectra. The motivation for using VeSPA is that it is a simple, flexible, and user-friendly graphical simulation environment that has access to almost the entire GAMMA C++ library. The second objective of this chapter is to investigate how the CRLB values output by LCModel vary with different acquisition parameters (field strength and TE values) and also how baseline and lineshape affect the quantification accuracy.

## Methods and Materials

### Pulse Sequence Simulations

All  $^1\text{H}$  MRS simulations were performed using the VeSPA simulation software and a screenshot of the program is shown in Figure 5-1. The software package was installed on a Windows XP system parallel installed on a 1.8 GHz Intel Core i5 and 4 GB RAM Macintosh OS X10.8 laptop. Using the library of predefined chemical compounds with chemical shift and J-coupling values published by Govindaraju et al. (Govindaraju et al, 2000), simulations were performed on commonly observable neurometabolites: NAA, NAAG, GABA, choline, creatine, glucose-alpha, glucose-beta, Glu, Gln, glycerophosphorylcholine, myo-inositol, scyllo-inositol,

lactate, phosphocreatine, and taurine. Using the predefined pulse sequences in VeSPA, PRESS and Spin Echo acquisition were simulated. The parameters of these pulse sequences are user definable. VeSPA is capable of density matrix simulations that make use of both the ideal RF pulses (defined in GAMMA) and the user-defined real RF pulses. Ideal RF pulses were used in the implementation of the VeSPA predefined PRESS and Spin Echo sequences in this study. Total three magnetic field strength levels were chosen for simulations, including 1.5 T, 3 T, and 7 T, since these are the magnetic field strengths commonly available on commercial scanners. Various echo time (TE) values were selected for simulations at those three field strengths using PRESS and Spin Echo acquisitions. Table 5-1 lists the TE and resonance frequency values simulated with VeSPA Simulation software package.

### **Spectra Simulation and Quantification**

All simulated *in vivo*  $^1\text{H}$  spectra were created using the VeSPA Priorset software package. This application uses prior information from the VeSPA Simulation experiments to create simulated single voxel MR spectroscopy data. Figure 5-2 shows the VeSPA Priorset user interface as well as example brain spectra with added random noise and baseline signals. The random Gaussian noise were generated using the `numpy.random.randn()` function in Python. In Priorset, the SNR value is defined by the peak height divided by root mean square of noise value and the peak height is obtained from the user defined reference peak, which was chosen to be the 3.0-ppm creatine peak. Total 12 SNR levels were simulated using the experiments listed in Table 5-1. Zero phase values were set for all metabolites and the B0 shift was also chosen to be zero. In addition, the spectral linewidth value was adjusted by changing the  $T_2^*$  line-broadening parameter in Priorset and the  $T_2$  values for all simulated metabolites were assigned to be 0.3 seconds. Ten different line-broadening effects were simulated using the PRESS TE 30

acquisition at 3 T. Using the predefined baseline signals provided by Priorset, total of seven baseline signals at 0.9 ppm, 1.35 ppm, 1.64 ppm, 2.14 ppm, 2.35 ppm, 2.89 ppm, and 3.81 ppm, were added to the simulated brain spectra. All simulated spectra were fitted with the LCModel software, using vendor provided basis-set files. The CRLB values for all experiments were recorded and plotted against the SNR values and linewidth values.

## Results

### SNR vs. SD

The primary interest of this study is to investigate the relationship between the CRLB values obtained from LCModel and the SNR in the simulated MR spectra for Glu, Gln, and GABA. Figure 5-3 displays some of the simulated spectra generated by Priorset with SNR values of 26, 20, 12, 9, and 8, using the PRESS TE 30 experiment at 3 T. The linewidth of these experiments were chosen to be 0.04 ppm, which is close to the average linewidth value obtained in the anterior cingulate cortex in a human brain. Figure 5-4 shows an example of the LCModel fitted spectrum, which was produced by Priorset using the PRESS TE 80 experiment at 3 T. LCModel was able to reliably identify majority of the metabolites in the simulated spectrum, except for Gln, GABA, and glucose. The concentration values listed in this output file correspond to the metabolite signal amplitude in institutional unit (I.U.). No baseline signals were added in this part of the study. Figure 5-5 shows the SNR verses CRLB plots for Glu, Gln, and GABA for two of the experiments. The top is the PRESS TE 30 experiment at 1.5 T and the bottom is the PRESS TE 20 experiment at 7T. Figure 5-6 also shows the SNR verses CRLB plots for Glu, Gln, and GABA for three of the experiments. The top is the PRESS TE 30 experiment at 3 T, the PRESS TE 80 experiment at 3T is located in the middle of the figure, and the bottom is the Spin Echo TE 15 experiment at 3T. In similar arrangements, Figure 5-7 and Figure 5-8

display the SNR verses CRLB plots for total NAA, total creatine, and total choline. Some of the data curves were fitted with a polynomial function with very high  $R^2$  values. The general observation from these plots is that the CRLB values increase with decreasing SNR values in the simulated spectra for all six metabolites. The CRLB values are generally very low for total NAA, total creatine, and total choline. However, the CRLB values for Glu, Gln, and GABA are highly depended on the SNR values.

### Linewidth vs. SD

Using the PRESS TE 30 experiment at 3T, the aim of this part of the study is to investigate the relationship between metabolite signal linewidth and the CRLB value. Figure 5-9 displays some of the simulated spectra generated by Priorset with linewidth values ranged from 0.028 ppm to 0.087 ppm, using the PRESS TE 30 experiment at 3 T. The SNR values of these experiments were chosen to be 11. Figure 5-10 shows the linewidth verses CRLB plots for six neurometabolites. The CRLB values of total NAA, total creatine, and total choline remained to be relatively stable (under 5%) as the linewidth increases. For Gln, there were considerable amount of data points with CRLB values of 999% and these data points were not plotted in the figure, but even with the remaining four data points, none of them has CRLB values below 20%. For Glu, no discernable trend can be made as regard to the relationship between the linewidth and the CRLB. However, the CRLB of Glu stays below 15% as the linewidth increases, so possible conclusion can be made is that the CRLB of Glu are less likely affected by signal linewidth with PRESS TE 30 acquisition at 3T. For GABA, there is some upward trending for the CRLB values as the linewidth increases. Surprisingly, the plot shows that GABA can potentially be quantified with CRLB lower than 20% when the linewidth of the spectrum is lower than 0.04 ppm, but this assumption needs further validation.

## Baseline vs. SD

In this part of the study, the relationship between baseline and CRLB was examined. Seven baseline signals were added one by one in the order of their increasing ppm values. Figure 5-11 displays the PRESS TE 30 simulated spectrum at 3T with and without added baseline signals and Gaussian noise. The SNR and linewidth for the spectrum was 14 and 0.036 ppm. Figure 5-12 shows the CRLB values of Glu, GABA, tNAA, tCho, and tCr when the baseline signal was added at the corresponding ppm value. Again, for Gln, none of the data points has CRLB values lower than 40%, so the Gln CRLB was not plotted. It can be seen that the CRLB values of tNAA, tCho, and tCr remain fairly constant when additional baseline signals were added to the spectrum. On the contrary, the CRLB values of Glu and GABA demonstrate considerable instability when baseline signals were added. For Glu, the largest perturbation in CRLB values occurs when baseline signals were added at the 2.14 ppm and the 2.35 ppm. For GABA, the largest perturbation in CRLB values occurs when baseline signals were added at 2.35 ppm and the 2.89 ppm.

## Discussions

This study aims to provide further insight into the relationship between the SNR, linewidth, baseline, and the LCModel quantification percent standard deviation or the CRLB value for Glu, Gln, and GABA. Six VeSPA simulated MR spectroscopy experiments were studied at various SNR levels. The PRESS TE 30 experiment at 3T was further investigated with 10 linewidth values and 7 baseline signals separately. By comparing the CRLB verses SNR plots for these three structurally very similar metabolites, conclusion can be drawn that, at 3 T, the Gln CRLB values are primary dependent on the SNR of the simulated spectra, yet the CRLB values of GABA are influenced by both the SNR and linewidth values. Although it might seem

impossible to quantify Glu and Gln separately at 3T, this study suggest that with SNR higher than 25, Gln can be quantified with CRLB lower than 20% with the PRESS TE 30, assuming that the *in vivo* concentration of Gln is around 3-6 mMol. TE 80 acquisition appears to be slightly more advantageous for the detection of Glu and Gln than the TE 30 acquisition, as shown in Figure 5-6 that some of the Gln CRLB values are below 20% when the SNR is higher than 15. However, generally, in MRS acquisitions, as the TE value increases, the SNR of a spectrum decrease, so the accurate detection of Glu and Gln with the TE 80 acquisition requires additional acquisition time to achieve desirable SNR levels. Furthermore, the simulations also suggest that the short TE Spin Echo acquisition is reliable in detecting Glu at 3 T. Surprisingly, the simulations also suggest that TE 15 Spin Echo acquisition can detect GABA signals with SNR values higher than 10. In addition, the PRESS TE 20 simulations indicate that this acquisition method is reliable in detection of both Glu and Gln, but not as reliable for GABA. Hence, the accurate and reliable detection of GABA signals requires the usage of special spectral editing pulse sequences. This study also shows that Glu and GABA, presumably Gln as well, are sensitive to the presence of macromolecule baseline signals. The metabolite signal amplitudes for these three metabolites vary strongly with the additions of baseline signals at the 2.14 ppm, the 2.35 ppm, and the 2.89 ppm.

To validate the some of the results from this simulation study, 95 actual *in vivo* data sets were extracted from an ongoing single voxel PRESS MRS (Siemens 3T MAGNETOM Allegra system, TE=30 ms, TR=2000 ms, Voxel size=12x20x18 mm<sup>3</sup>, Vector size=2048, NEX=128) depression study (Narr and Randall, PI) to investigate how data SNR and signal linewidth affects the CRLB values, using the LCModel software. As shown in top part of figure 5-13, we plotted the CRLB values of Glu, Gln, and GABA versus data SNR. The plots confirms with simulation



results that Glu CRLB decreases as the spectral SNR increases and PRESS TE 30 is not a reliable method to detect Gln and GABA, but the CRLB values of Gln are able to drop below the 20% mark when the spectral SNR is higher than 15. The bottom three graphs of figure 5-13 show that as the linewidth of a spectrum increases, the CRLB of Glu increases as well, but the values for Gln and GABA do not appear to be increasing. This finding suggests that the measurement uncertainties of Gln and GABA are not influenced by the spectral linewidth at 3 T with PRESS TE 30 acquisition.

## Conclusions

We applied the GUI based MRS simulation and visualization software VeSPA to simulate *in vivo*  $^1\text{H}$  NMR spectra and to investigate how the LCModel quantification accuracy varies with different acquisition parameters and baseline signals. Quantum mechanical based simulations reveals that Gln cannot be reliably measured at 1.5 T and 3 T with the PRESS acquisition and the Spin Echo method, but Gln can be reliably measured at 7 T with the PRESS method. Glu can be reliably measured at 1.5 T, 3 T, and 7 T with both the PRESS and Spin Echo method. Pulse sequences other than PRESS should be employed to detect GABA resonances, since either the PRESS method or the Spin Echo method was able to accurately quantify GABA at all three field strength levels. Linewidth broadening caused by  $T_2^*$  did not have significant influence on Glu and Gln measurements, but good linewidth is necessary for GABA quantification with PRESS acquisition. Macromolecule baseline signals significantly influence the resonance amplitudes for Glu and Gln but not for tNAA, tCho, and tCr.

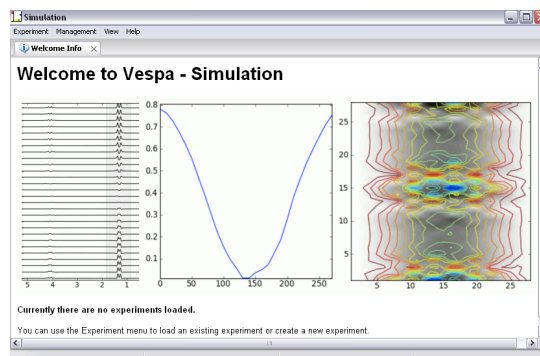


Figure 5-1: VeSPA simulation software user interface.

	PRESS (ms)	Spin Echo (ms)
1.5 T	TE 30	x
3 T	TE 30	TE 15
	TE 80	x
7 T	TE 20	x

Table 5-1: Field Strength and TE values chosen for simulations.

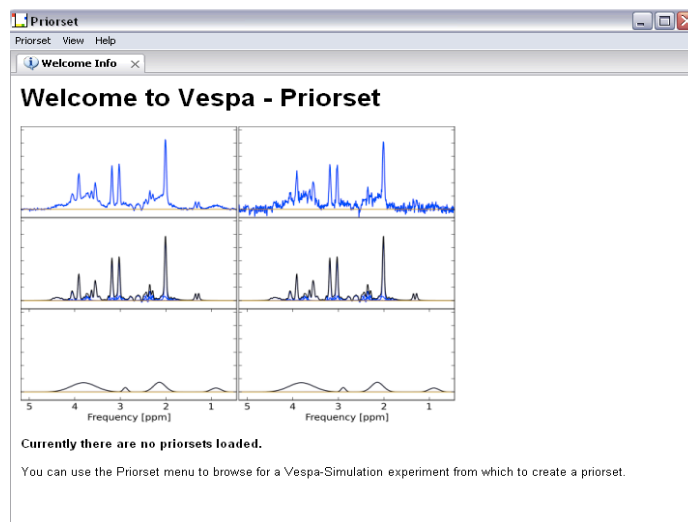


Figure 5-2: VeSPA Priorset user interface.

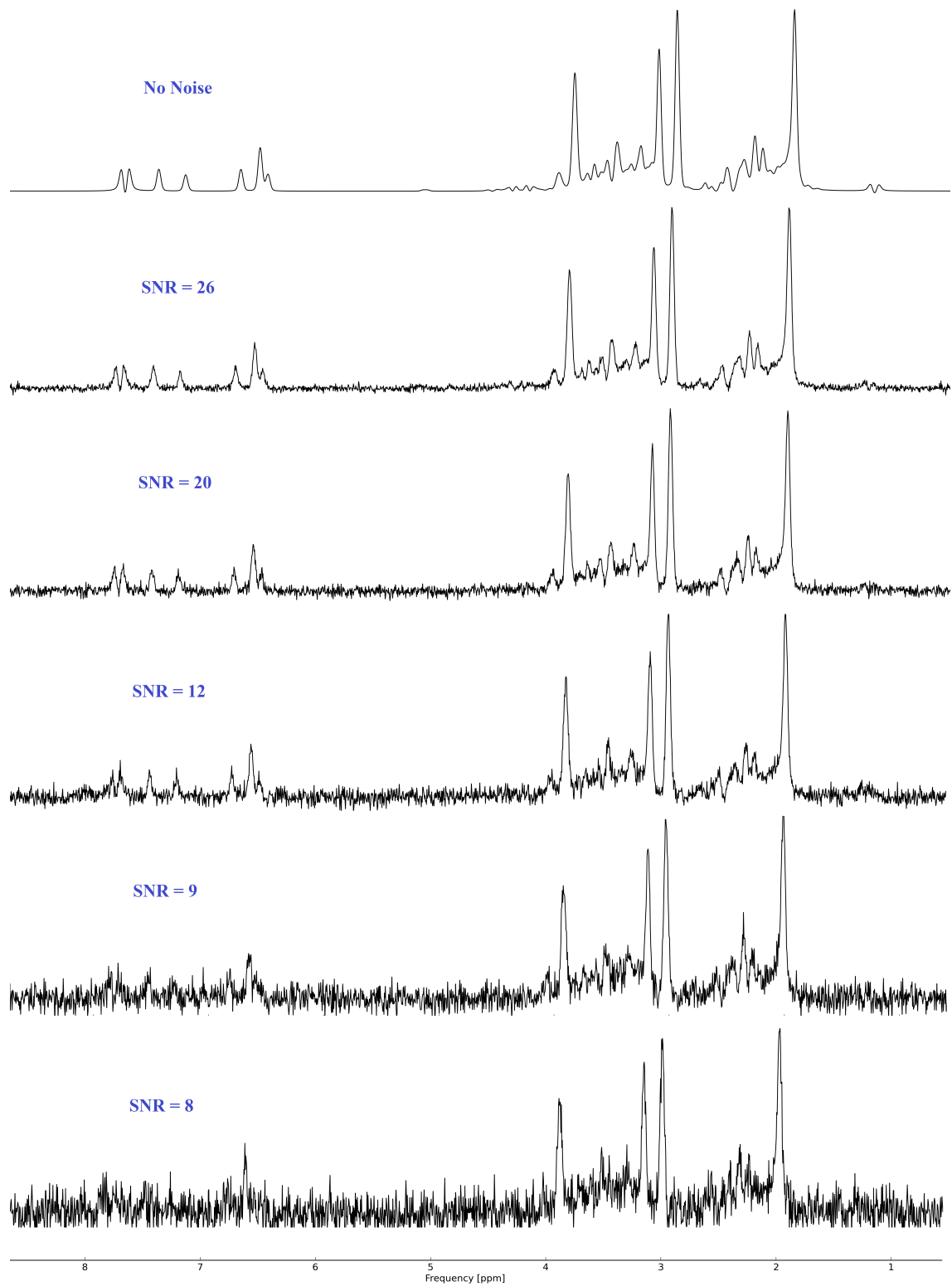


Figure 5-3: VeSPA simulated 1H MR spectrum with different levels of Gaussian noise with PRESS TE 30 at 3 T.

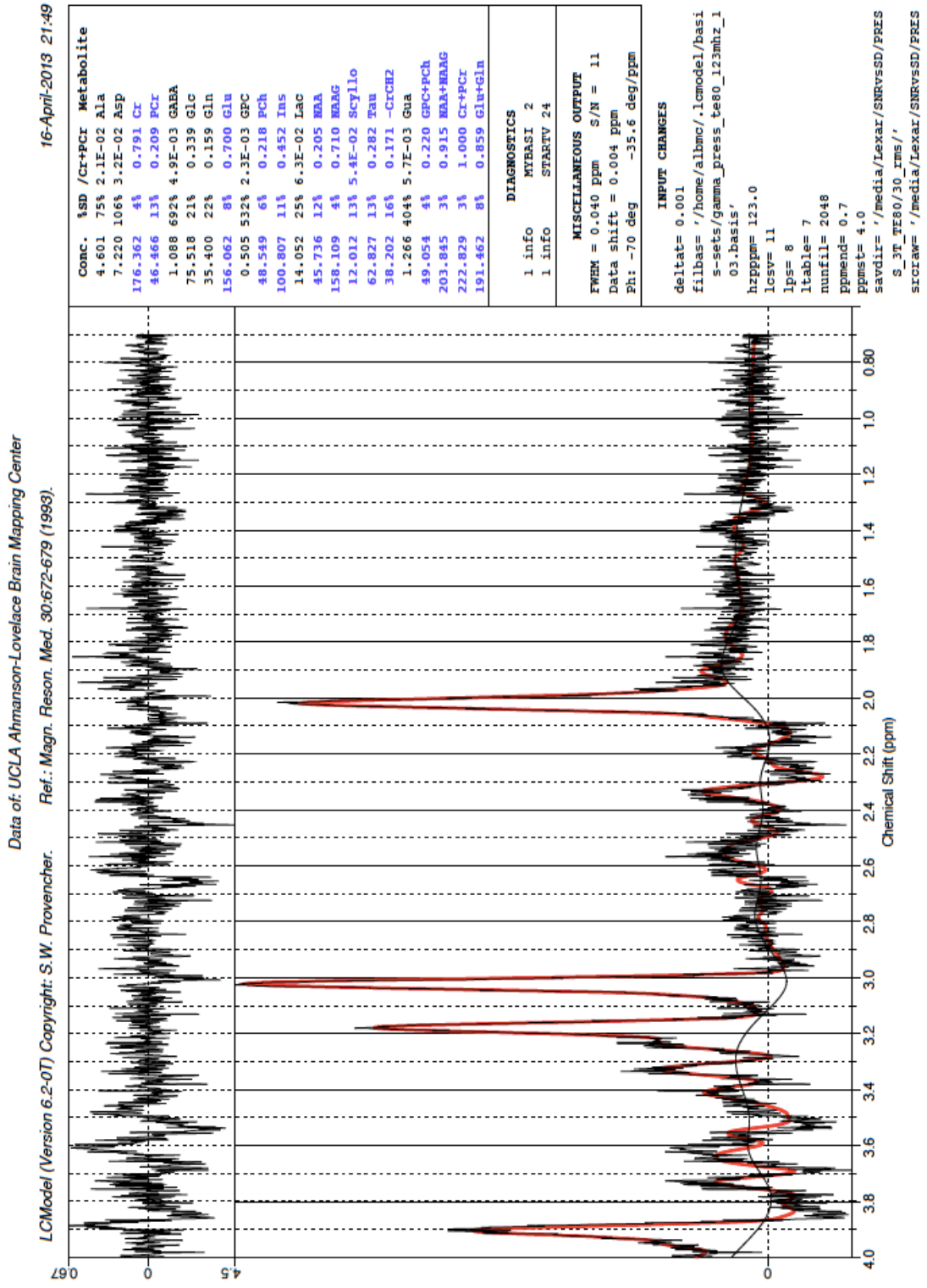
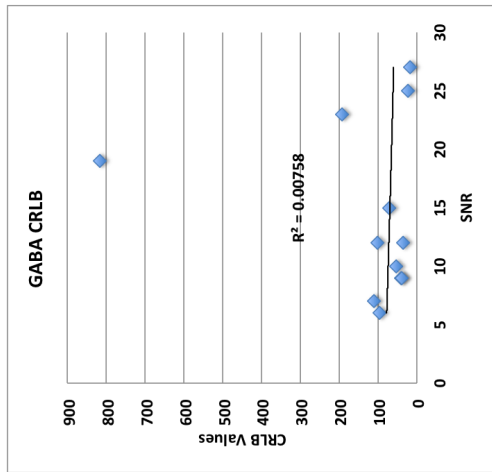
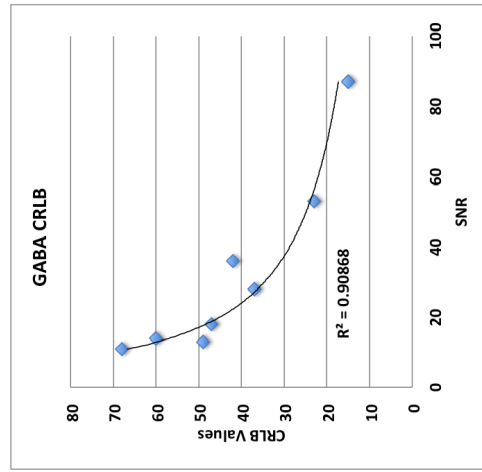


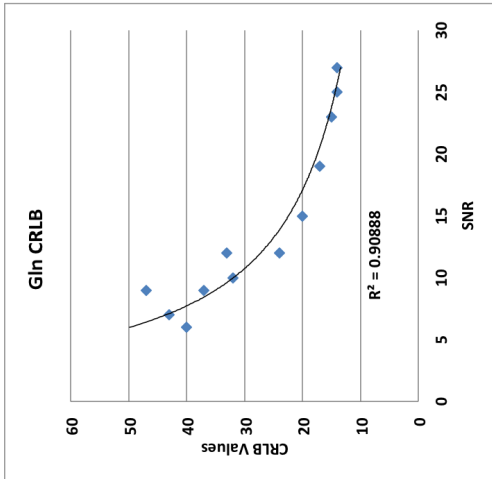
Figure 5-4: An example of LCModel analyzed VeSPA simulated MR spectrum with PRESS TE 80 at 3 T.



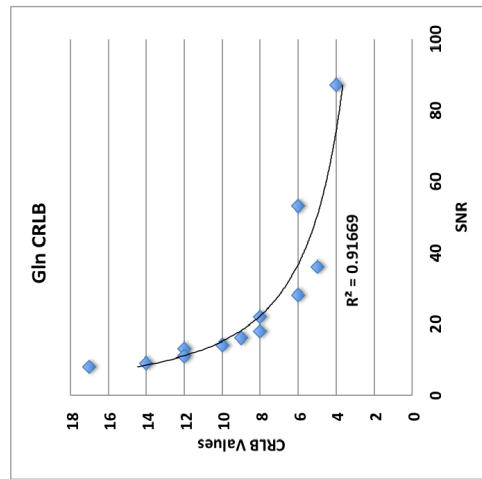
**1.5 T**



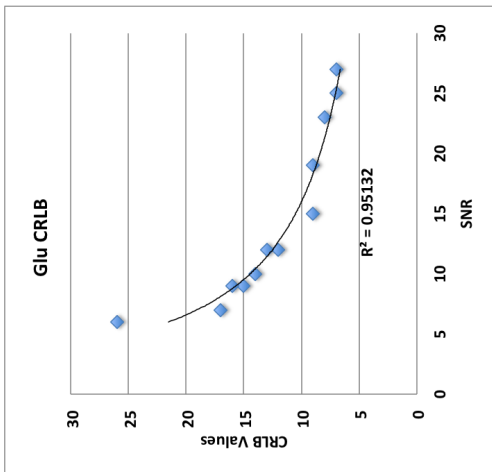
**7 T**



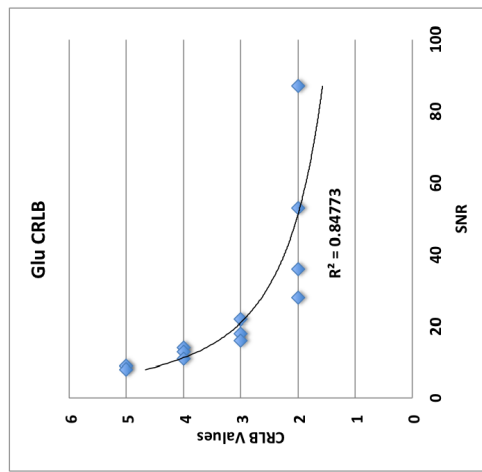
**1.5 T**



**7 T**

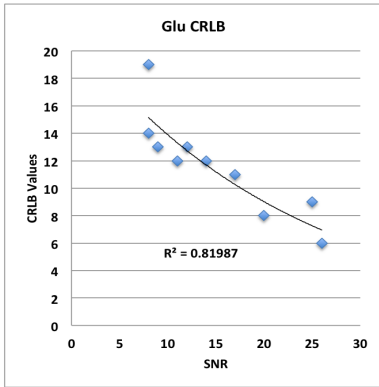


**1.5 T**

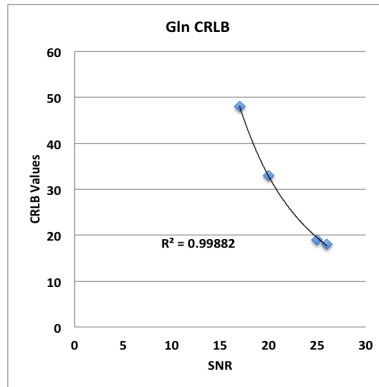


**7 T**

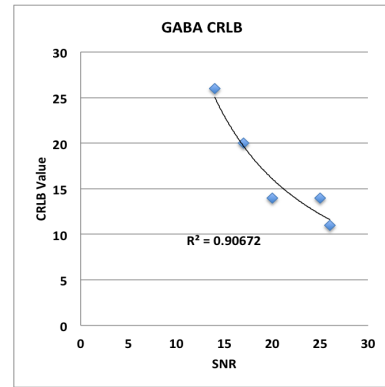
Figure 5-5: CRLB values of Glu, Gln, and GABA versus SNR (Top: PRESS TE 30 at 1.5 T, Bottom: PRESS TE 20 at 7T).



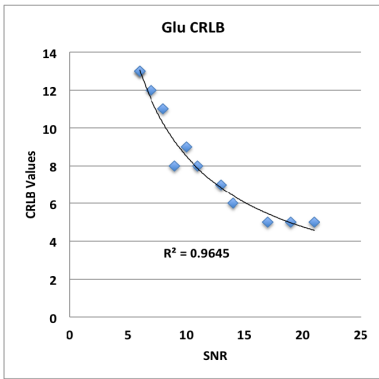
**PRESS TE 30**



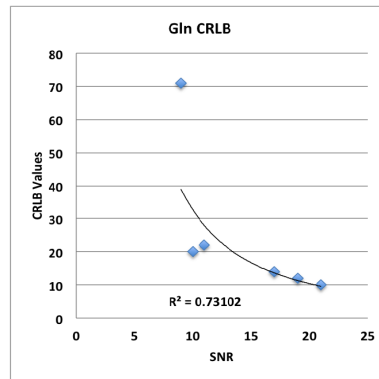
**PRESS TE 30**



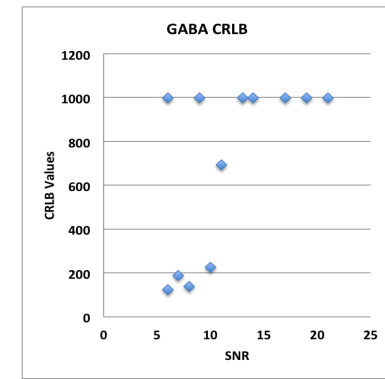
**PRESS TE 30**



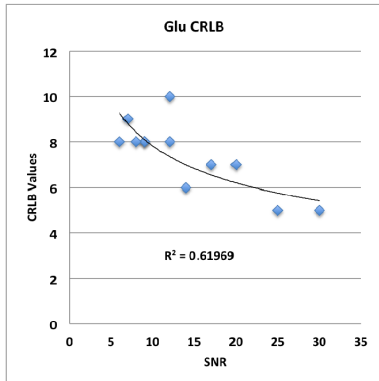
**PRESS TE 80**



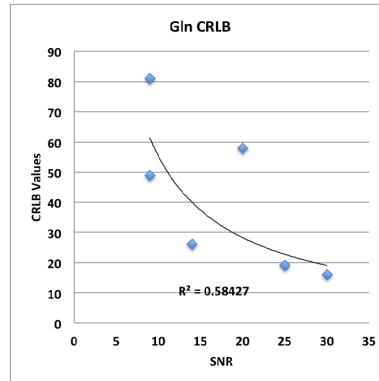
**PRESS TE 80**



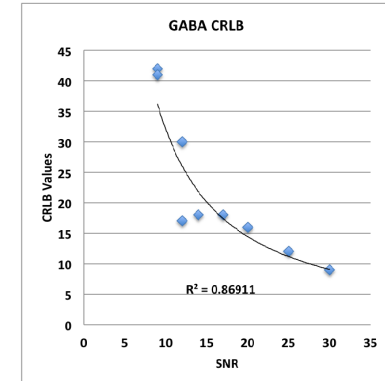
**PRESS TE 80**



**Spin Echo TE 15**



**Spin Echo TE 15**



**Spin Echo TE 15**

**Figure 5-6: CRLB values of Glu, Gln, and GABA verses SNR at 3T(Top: PRESS TE 30, Center: PRESS TE 80, Bottom: Spin Echo TE 15).**

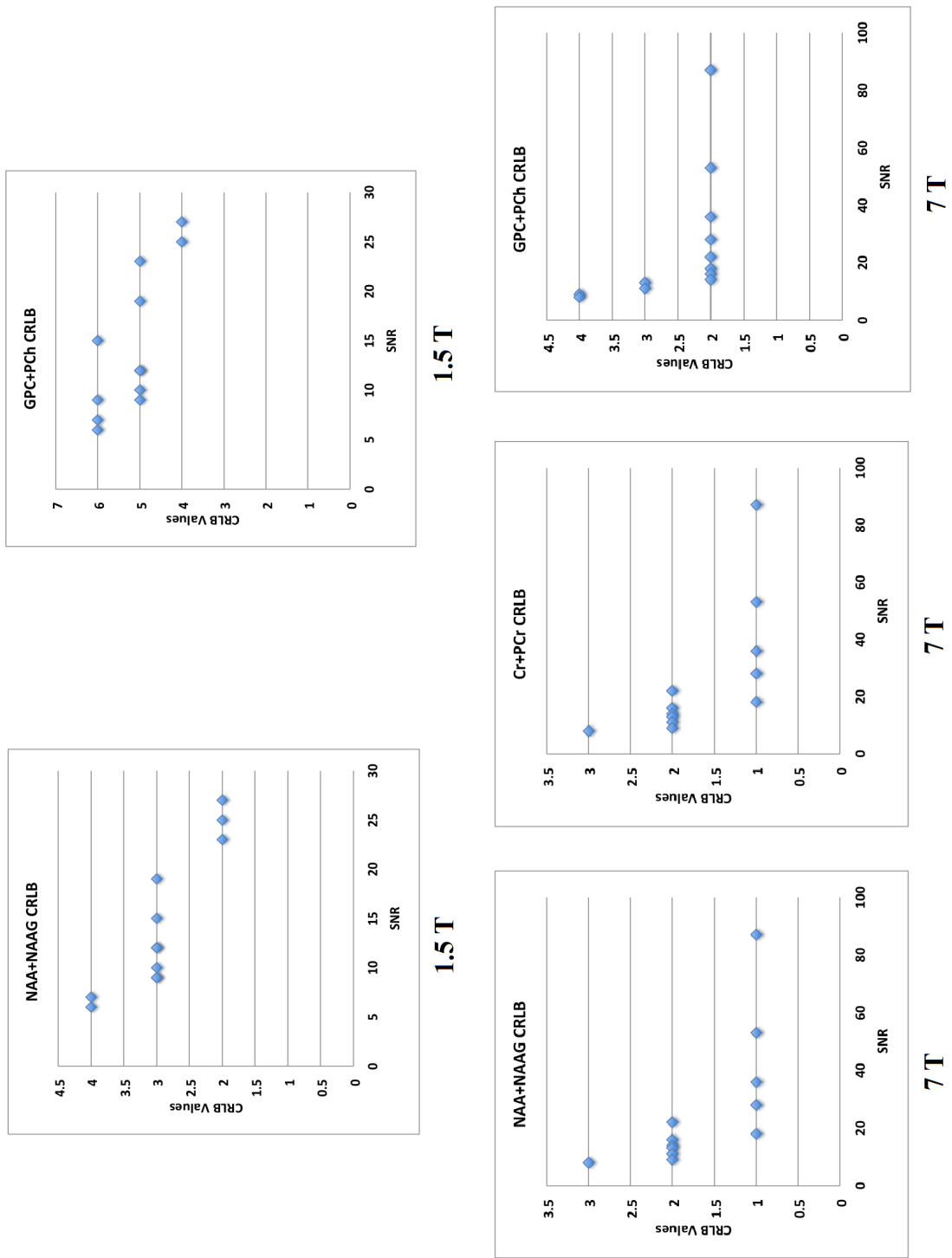


Figure 5-7: CRLB values of tNAA, tCho, and tCr verses SNR (Top: PRESS TE 30 at 1.5 T, Bottom: PRESS TE 20 at 7T).





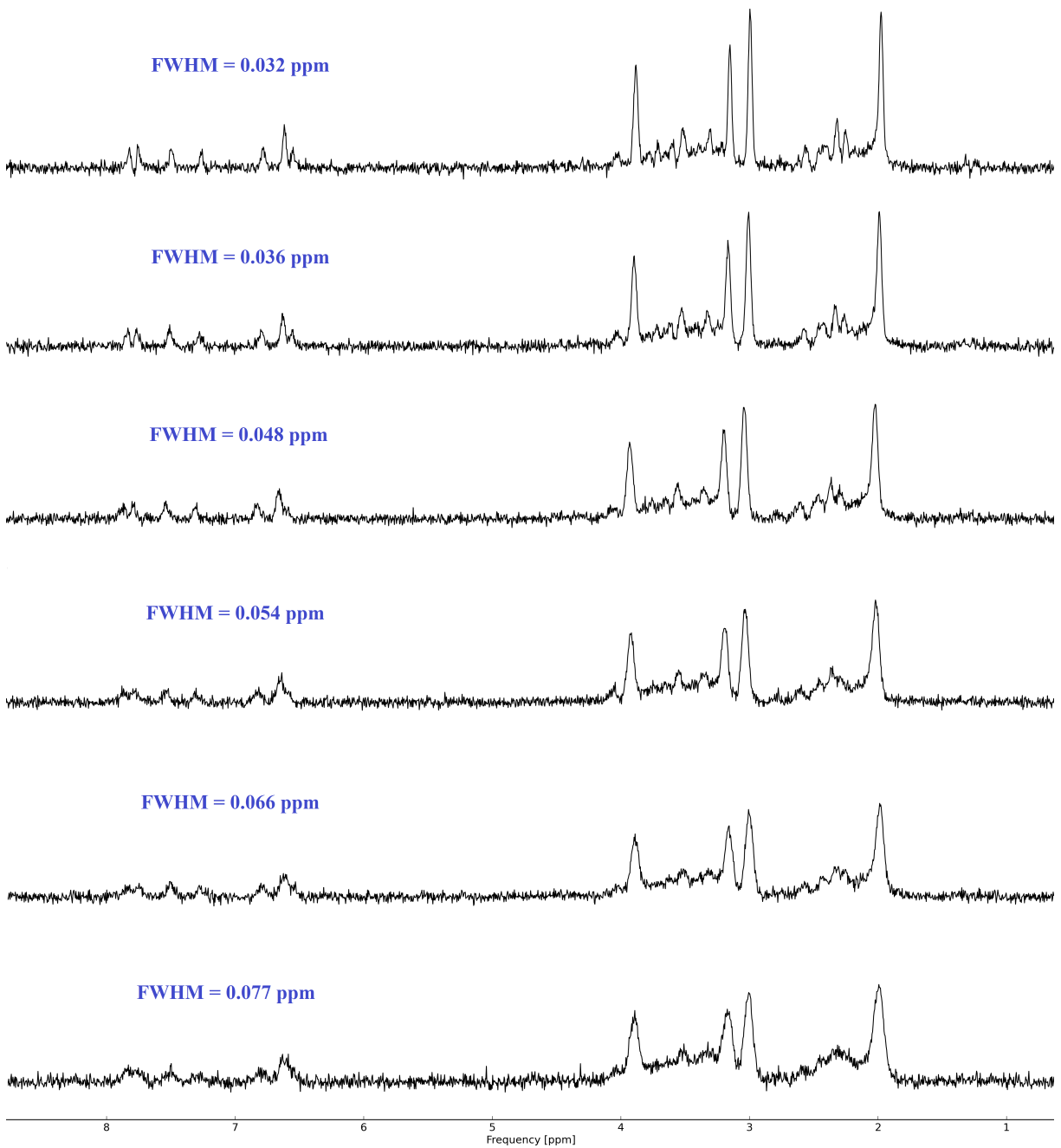


Figure 5-9: VeSPA Priorset simulated MR spectra with increasing linewidth values.

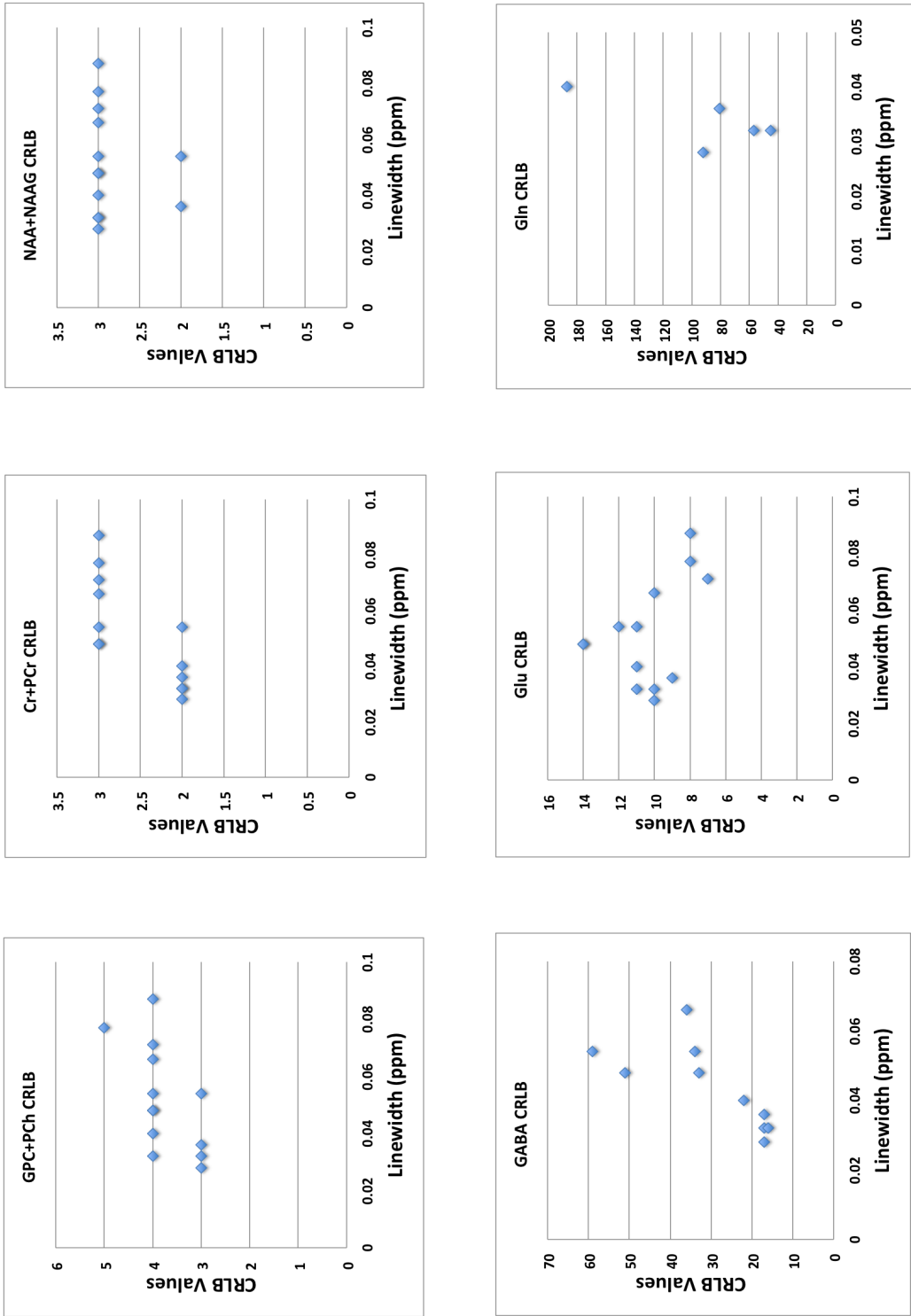


Figure 5-10: CRLB values of Glu, Gln, GABA, tNAA, tCho, and tCr verses linewidth (PRESS TE 30 at 3 T).

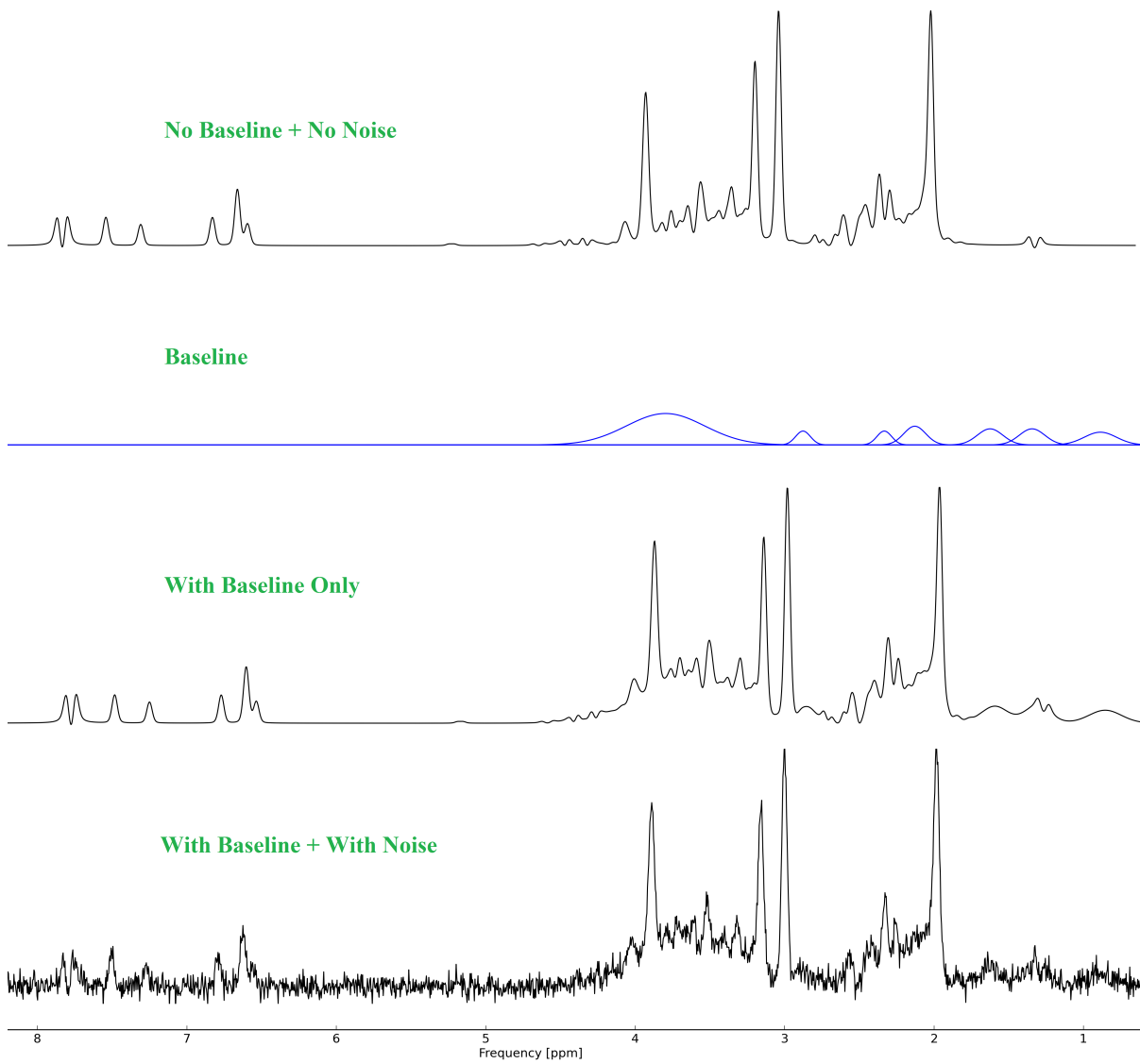


Figure 5-11: Simulated PRESS TE 30 spectra at 3T with added Gaussian noise and seven baseline signals.

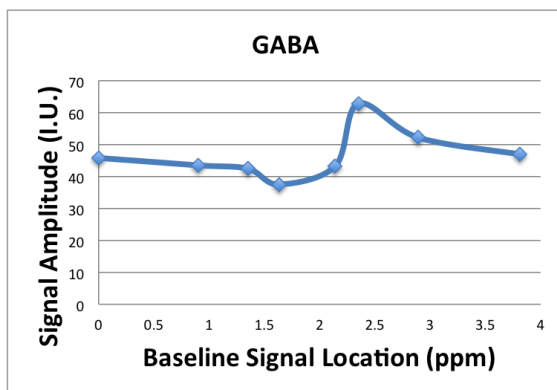
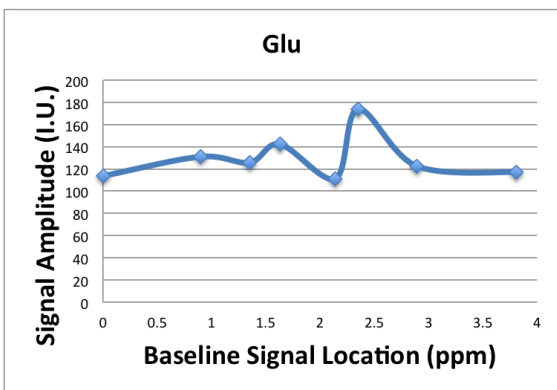
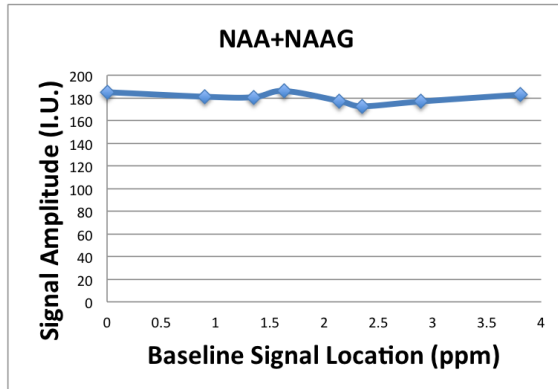
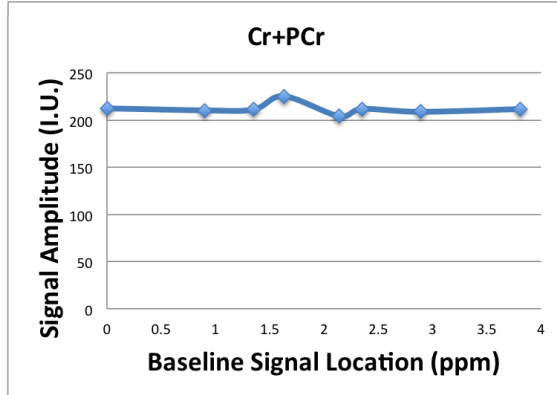
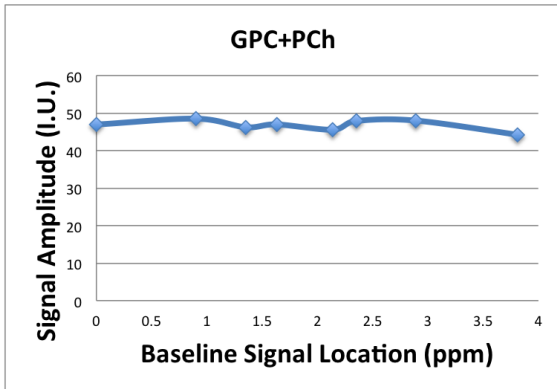


Figure 5-12: Signal amplitudes of Glu, Gln, GABA, tNAA, tCho, and tCr verses baseline signals (PRESS TE 30 at 3T).

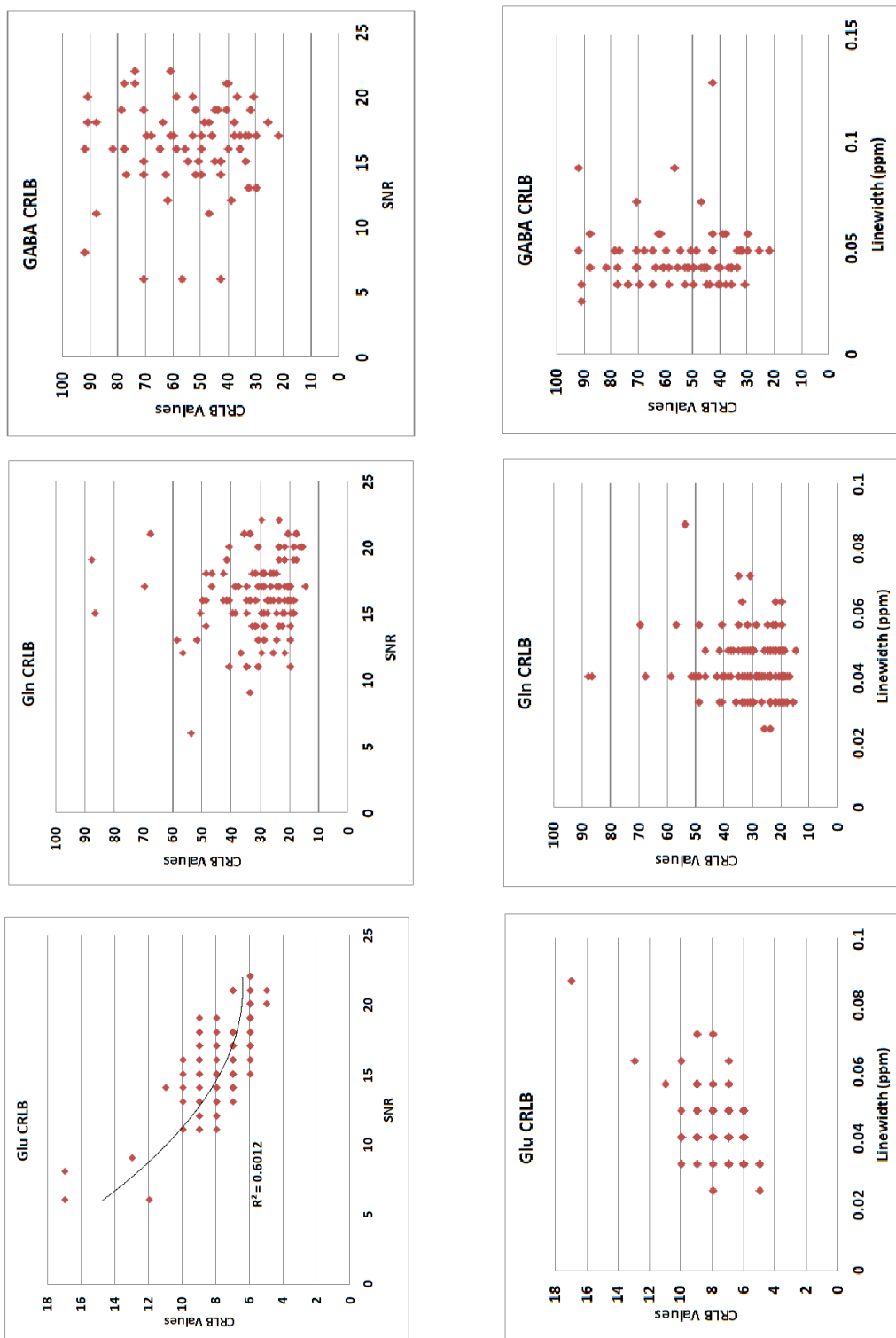


Figure 5-13: Glu, Gln, and GABA LCModel %SD (CRLB) vs. SNR (top) and linewidth (bottom) at 3T using single voxel TE 30 PRESS acquisition.

## References

- Matson, G. B. (1994). An integrated program for amplitude-modulated RF pulse generation and re-mapping with shaped gradients. *Magnetic Resonance Imaging*, *12*, 1205-25.
- Smith, S. A., Levante, T. O., Meier, B. H., & Ernst, R. R. (1994). Computer Simulations in Magnetic Resonance. An Object-Oriented Programming Approach. *Journal of Magnetic Resonance, Series A*, *106*, 75-105.
- Soher, B. J., Young, K., Bernstein, A., Aygula, Z., & Maudsley, A. A. (2007). GAVA: Spectral simulation for in vivo MRS applications. *Journal of Magnetic Resonance*, *185*, 291-99.

## Chapter 6 J-difference Editing for GABA

### Introduction

$\gamma$ -Aminobutyric acid (GABA;  $\text{NH}_2\text{-C}^4\text{H}_2\text{-C}^3\text{H}_2\text{-C}^2\text{H}_2\text{-C}^1\text{O}_2\text{H}$ ) is roughly ten times lower in concentration than some of the more detectable neurometabolites, such as N-acetylaspartate (NAA), choline (Cho), and creatine (Cr). GABAergic neurotransmission imbalance has been implicated in a number of neurological and psychiatric disorders, such as the major depressive disorder (Sanacora et al 2004; Hasler et al 2007), attention deficit hyperactivity disorder (Edden et al 2012), obsessive-compulsive disorder (Simpson et al 2012; Nikolaus et al 2012), schizophrenia (Rowland et al 2012; Kegeles et al 2012), epilepsy (Petroff et al 1996; Simister et al 2009), the autism spectrum disorder (Kubas et al 2012; Rojas et al 2013) and so on. In response to its significant roles in neurotransmission and diseases, a large number of magnetic resonance spectroscopy (MRS) methodology studies have been devoted to the accurate detection and quantification of GABA (Rothman et al. 1993; Jensen et al. 2005; Edden and Barker 2007; Henry et al 2010), since currently MRS is the only non-invasive method to detect and measure GABA concentration *in vivo*.

GABA has a total of six NMR observable protons distributed in three methylene groups. At 4 T or lower, strong coupling effect is observed for GABA C-2 and C-3 protons. The triplets of the GABA C-2 and C-4 resonances appear at 2.28 ppm and 3.01 ppm, while the C-3 quintet is situated at 1.89 ppm. All three of the resonances from GABA strongly overlap with other more intense resonances signals generated from Glutamate (Glu), Glutamine (Gln), NAA, and Cr. Figure 6-1 shows the GABA C-2, C-3, and C4 signal peak location in relation to the other more prominent brain metabolites. Because of the overlapping signals, detection of GABA is less feasible on clinical scanners (1 T to 3 T) with the traditional point resolved spectroscopy

(PRESS) or the stimulated echo (STEAM) based pulse sequences. As a result, a group of special editing techniques have to be employed to achieve separation of the obscured GABA resonance peaks from other overlapping resonances.

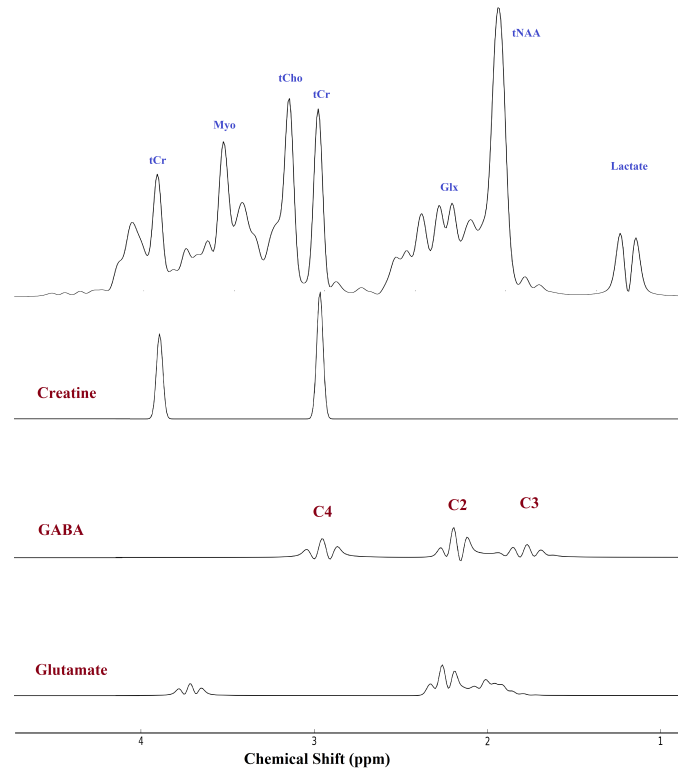


**Figure 6-1: GABA C-2, C-3 and C-4 proton resonances are overlapping with Glu, NAA, and tCr signal peaks (Simulated spectral with PRESS TE 30 ms at 3 T).**

Generally, a spectral editing method in MRS involves the simplification of the MR spectrum so that only a particular metabolite is singled out in the detection process. Many techniques have been developed in the past thirty years to achieve this goal. There are the homonuclear J-difference editing method (Rothman et al, 1984), multiple quantum filtering method (Keltner et al, 1997), longitudinal scalar order difference method (de Graaf et al, 2001), homonuclear polarization transfer (Shen et al, 2004) and the Hartmann-Hahn transfer method (Choi et al, 2005). Out of these five methods, homonuclear J-difference editing is the most popular and widespread technique due to its relatively easy implementation process on a



commercial scanner and straightforward post-processing and analysis procedures. In essence, the homonuclear J-difference editing utilizes frequency selective  $180^\circ$  refocusing radio frequency (RF) pulses to influence the J evolution of the coupled spins of the same species, but these pulses have no effect on the J evolution of the uncoupled spins. As a result, the subtraction of one spectrum, acquired with the selective refocusing pulses, from the one that without, will diminish the uncoupled spin resonances. In other words, this process allows the selective detection of coupled spin systems from those that are not coupled but spectrally overlapping with the desired resonance peaks.

## **J-difference Editing**

### **Overview of MEGA-PRESS**

One of such homonuclear J-difference editing technique is the MEGA-PRESS technique (Mescher et al, 1998). MEGA-PRESS stands for Mescher-Garwood point resolved spectroscopy, named after two of the original technique creators. This technique was originally created for simultaneous water suppression and GABA editing, using two double-banded Gaussian  $180^\circ$  pulses with one band set on the water resonance frequency and the other one set on the 1.9 ppm GABA C-3 protons, which couple with the nearby C-4 protons at 3.02 ppm. Because of the scalar coupling effect between the GABA methylene protons, the outer two peaks of the C-4 resonances peaks are refocused after the frequency selective Gaussian pulses. During an opposite experiment, if the C-3 peaks are left untouched by setting the band frequency somewhere else other than the 1.9 ppm, then the J evolution of C-4 resonance peaks are not refocused. These two experiments are generally referred to as the ‘editing on’ and the ‘editing off’ acquisitions respectively. By subtracting the two spectra obtained from these two acquisitions, the C-4 resonances can be separated from the total creatine signals at 3.01 ppm, which are not affected

by the two frequency selective refocusing pulses. This process is illustrated in Figure 6-2. Since the first introduction of the MEGA-PRESS technique in 1998, different scanner vendors and spectroscopy research groups have implemented their own versions of the sequence by modifying a pre-existing PRESS sequence.

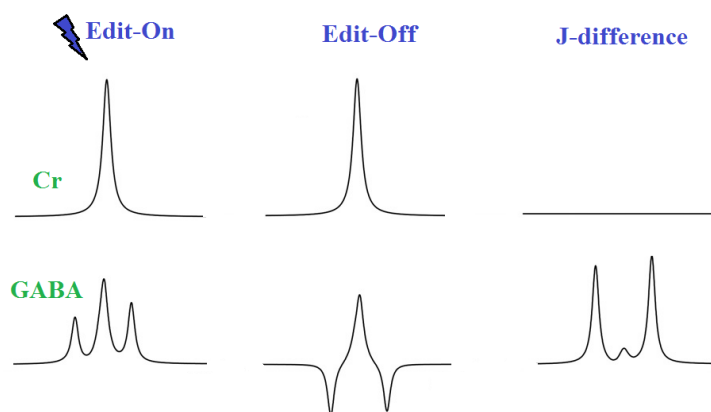


Figure 6-2: Schematic diagram of MEGA-PRESS editing for 3-ppm GABA triplet signals.

### Siemens WIP

Siemens Healthcare has also created their own version of the MEGA-PRESS sequence based on the version published by Mescher et al. This work-in-progress (WIP) pulse sequence package is available for the 3 T MAGNETOM and Verio systems, running syngo MR Numaris 4 VB12A scanner software package. While the original MEGA-PRESS sequence uses double-banded frequency selective pulse, the spectral editing sequence provided by Siemens employs the chemical shift selective suppression (CHESS) approach for water signal suppression, instead of using the MEGA technique. The pulse sequence diagram of the Siemens GABA spectral editing acquisition is shown in Figure 6-3. During the odd data acquisitions or the ‘on-resonance’ acquisitions, the two  $180^\circ$  frequency selective refocusing Gaussian pulses are irradiated at the 1.9 ppm C-3 protons to refocus the J evolution of the coupled C-4 protons. During the even

acquisition or the ‘off-resonance’ acquisitions, the two pulses are irradiated at the 7.5 ppm. Hence, the C-4 protons at 3.02 ppm are not affected. Siemens stores both of these acquisitions into separate raw files, namely raw1 and raw 2, while the editing spectrum is stored in raw3.

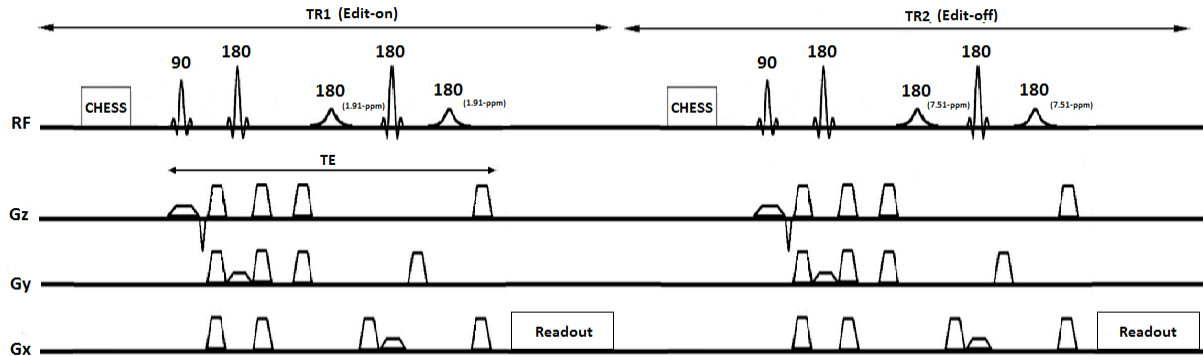


Figure 6-3: Pulse sequence diagram of MEGA-PRESS acquisition with CHES water suppression.

## GABA Resonance Quantification

### LCModel

Similar to the MRS signal quantification of traditional PRESS acquisition, LCModel software package (Provencher 1993) is also capable of quantifying MEGA-PRESS acquired GABA signals. However, since LCModel is a prior-knowledge based frequency domain fitting software, accurate quantification of the edited GABA resonance peaks requires the modification of the basis-files and control parameters. LCModel version 6.3 has been introduced in January of 2013 as the newest software version, in which additional functions have been added to estimate *in vivo* GABA concentrations with the MEGA-PRESS acquisitions. An example of the LCModel fitted MEGA-PRESS spectrum is shown in Figure 6-4. Unlike the PRESS brain spectrum, only a few neurometabolites have been included in the LCModel basis-file, namely NAA, NAAG, Glu, Gln, GSH, and GABA.

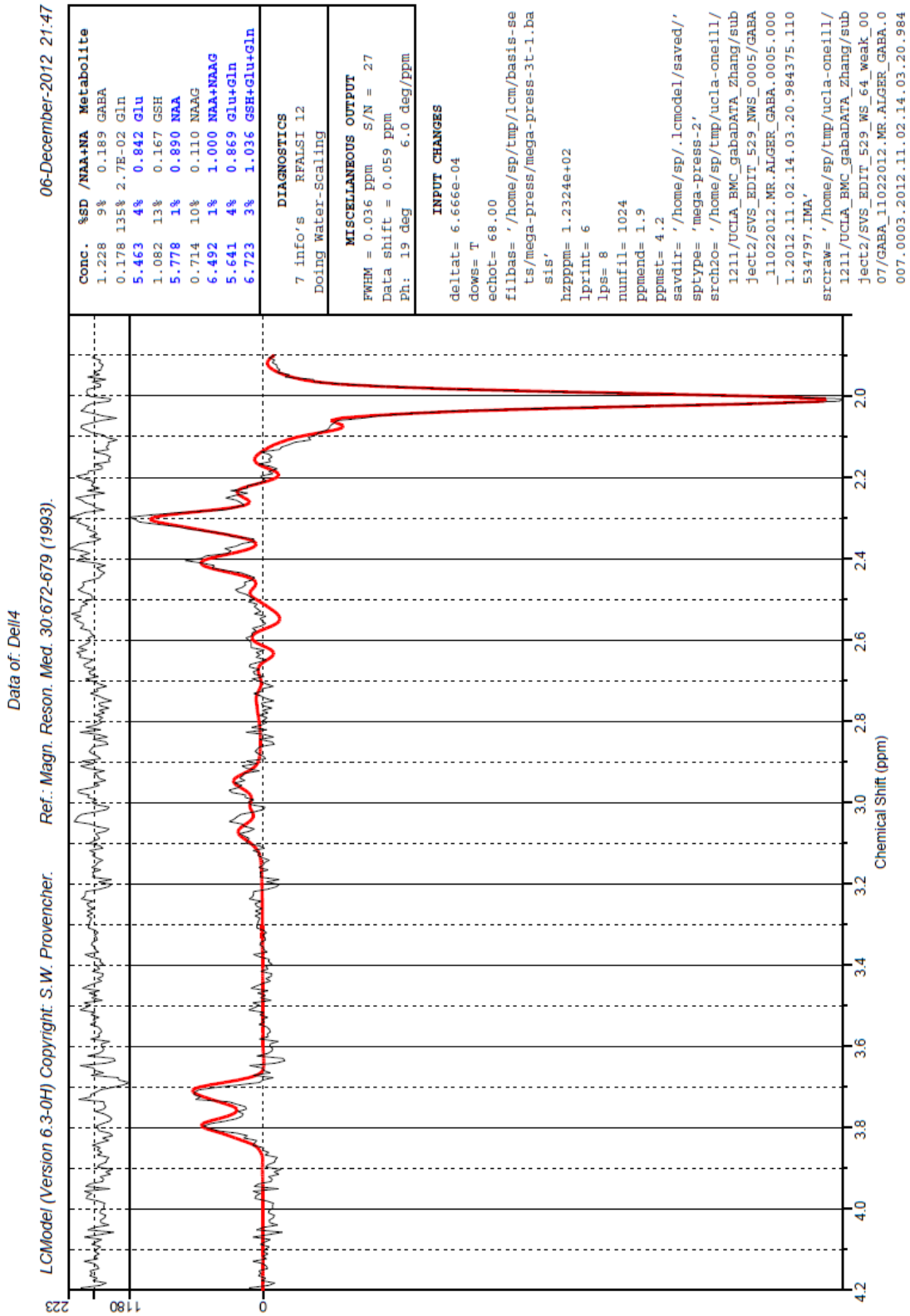


Figure 6-4: An example of the LCModel fitted human brain MEGA-PRESS spectrum.

## Peak Integration

One of the oldest NMR signal analysis methods is the peak integration technique. Mathematically, peak integration simply calculates the area under the resonance signal curve. The reason why integration is performed instead of simply measuring the signal peak height is because the linewidth associated with the  $T_2^*$  relaxation process. As a result, the area of a particular metabolite resonance peak is proportional to the signal intensity. More importantly, it is directly proportional to the number of protons in the acquisition volume. Therefore, peak integration can help to calculate the metabolite concentration *in vivo*. In particular, the edited GABA C-4 resonance peaks can be integrated over the appropriate length in the frequency domain to estimate the total amount of GABA molecules present in the acquisition volume. Similar approach can also be used to calculate the total amount of water molecules present in the acquisition volume.

## Phantom Study

We have obtained the GABA spectral editing WIP pulse sequence from the Siemens Healthcare to facilitate our investigation in the GABAergic neurotransmission abnormalities in major depressive disorder patients (Narr and Randall, PI). The first purpose of this chapter is to give a brief methodology review in GABA resonance detection and measurement with the MEGA-PRESS acquisition technique. The second purpose is to summarize the phantom and human subject studies that I have conducted for my dissertation, using the GABA WIP sequence requested from Siemens.

## Methods

Five phantoms were used in this part of the study to assess the detection reliability of the Siemens' version of the single voxel MEGA-PRESS sequence. The first phantom is a "Braino"

phantom (GE Medical Systems, Milwaukee, WI, USA), containing 12.5 mMol of NAA, 10 mMol of Cr, 3 mMol of Cho, 7.5 mMol of myo-inositol, 12.5 mMol of Glu, 5 mMol of Lactate, 0.1% of sodium azide, 50 mMol of potassium phosphate monobasic, and 56 mMol of sodium hydroxide. The second phantom is a GABA only phantom, containing 20 mMol of GABA. The third phantom contains 4 mMol of GABA, 12.5 mMol of NAA, 10 mMol of Cr, 3 mMol of Cho, 5 mMol of Lactate, and 0.1% of sodium azide. The fourth phantom contains 8 mMol of GABA, 12.5 mMol of NAA, 10 mMol of Cr, 3 mMol of Cho, 5 mMol of Lactate, and 0.1% of sodium azide. The fifth phantom contains 12 mMol of GABA, 12.5 mMol of NAA, 10 mMol of Cr, 3 mMol of Cho, 5 mMol of Lactate, and 0.1% of sodium azide. Two pulse sequences were studied using the previously mentioned five phantoms on a 3 T Siemens MAGNETOM Tim Trio system (Siemens Healthcare, Erlangen, Germany). The two acquisition methods were the PRESS (TR = 3000 ms, TE = 30 ms, 128 averages, 15x15x15 mm<sup>3</sup>, 4:17 min runtime, 12-channel phased array head coil, automatic shimming) and the MEGA-PRESS sequence (TR = 2500 ms, TE = 1/2J= 68 ms, 128 averages, 15x15x15 mm<sup>3</sup>, 8:34 min runtime, 12-channel phased array head coil, automatic shimming). LCMoDel and peak integration methods were used for GABA spectral analysis. For the peak integration method, the water-scaled GABA concentration was estimated with the following equation:

$$[GABA] = \frac{A_{GABA}}{A_{H_2O}} [H_2O] \frac{1 - \exp\left(\frac{-TR}{T_{1H_2O}}\right)}{1 - \exp\left(\frac{-TR}{T_{1GABA}}\right)} * \frac{\exp\left(\frac{-TE}{T_{2H_2O}}\right)}{\exp\left(\frac{-TE}{T_{2GABA}}\right)}, \quad [6 - 1]$$

where  $A_{GABA}$  is the area for the GABA resonance peaks,  $A_{H_2O}$  is the area for the water resonance peak,  $[H_2O]$  is the water concentration,  $T_{1H_2O}$  and  $T_{2H_2O}$  are the  $T_1$  and  $T_2$  values of water (Wansapura et al 1999), and  $T_{1GABA}$  and  $T_{2GABA}$  are the  $T_1$  and  $T_2$  values of GABA (Träber et al 2004).

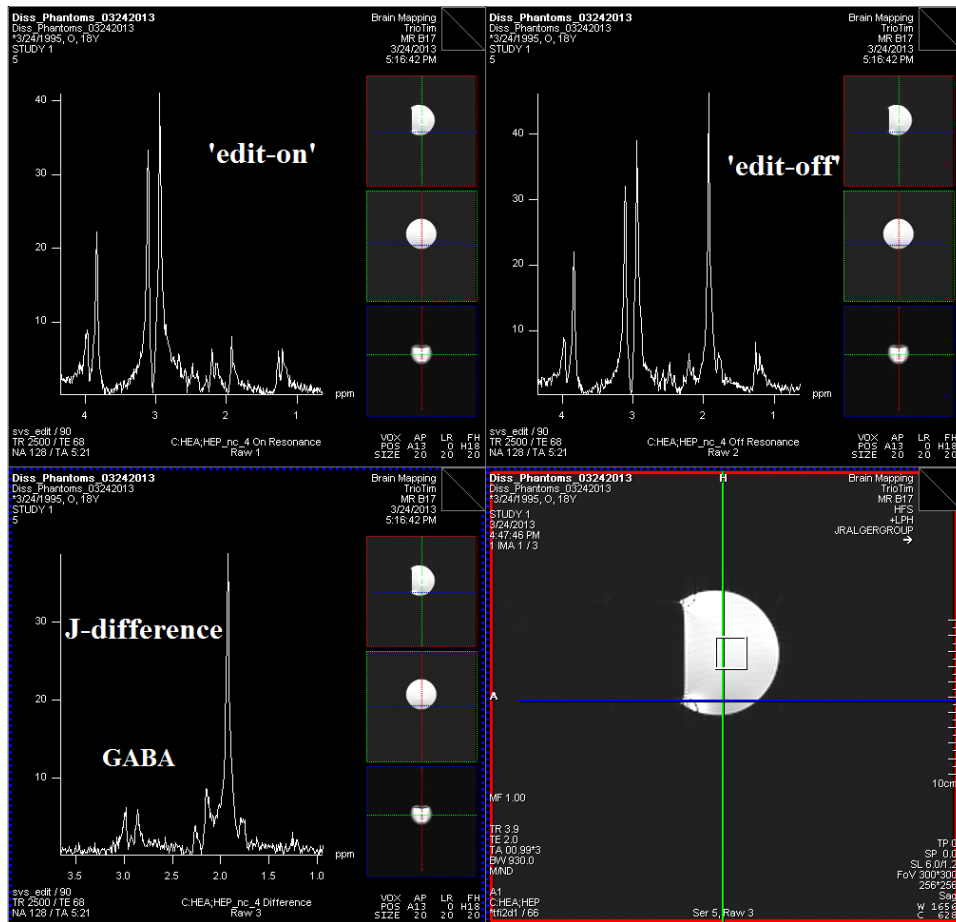


Figure 6-5: MEGA-PRESS acquisition on a phantom with 8 mMol of GABA.

## Results

Figure 6-5 shows examples of the MRS spectra acquired with the MEGA-PRESS pulse sequence using the 8 mMol GABA phantom. The top left corner shows the MEGA-PRESS ‘edit-on’ spectrum. Due to the  $180^\circ$  1.9 ppm frequency selective pulse, the NAA signal peak at 2.0 ppm has been completely dephased. The top right corner shows the MEGA-PRESS ‘edit-off’ spectrum. Since the frequency selective pulse is set at 7.5 ppm during this acquisition, the spectrum can be considered as a TE 68 ms PRESS acquisition. The bottom left corner shows the subtraction difference between the ‘edit-on’ and the ‘edit-off’ spectra, also known as the edited spectrum. In this edited spectrum, the resonance signals that are not affected by the 1.9 ppm

frequency selective pulse, have been completed eliminated and the pseudo doublet peaks at 3.0 ppm can be ascribed to be the GABA C-4 resonances.

Since the ‘edit-off’ acquisition can be essentially considered as an independent TE 68 ms PRESS acquisition, the ‘edit-off’ spectrum can also be analyzed with LCModel to obtain useful metabolite concentration information in both phantoms and human subjects. As shown in Figure 6-6, spectra from both the TE 30 PRESS and the TE 68 MEGA-PRESS ‘edit-off’ were quantified with LCModel. The results of the quantification are plotted against the actual Braino phantom metabolite levels.

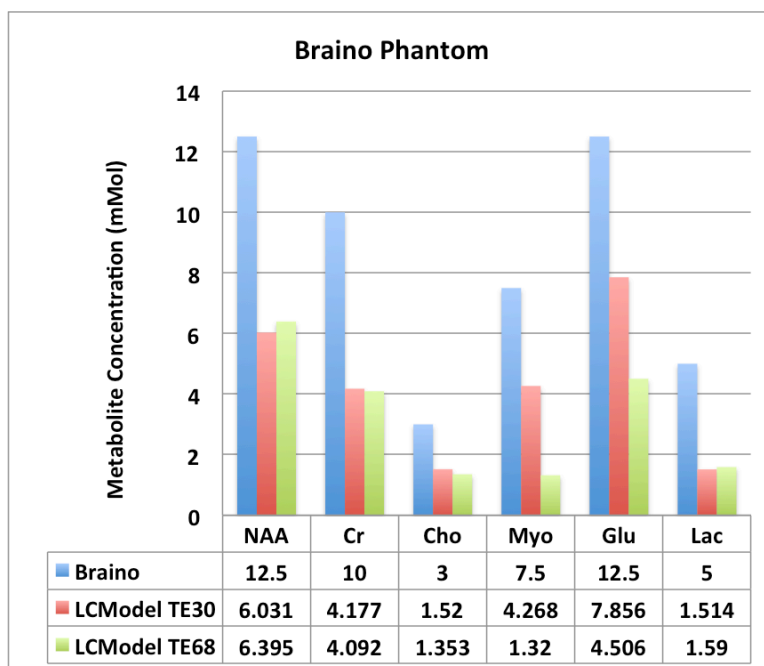


Figure 6-6: Braino phantom metabolite concentration measurement with TE 30 PRESS and MEGA-PRESS ‘edit-off’ TE 68 acquisition.

Figure 6-7 (a) and (b) show the GABA concentration levels in four phantoms having GABA concentrations ranging from 0 to 12 mMol. The measurements were done using the TE 30 PRESS and the TE 68 MEGA-PRESS ‘edit-off’ acquisitions. These two figures indicate that



LCModel quantification systematically underestimates the actual *in vitro* phantom values of GABA. Figure 6-7 (c) shows the GABA concentration level for four phantoms having GABA levels ranging from 4 to 20 mMol. The measurements were done using the TE 68 MEGA-PRESS edited spectra. Spectral quantification was analyzed with both the LCModel and the peak integration methods. These results also indicates that LCModel underestimates the actual *in vitro* GABA concentration values and that the peak integration method performs better than LCModel in quantifying the GABA edited spectra *in vitro*.

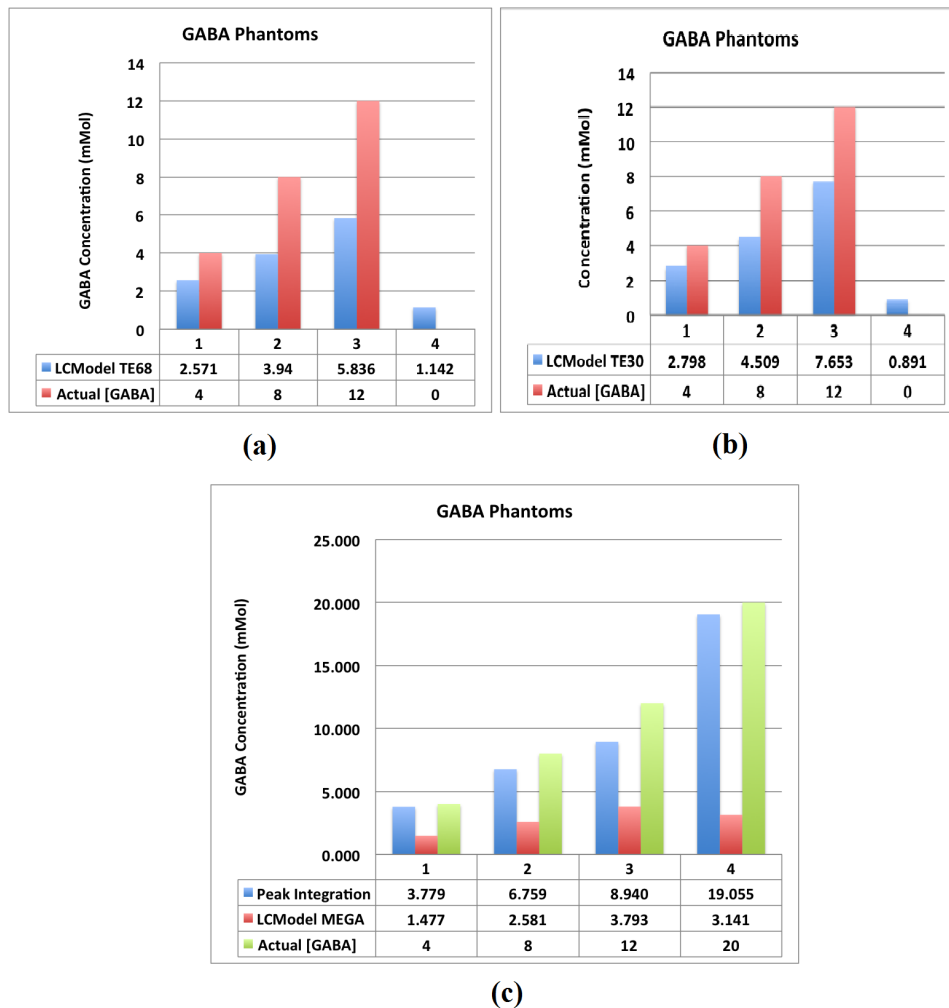


Figure 6-7: GABA concentrations in phantoms with 0 mMol, 4 mMol, 8 mMol, 12 mMol, and 20 mMol of GABA, using TE 68 MEGA-PRESS 'edit off' (a), TE 30 PRESS (b), and the MEGA-PRESS acquisition (c).

## In vivo Study

### Methods

In this part of the study, the single voxel MEGA-PRESS (3 T Siemens Tim Trio, TR = 2000 ms, TE = 1/2J= 68 ms, 128 averages, 20x30x40 mm<sup>3</sup>, 8:34 min runtime, 12-channel phased array head coil, automatic shimming) was performed in ten healthy adult human subjects (5 female and 5 male, age ranges from 19 to 53 years old) in the anterior cingulate (AC) region. The J-difference edited spectrum is shown on the left of Figure 6-8. The edited GABA signal is circled in orange in the figure. The GABA signal appears at -1.7 ppm on the plot because the water frequency (4.7 ppm) is used as an internal reference. LCModel and peak integration methods were also used for GABA spectral analysis in this *in vivo* study. GABA concentrations for peak integration were calculated using an equation that is a slightly different from Equation 6-1:

$$[GABA] = \frac{A_{GABA}}{A_{H_2O}} [H_2O] V_{H_2O} \frac{1 - \exp\left(\frac{-TR}{T_{1H_2O}}\right)}{1 - \exp\left(\frac{-TR}{T_{1GABA}}\right)} * \frac{\exp\left(\frac{-TE}{T_{2H_2O}}\right)}{\exp\left(\frac{-TE}{T_{2GABA}}\right)}, \quad [6 - 2]$$

where  $V_{H_2O}$  is the water visibility in human brain (Mullins et al 2013).

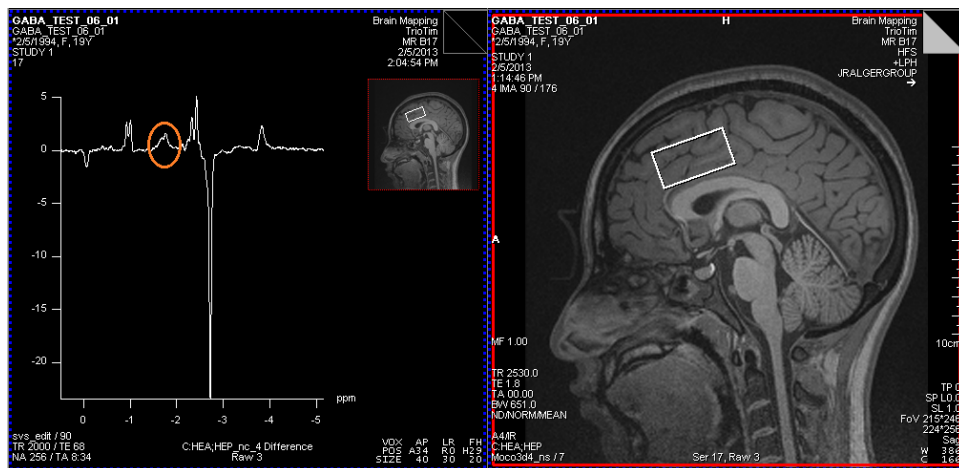
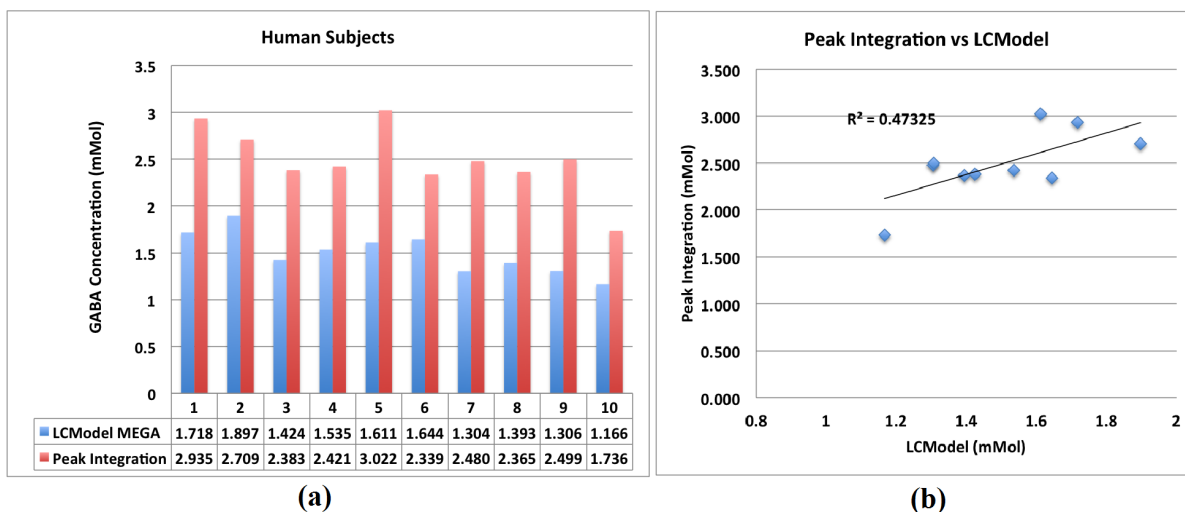


Figure 6-8: MEGA-PRESS single voxel acquisition in human brain in vivo at 3T and its J-difference spectrum (left).

## Results



**Figure 6-9: GABA concentrations in ten human subjects (a) and the measurement correlation between the LCMoDel and the peak integration method.**

Figure 6-9 (a) shows the LCMoDel and the peak integration determined GABA concentration levels in the anterior cingulate cortex of the ten healthy control subjects. The mean and the standard deviation are 1.5 mMol and 0.22 mMol for the LCMoDel measurements and 2.49 mMol and 0.36 mMol for the peak integration measurements. The inter-subject CV for both methods is 14.4% for peak integration and 14.6% for LCMoDel. Figure 6-9 (b) shows that the two analytical methods correlate well with one another, but the LCMoDel output values are closer to the physiological GABA concentration range of 1 to 2 mMol.

## Discussions

This study demonstrates our ability to collect single voxel J-edited GABA spectrum *in vivo* in a reasonable scanning time of under 10 minutes, using the Siemens WIP MEGA-PRESS pulse sequence. We were able to collect GABA spectra in both phantoms and human subjects; however, one of the remaining challenges is the accurate and reliable quantification of the 3 ppm GABA resonances in the edited spectra. We have applied both the peak integration method and

the LCModel method to quantify GABA signals and observed better performance with peak integration for *in vitro* data. LCModel estimates could be biased because of assumptions LCModel employs for concentration calculation for *in vivo* human brain metabolite measurements. For the *in vivo* experiments, both methods seem to offer the same measurement CV between subjects, but the LCModel water-scaled GABA concentrations are closer to the previously reported physiological GABA level.

Some of the limitations of this study include: (1) we did not account for the macromolecule (MM) signals coedited with the 3 ppm GABA signal and (2) only one acquisition was obtained per subject during the *in vivo* study as well as the phantom study. Contamination of the GABA spectra by co-edited MM signals is a major concern in MEGA-PRESS acquisitions (Mullins et al 2013). Current solutions to the MM problem include: symmetrical elimination of the undesirable MM signals using selective editing pulse at 1.7 ppm (Henry et al 2001), modeling MM signals and GABA signals in the LCModel basis file, and direct measurement of MM baseline signals through metabolite nulling (Behar et al 1994). Acknowledgement of the MM signal contamination issue is necessary since the signal contribution from the MM resonance can render the GABA signal quantification inaccurate. Hence, alternative post processing methods should be investigated to separate the MM signals from the GABA signals in the MEGA-PRESS acquisition.

## Conclusions

We have applied the WIP MEGA-PRESS pulse sequence implemented by Siemens Healthcare to measure GABA concentrations in both phantoms and healthy human controls. Two MRS quantification methods were used to quantify the C4 GABA resonances with the edited spectra. We have found that both the LCModel and peak integration techniques offer similar

inter-subject CV in GABA signal quantifications. Peak integration is given nearly the correct results in phantoms, but LCModel is underestimating the values in phantoms.

## References

- Behar, K. L., Rothman, D. L., Spencer, D. D., & Petroff, O. A. (1994). Analysis of macromolecule resonances in  $^1\text{H}$  NMR spectra of human brain. *Magn Reson Med*, *32*, 294-302.
- Choi, I. Y., Lee, S. P., & Shen, J. (2005). Selective homonuclear Hartmann-Hahn transfer method for in vivo spectral editing in the human brain. *Magn Reson Med*, *53*, 503-10.
- de Graaf, R. A., & Rothman, D. L. (2001). Detection of  $\gamma$ -Aminobutyric Acid (GABA) by Longitudinal Scalar Order Difference Editing. *Journal of Magnetic Resonance*, *152*, 124-31.
- Edden, R. A., & Barker, P. B. (2007). Spatial effects in the detection of gamma-aminobutyric acid: improved sensitivity at high fields using inner volume saturation. *Magn Reson Med*, *58*, 1276-82.
- Edden R. A., Crocetti D., Chu H., Gilbert D. L., Mostofsky S. H. (2012). Reduced gaba concentration in attention-deficit/hyperactivity disorder. *Archives of General Psychiatry*, *69*, 750-53.
- Hasler, G., van der Veen, J. W., Tumonis, T., Meyers, N., Shen, J., & Drevets, W. C. (2007). Reduced prefrontal glutamate/glutamine and gamma-aminobutyric acid levels in major depression determined using proton magnetic resonance spectroscopy. *Arch Gen Psychiatry*, *64*, 193-200.
- Henry, M. E., Lauriat, T. L., Shanahan, M., Renshaw, P. F., & Jensen, J. E. (2011). Accuracy and stability of measuring GABA, glutamate, and glutamine by proton magnetic resonance spectroscopy: a phantom study at 4 Tesla. *J Magn Reson*, *208*, 210-8.
- Henry, P. G., Dautry, C., Hantraye, P., & Bloch, G. (2001). Brain GABA editing without macromolecule contamination. *Magn Reson Med*, *45*, 517-20.
- Jensen, J. E., Frederick, B. D., Wang, L., Brown, J., & Renshaw, P. F. (2005). Two-dimensional, J-resolved spectroscopic imaging of GABA at 4 Tesla in the human brain. *Magn Reson Med*, *54*, 783-8.
- Kegeles Ls, M. X. S. A. D., & et al. (2012). ELevated prefrontal cortex  $\gamma$ -aminobutyric acid and glutamate-glutamine levels in schizophrenia measured in vivo with proton magnetic resonance spectroscopy. *Archives of General Psychiatry*, *69*, 449-59.
- Keltner, J. R., Wald, L. L., Frederick, B. D., & Renshaw, P. F. (1997). In vivo detection of

- GABA in human brain using a localized double-quantum filter technique. *Magn Reson Med*, 37, 366-71.
- Kubas, B., Kulak, W., Sobaniec, W., Tarasow, E., Lebkowska, U., & Walecki, J. (2012). Metabolite alterations in autistic children: a <sup>1</sup>H MR spectroscopy study. *Adv Med Sci*, 57, 152-6.
- Mescher, M., Merkle, H., Kirsch, J., Garwood, M., & Gruetter, R. (1998). Simultaneous in vivo spectral editing and water suppression. *NMR Biomed*, 11, 266-72.
- Mullins, P. G., McGonigle, D. J., O'Gorman, R. L., Puts, N. A. J., Vidyasagar, R., Evans, C. J., & Edden, R. A. E. (2013). Current practice in the use of MEGA-PRESS spectroscopy for the detection of GABA. *NeuroImage*.
- Nikolaus, S., Antke, C., Beu, M., & Muller, H. W. (2010). Cortical GABA, striatal dopamine and midbrain serotonin as the key players in compulsive and anxiety disorders--results from in vivo imaging studies. *Rev Neurosci*, 21, 119-39.
- O'Gorman, R. L., Michels, L., Edden, R. A., Murdoch, J. B., & Martin, E. (2011). In vivo detection of GABA and glutamate with MEGA-PRESS: reproducibility and gender effects. *J Magn Reson Imaging*, 33, 1262-7.
- Petroff, O. A., Rothman, D. L., Behar, K. L., & Mattson, R. H. (1996). Low brain GABA level is associated with poor seizure control. *Ann Neurol*, 40, 908-11.
- Provencher, S. W. (1993). Estimation of metabolite concentrations from localized in vivo proton NMR spectra. *Magn Reson Med*, 30, 672-9.
- Rojas, D. C., Singel, D., Steinmetz, S., Hepburn, S., & Brown, M. S. Decreased left perisylvian GABA concentration in children with autism and unaffected siblings. *NeuroImage*.
- Rothman, D. L., Behar, K. L., Hetherington, H. P., & Shulman, R. G. (1984). Homonuclear <sup>1</sup>H double-resonance difference spectroscopy of the rat brain in vivo. *Proc Natl Acad Sci U S A*, 81, 6330-4.
- Rothman, D. L., Petroff, O. A., Behar, K. L., & Mattson, R. H. (1993). Localized <sup>1</sup>H NMR measurements of gamma-aminobutyric acid in human brain in vivo. *Proc Natl Acad Sci U S A*, 90, 5662-6.
- Rowland, L. M., Kontson, K., West, J., Edden, R. A., Zhu, H., Wijtenburg, S. A., Holcomb, H. H., & Barker, P. B. (2012). In Vivo Measurements of Glutamate, GABA, and NAAG in Schizophrenia. *Schizophrenia Bulletin*.
- Sanacora, G., Gueorguieva, R., Epperson, C. N., Wu, Y. T., Appel, M., Rothman, D. L., Krystal, J. H., & Mason, G. F. (2004). Subtype-specific alterations of gamma-aminobutyric acid and glutamate in patients with major depression. *Arch Gen Psychiatry*, 61, 705-13.

- Shen, J., Yang, J., Choi, I. Y., Li, S. S., & Chen, Z. (2004). A new strategy for in vivo spectral editing. Application to GABA editing using selective homonuclear polarization transfer spectroscopy. *J Magn Reson*, *170*, 290-8.
- Simister, R. J., McLean, M. A., Barker, G. J., & Duncan, J. S. (2009). Proton MR spectroscopy of metabolite concentrations in temporal lobe epilepsy and effect of temporal lobe resection. *Epilepsy Res*, *83*, 168-76.
- Simpson, H. B., Shungu, D. C., Bender, J., Jr., Mao, X., Xu, X., Slifstein, M., & Kegeles, L. S. (2012). Investigation of cortical glutamate-glutamine and gamma-aminobutyric acid in obsessive-compulsive disorder by proton magnetic resonance spectroscopy. *Neuropsychopharmacology*, *37*, 2684-92.
- Träber, F., Block, W., Lamerichs, R., Gieseke, J., & Schild, H. H. (2004). <sup>1</sup>H metabolite relaxation times at 3.0 tesla: Measurements of T1 and T2 values in normal brain and determination of regional differences in transverse relaxation. *Journal of Magnetic Resonance Imaging*, *19*, 537-45.
- Wansapura, J. P., Holland, S. K., Dunn, R. S., & Ball, W. S. (1999). NMR relaxation times in the human brain at 3.0 tesla. *Journal of Magnetic Resonance Imaging*, *9*, 531-38.

## Chapter 7 A Padé Approximant Method for the Analysis of Proton Magnetic Resonance Spectroscopy Signals of the Human Brain

### Introduction

Accurate quantification of *in vivo* localized proton magnetic resonance spectroscopy ( $^1\text{H}$ -MRS) signals in the human brain is one of the important steps in differentiating abnormal neurometabolite concentration values from those of healthy brains. Overlapping signal peaks and significant baseline contamination contributed by macromolecules can interfere with spectral quantification. We propose to use a quantification technique called the Fast Padé Transform (FPT), which does not require prior knowledge (i.e. basis sets). We investigated the FPT method as an alternative *in vivo* metabolite quantification technique.

The FPT method was introduced by Belkic as a parametric MRS signal processing and quantification technique that offers exact and closed form analytical solutions to MRS spectral peak parameters (Belkic, 2001). It is mathematically based upon the Padé approximant from the field of numerical analysis and the causal z-transform from the field of spectral analysis. FPT has been previously used to analyze the exponentially decaying NMR signals with various line-shapes (Maltempo, 1986; Robert et al, 1997; Higinbotham & Marshall, 2001). Belkic (Belkic 2006) and Williamson (Williamson et al, 2006) have also shown it to be superior to the standard discrete fast Fourier transform in calculating and forming *in vivo* NMR spectra. In this study, we compared the FPT method to the LCModel (Provencher 1993) method using both simulated and *in vivo* human brain data. The goal is to evaluate FPT accuracy in quantifying neurometabolites N-acetylaspartate (NAA), choline (Cho), creatine (Cr), glutamate (Glu), glutamine (Gln), and  $\gamma$ -Aminobutyric acid (GABA).



## Theory

Time domain <sup>1</sup>H-MRS spectra can be viewed mathematically as a finite series of exponentially decaying functions. Let  $S(t)$  represent a finite digitized time domain MRS signal with  $N$  data points and  $K$  metabolite resonance signals:

$$S(t) = \sum_{n=0}^{N-1} \sum_{k=1}^K A_k^n e^{-i\phi_k^n} e^{-(i\omega_k^n + R_k^n)t}, \quad [7-1]$$

where  $A_k$  and  $R_k$  are the metabolite signal amplitude and  $T_2^*$  relaxation rate constant and  $\phi_k$  and  $\omega_k$  are the metabolite signal phase and frequency. Let the data-sampling time interval be  $\tau$ , which equals to the inverse of data sampling bandwidth, and  $t = \tau * n$ . We can simplify Equation 7-1 by introducing two variables  $\{d_k, \Omega_k\}$  and also let  $\Omega_k = \omega_k^n + R_k^n$ :

$$d_k = A_k^n e^{-i\phi_k^n}, \quad [7-2]$$

$$u_k = e^{-(i\omega_k^n + R_k^n)t\tau} = e^{i\Omega_k\tau}, \quad [7-3]$$

$$S(u) = \sum_{n=0}^{N-1} \sum_{k=1}^K d_k u_k^{-n}. \quad [7-4]$$

If we let  $n$  goes to infinity, then we can approximate Equation 7-4 using the geometric series sum rule (Equation 7-5):

$$\sum_{r=0}^{\infty} a^r = \frac{a}{1-a}, \quad [7-5]$$

$$\begin{aligned} S(u) &= \sum_{k=1}^K \sum_{n=0}^{\infty} d_k * u_k^{-n} = \sum_{k=1}^K d_k * \frac{1}{1 - \frac{1}{u_k}} \\ &= \sum_{k=1}^K d_k * \frac{1}{u_k - 1}. \quad [7-6] \end{aligned}$$

If we can solve for  $\{d_k, \Omega_k\}$  explicitly, then the real part of  $\Omega_k$  divided by  $\pi$  is the linewidth of the  $k$ th metabolite signal, the imaginary part of  $\Omega_k$  is the frequency of the  $k$ th metabolite signal. Similarly, the absolute value of  $d_k$  is the signal amplitude of the  $k$ th metabolite signal and the argument of  $d_k$  is the phase of the  $k$ th metabolite signal. The relationships between  $\{d_k, \Omega_k\}$  and some of the important MRS parameters are listed in Table 7-1.

**Table 7-1: Summary of the relationships between  $\{d_k, \Omega_k\}$  and MRS parameters for the  $k$ th metabolite.**

$\{d_k, \Omega_k\}$	Parameter
$\frac{Re(\Omega_k)}{\pi}$	Linewidth
$Im(\Omega_k)$	Frequency (Chemical Shift)
$ d_k $	Amplitude
$Arg(d_k)$	Phase

To solve Equation 7-6 and to obtain physical parameters for each metabolite, the Padé approximant technique is used. The technique introduce two polynomials  $P_K(u)$  and  $Q_K(u)$ :

$$P_K(u) = p_0 + p_1u + p_2u^2 + p_3u^3 + \dots + p_Ku^K, \quad [7-7]$$

$$Q_K(u) = 1 + q_1u + q_2u^2 + q_3u^3 + \dots + q_Ku^K. \quad [7-8]$$

To obtain a rational approximation to the time domain signal  $S(t)$  on  $[K, K]$ :

$$S(u) = \sum_{k=1}^K d_k * \frac{1}{u_k - 1} = \frac{P_K(u)}{Q_K(u)}. \quad [7-9]$$

In Equation 7-9,  $\frac{P_K(u)}{Q_K(u)}$  is said to be the Padé approximant of  $S(u)$  if and only if function  $S(u)$

and  $\frac{P_K(u)}{Q_K(u)}$  equal to each other when  $u$  equals to zero and also their subsequent derivatives

evaluated at zero equal to each other:

$$S(0) = \frac{P_K(0)}{Q_K(0)}, \quad [7-10]$$

$$\frac{d^k}{du^k} S(0) = \frac{d^k}{du^k} \left( \frac{P_K(0)}{Q_K(0)} \right). \quad [7-11]$$

Equation 7-10 can yield a set of linear equations by multiplying  $Q_K(0)$  on both sides of the equations. By comparing coefficients with the same powers and setting  $u$  equals zero, it is possible to obtain

$$\begin{aligned} c_0 - p_0 &= 0 \\ c_0 q_1 + c_1 - p_1 &= 0 \\ c_0 q_2 + c_1 q_1 + c_2 - p_2 &= 0 \\ &\vdots \\ c_0 q_k + c_1 q_{k-1} + \dots + c_k - p_k &= 0, \quad [7-12] \end{aligned}$$

and

$$\begin{aligned} c_1 q_k + c_2 q_{k-1} + \dots + q_1 c_k - c_{k+1} &= 0 \\ c_2 q_k + c_3 q_{k-1} + \dots + q_1 c_{k+1} - c_{k+2} &= 0 \\ c_3 q_k + c_4 q_{k-1} + \dots + q_1 c_{k+2} - c_{k+3} &= 0 \\ &\vdots \\ c_k q_k + c_{k+1} q_{k-1} + \dots + q_1 c_{2k-1} - c_{2k} &= 0. \quad [7-13] \end{aligned}$$

We can rewrite Equation 7-12 and 7-13 into more compact forms:

$$c_{n+k} = \sum_{k=1}^K q_k * c_{2k-n} \quad (1 \leq n \leq K), \quad [7-14]$$

$$p_k = \sum_{n=0}^k c_n * q_{k-n} \quad (0 \leq k \leq K). \quad [7-15]$$

Solving Equation 7-14 and 7-15 provides the coefficients of the polynomial  $P_K(u)$  and  $Q_K(u)$ . Coefficients of  $Q_K(u)$  can be determined numerically using the method of singular values decomposition (SVD) of a Hankel matrix derived from the original time domain data.

Coefficients of  $P_K(u)$  can be calculated from the coefficients of  $Q_K(u)$  using equation 7-15. As a result, going back to the original goal of solving the values of  $\{d_k, \Omega_k\}$ , we can determine  $u_k$  by finding the roots of polynomial  $Q_K(u)$ . From  $u_k$  we can obtain solutions to  $\Omega_k$ :

$$\Omega_k = \frac{i}{\tau} * \ln(u_k). \quad [7-16]$$

To solve  $d_k$ , we can apply Cauchy's residue theorem to Equation 7-9 since  $S(u)$  has a simple pole at 1 and it is possible to obtain:

$$Res(S, 1) = d_k = \frac{P_K(u_k)}{Q_K'(u_k)}, \quad [7-17]$$

notice that  $Q_K'(u_k)$  is in its differential form.

Once all of the values of  $\{d_k, \Omega_k\}$  have been extracted from the FID signal, the complex frequency domain spectrum is obtained from the Heaviside partial fraction expansion for spectral visualization purpose:

$$S(u) = \frac{P_K(u)}{Q_K(u)} = \sum_{k=1}^K \frac{d_k}{u - u_k}. \quad [7-18]$$

It can be seen from the derivations that some important metabolite MRS parameters can be explicitly solved using the original free induction decay data by applying the Padé approximant technique. Metabolite amplitude values determined from Equation 7-17 can be used to calculate metabolite concentration values, since the MRS signal amplitude is directly proportional to amount of protons contained in a particular acquisition volume.

### Froissart Doublet

In the method of Padé approximant, some interesting observations can be made in the distribution of the zeros and the poles values (Besis 1996). The poles are the roots of the polynomial  $Q_K(u)$  and the zeros are the roots of the polynomial  $P_K(u)$ . French physicist Marcel

Froissart first discovered that Padé approximants to a power series is disturbed by random noise. He observed that when using Padé approximant to numerically calculate experimental data with random noise, the distributions of pole and zero pair can be divided into three categories. 1) Doublet pole-zero pair resides at a distance on the order of numerical round off errors; 2) Doublet pole-zero pair resides at a distance on the order of random noise in the experimental data; 3) The rest of the poles and zeros can be ascribed to the analytic structure representing the experimental data. By throwing away the first two categories of pole and zero pair (or doublets), a data filtering or denoising effect can be achieved. Figure 7-1 shows the poles (in red) and zeros (in blue) from an analysis of an *in vivo* MR spectrum (acquired with PRESS TE 30 ms method) using the FPT algorithm. Some of the poles and zeros are tightly paired up near the vicinity of the unit circle (black solid curve), so these Froissart doublets actually belong to either the first or the second category of poles and zeros. In theory, genuine MR resonances can be separated from noise by identifying these Froissart doublets, which is a unique characteristic offered by the Padé approximant technique in comparison with other signal processing methods. The practical problem is defining how close a pole and zero pair must be to identify them as a Froissart doublet. We aim to implement this interesting denoising technique into our FPT computer algorithm and test its reliability with data at different noise levels.

## Software

In order to measure the metabolite concentrations using the Padé approximant method, a FPT algorithm was implemented in MATLAB (MathWorks, Naticks MA). Standard MATLAB functions were employed in this algorithm. MRS (water suppressed and non water suppressed) data can be processed with this FPT program to obtain parametric signal information (frequency, line-width, phase, and amplitude) for each signal presents in the data. Metabolite concentration

levels are calculated using the ratio of metabolite and water amplitude information scaled to the number of protons that produce the particular signal. The MATLAB software first reads in the DICOM or RDA data generated by the Siemens MRI scanner, then the coefficients of polynomial  $Q_K(u)$  is solved using the standard MATLAB SVD function of the Hankel data matrix derived from the time domain signal. The coefficients of polynomial  $P_K(u)$  are calculated from the coefficients of  $Q_K(u)$ . In order to generate a set of values for  $\{d_k, \Omega_k\}$ , the roots of  $P_K(u)$  and  $Q_K(u)$  are solved using standard MATLAB root finding function, as well as by identifying the Froissart doublets by setting exclusion criterion for the distance between the poles and zeros of  $Q_K(u)$  and  $P_K(u)$ . After Froissart doublet denoising, ‘genuine’  $u_k$  values are used for the calculation of  $d_k$  and  $\Omega_k$ . The values of  $\{d_k, \Omega_k\}$  are stored in a table called the Padé table, from which metabolite amplitude, frequency, phase, and linewidth information can be extracted manually. As the name of the FPT also suggests, this method can also be used to transform time domain data to frequency domain for the purpose of spectral visualization.

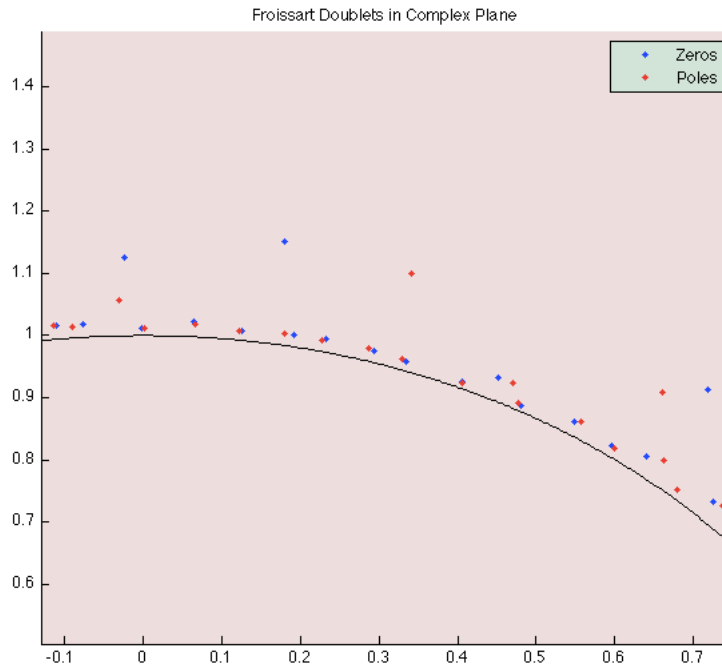


**Figure 7-1: Froissart doublets present in the FPT analysis of in vivo MR spectrum from TE 30 PRESS acquisition (plotted in the complex plane, black solid curve represents the unit circle).**

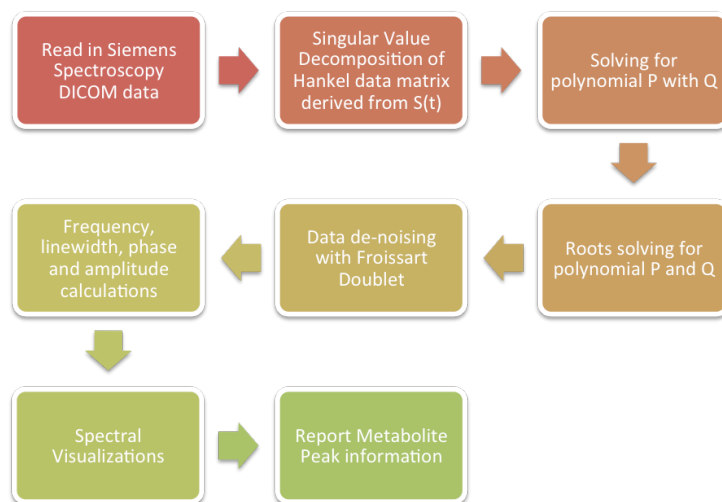


**Figure 7-2: A flowchart diagram of the FPT algorithm implemented in MATLAB.**

## Validation with Simulation

In order to validate our version of the FPT algorithm, simulated spectra were created using the VeSPA Priorset software package. TE 30 PRESS simulations were performed for 3 T with commonly observed neurometabolites: NAA, NAAG, GABA, Cho, Cr, glucose-alpha, glucose-beta, Glu, Gln, glycerophosphorylcholine, myo-inositol, scyllo-inositol, lactate, phosphocreatine, and taurine. Gaussian noise was added to the simulated spectra to model different SNR levels in reference to the Cr peak. The FPT algorithm was used to analyze the amplitude information from five of the metabolites.

Froissart doublet denoising method was tested with the simulated spectra at different SNR. Figure 7-3 (a) shows an example of the simulated human brain spectrum from the fast Fourier transform (FFT) operation, (b) shows the simulated spectrum with added noise (SNR = 20), and (c) is the FPT frequency domain spectrum using the Froissart denoising technique. Excellent agreement can be seen between (a) and (c) with the exceptions of the Lac resonance

peaks. The absence of the Lac doublets in the FPT Froissart doublet denoised spectrum indicates that this method can reliably perform spectral visualization for the resonance peaks greater than the intrinsic noise level in the spectral data. . In other words the Froissart method eliminated these signals as being noise. Figure 7-4 shows the linear relationship between the amount of noise and the Zero-Pole distance in the FPT algorithm. As the noise level increases in the spectral data, the distance between the Froissart doublets increases as well and this observation agrees with the general conditions of the Padé approximant technique. Figure 7-5 shows the Froissart doublet denoised simulated spectra with SNR ranging from 8 to 20.

Figure 7-6 shows the FPT algorithm measurement percentage errors verses the SNR levels using the simulated brain MR spectra. Since the true amplitude values are known for these simulated resonance peaks, the percentage error can be used to evaluate the accuracy of the FPT algorithm. From this figure it can be concluded that the FPT algorithm is excellent (percentage error < 6%) in the quantification of the total NAA signal (2.0 ppm), total Choline signal (3.2 ppm), and the algorithm gives acceptable (percentage error < 10%) performance in quantifying the total Cr resonance (3.0 ppm). Due to the overlap of GABA signal and Cr signal in the 3.0 ppm region, GABA was not accurately detected by the FPT algorithm, hence it is not presented in the plot. The FPT algorithm shows acceptable (percentage error < 10%) quantification error for the Glu 2.34 ppm and 2.35 resonance peaks at SNR level higher than 17, but it fails to measure the Gln peaks at 2.43 ppm and 2.46 ppm with acceptable accuracy.



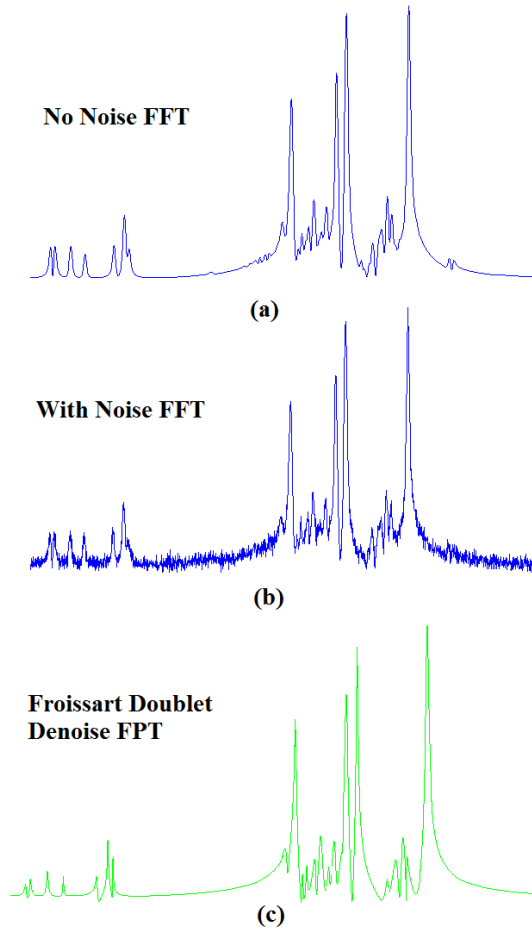


Figure 7-3: PRESS simulated MRS frequency domain magnitude spectra at 3 T without noise (a), with noise SNR = 20 (b), and the Froissart doublet denoised FPT spectrum (c).

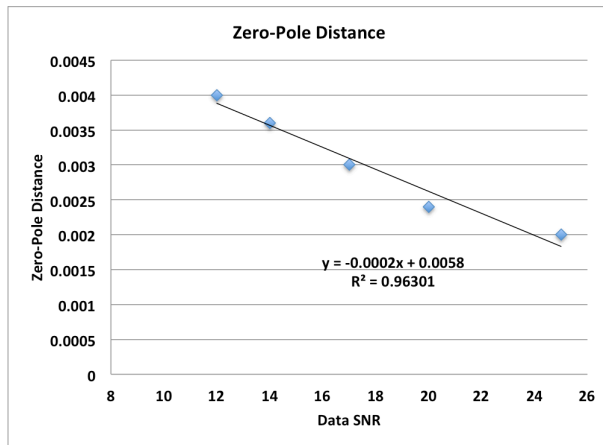


Figure 7-4: Linear relationship between data SNR and the Zero-Pole Distance.

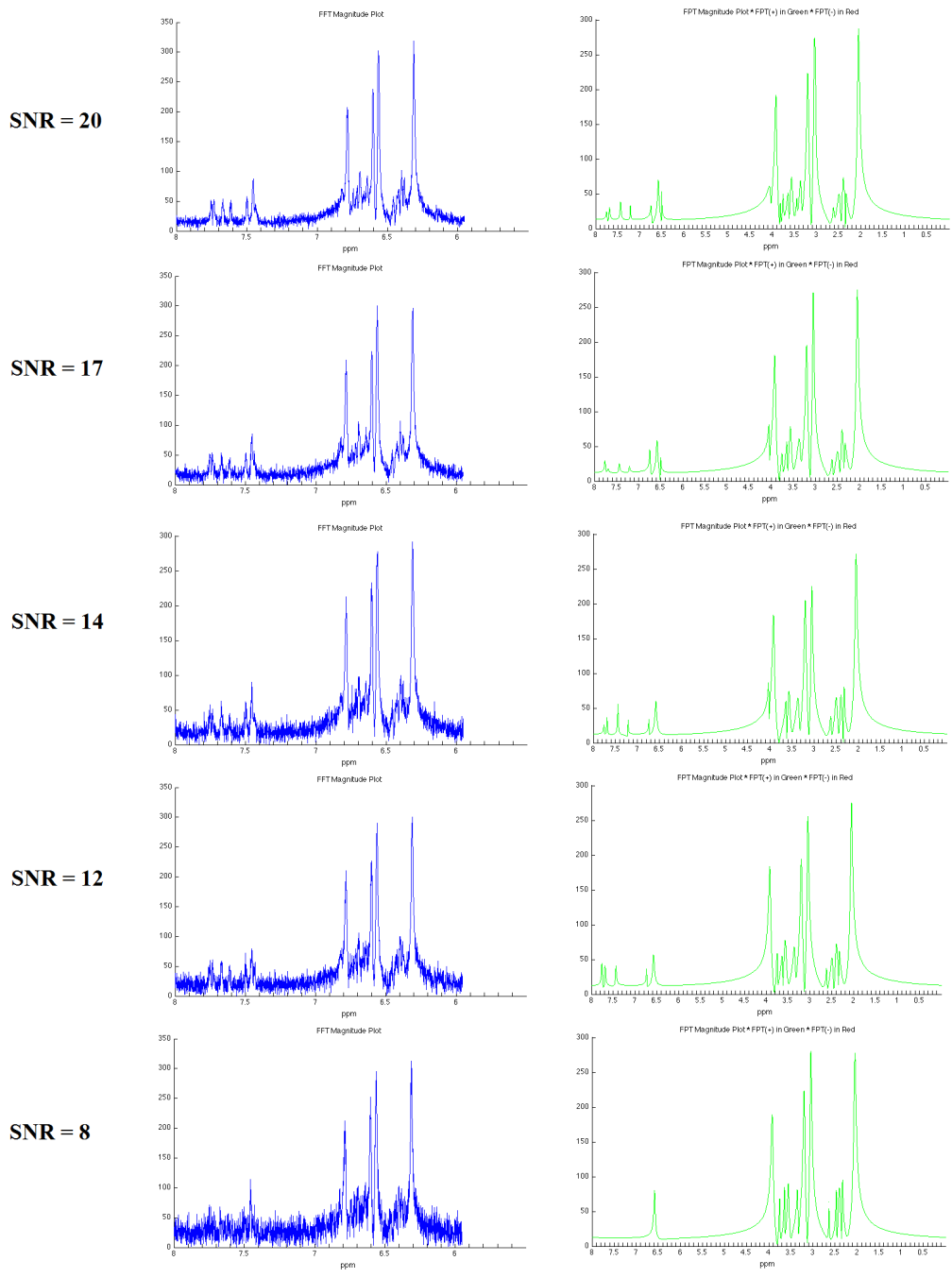


Figure 7-5: FPT algorithm measurement percentage errors using simulated brain MR spectra at 3 T with TE 30 PRESS pulse sequence.

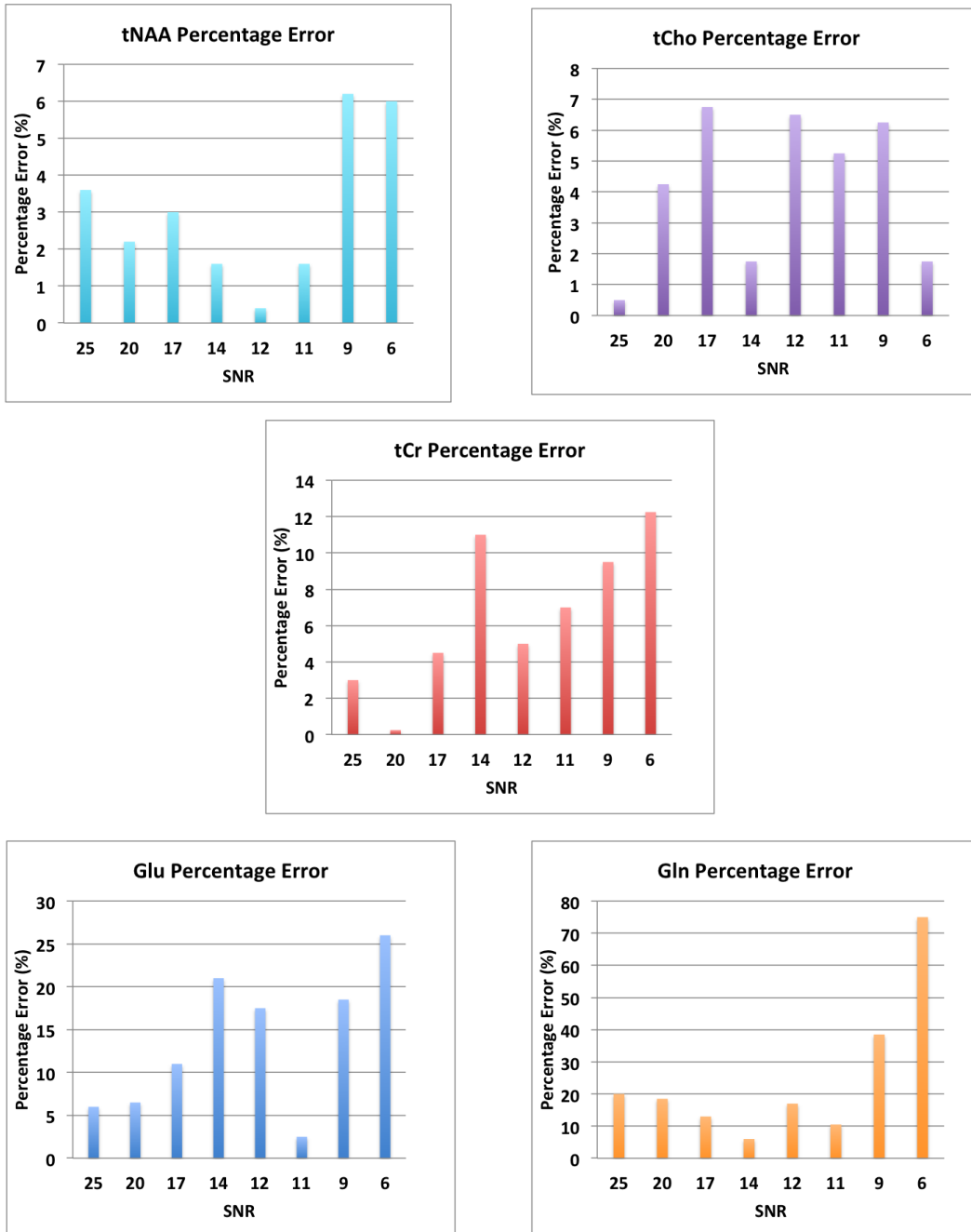


Figure 7-6: FPT algorithm measurement percentage errors using simulated brain MR spectra at 3 T with TE 30 PRESS pulse sequence.

### Validation with Phantoms

The measurement accuracy of the FPT algorithm was also tested in five phantoms. The first phantom is a “Braino” phantom (GE Medical Systems, Milwaukee, WI, USA), containing

12.5 mMol of NAA, 10 mMol of Cr, 3 mMol of Cho, 7.5 mMol of myo-inositol, 12.5 mMol of Glu, 5 mMol of Lactate, 0.1% of sodium azide, 50 mMol of potassium phosphate monobasic, and 56 mMol of sodium hydroxide. The other four phantoms contain GABA at concentrations of 4, 8, 12, and 20 mMol. The Braino phantom was studied using the TE 30 ms PRESS acquisition on a 3 T Siemens MAGNETOM Tim Trio system (TR = 3000 ms, TE = 30 ms, 128 averages, 15x15x15 mm<sup>3</sup>, 4:17 min runtime, 12-channel phased array head coil, automatic shimming). The GABA phantoms were studied with the MEGA-PRESS sequence (TR = 2500 ms, TE = 1/2J= 68 ms, 128 averages, 15x15x15 mm<sup>3</sup>, 8:34 min runtime, 12-channel phased array head coil, automatic shimming). Figure 7-7 shows the metabolite concentration values measured by the FPT algorithm in Braino phantom and Figure 7-8 shows the GABA concentrations measured also by the FPT algorithm in four different phantoms. The FPT measured concentrations values in all five phantoms have shown good agreements with the actual phantom values with the exception of the Glu and Myo measurements.

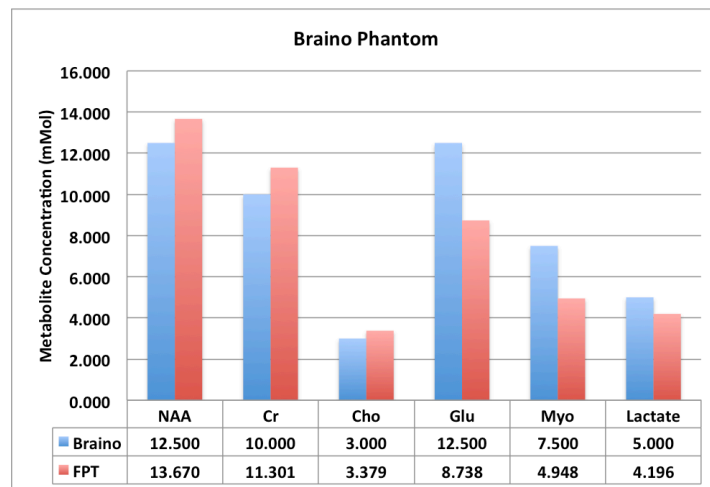


Figure 7-7: FPT measured metabolite concentrations in Braino phantom.

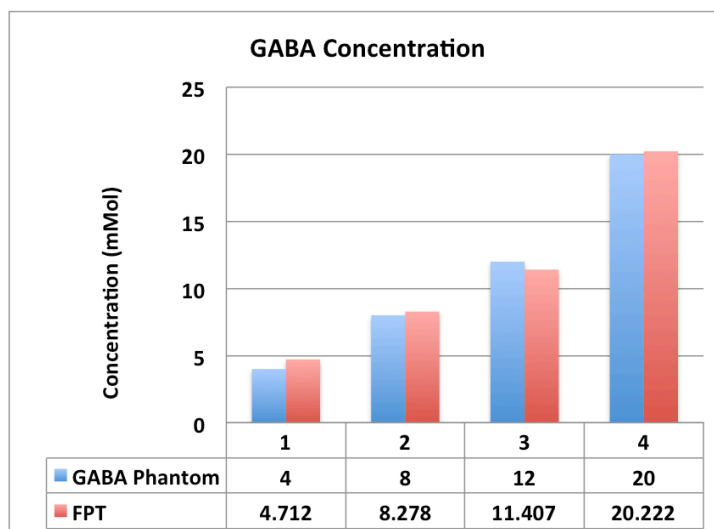


Figure 7-8: FPT measured GABA concentrations in four phantoms with 4 to 20 mMol of GABA.

## Comparison with LCModel

In this study, we compare the fast Padé transform method to the LCModel method using *in vivo* human brain data to evaluate its feasibility. MRS data were collected on a Siemens 3T MAGNETOM Allegra system. A single channel transmit and receive head coil was used to collect data. PRESS sequence (TE=30 ms, TR=2000 ms, Voxel size=12x20x18 mm<sup>3</sup>, Vector size=4096, NEX=128) was used to obtain both water reference (NWS) and metabolite spectra (WS). A total of 24 data sets were collected from the anterior cingulate cortex region in human volunteers (shown in Figure 7-9). Data were exported as Siemens RDA file format. MRS data were fed through the in-house built FPT program to obtain metabolite signal amplitude information. Three major metabolite concentrations (tNAA, tCr, and tCho) were chosen and calculated to compare with values output from the LCModel. An example of Padé shape component spectrum with individual signal peaks is shown in Figure 7-10. The mean and standard deviation of tNAA, tCr, and tCho concentrations from LCModel and FPT are listed in the Figure 7-11. The mean concentration values acquired from FPT method were higher than

those of LCModel, and it also has higher standard deviations than LCModel. The NAA standard deviation across 24 data sets is the highest. We found that although the FPT method has higher standard deviations in calculation of the concentrations, the mean concentration values are very close to the LCModel values. Pearson and Spearman correlation tests didn't show good linear or monotonic relationships between LCModel and FPT. And the Wilcoxon rank-sum test and the paired t-test revealed no significant statistical differences between the two methods. In addition, Bland-Altman correlation tests suggest a systematic concentration-dependent difference between the two methods. All together these findings indicate FPT can be used in place of LCModel for metabolite concentration quantification and the performance of the two methods is very similar.

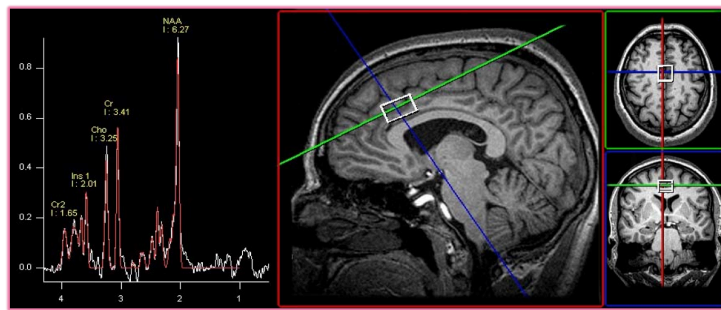


Figure 7-9: Single voxel PRESS acquisition at the AC region and the proton MR spectrum (left).

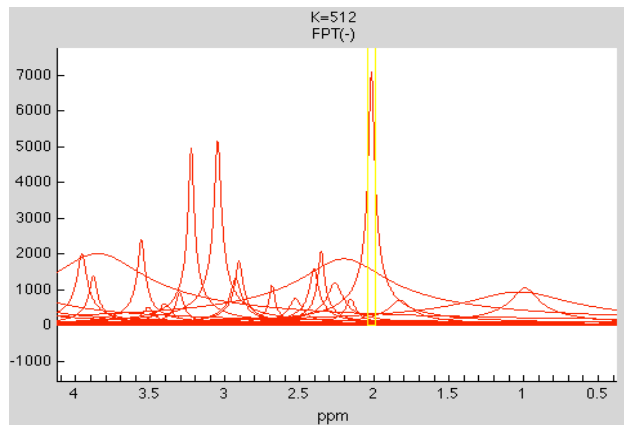


Figure 7-10: An example 3T TE 30 PRESS in vivo Padé component shape spectrum generated by the FPT algorithm, showing the NAA (highlighted in yellow) signal at 2.01 ppm, Glx signals at 2.1-2.5 ppm, Cr at 3.01 ppm and Cho at 3.2 ppm and Myo-Inositol at 3.55 ppm.

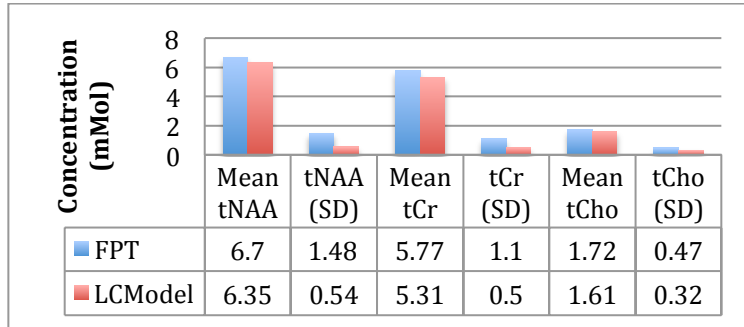


Figure 7-11: Comparison between FPT and LCModel measured mean concentration values for total NAA, total Cr and total Cho.

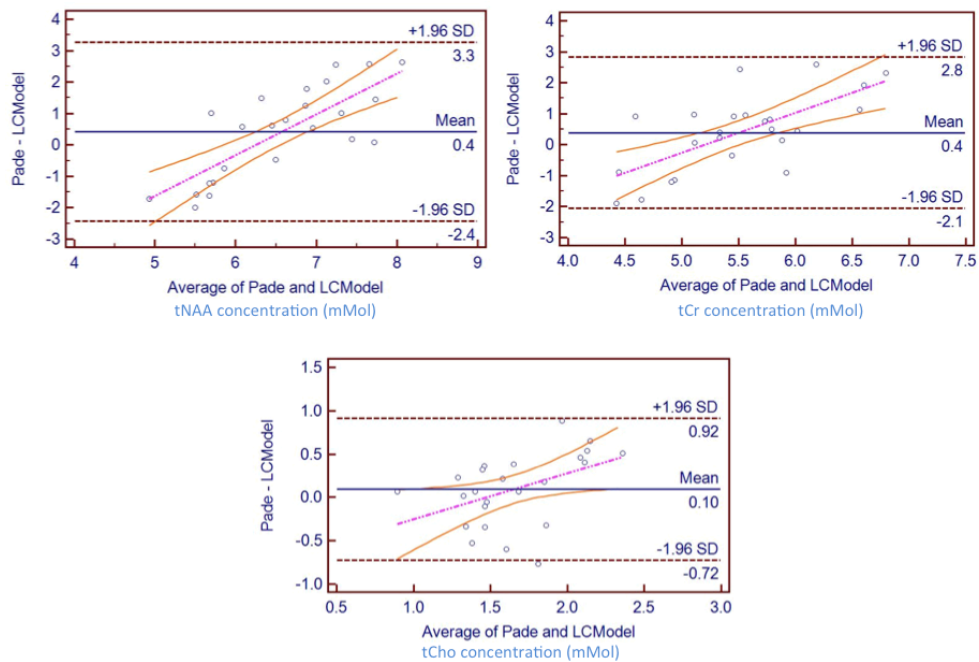


Figure 7-12: Bland-Atman correlation test between the FPT algorithm and LCModel.

## Glutamate, Glutamine, and GABA

Ten *in vivo* human brain MRS data were collected with TE 30 PRESS method on a Siemens 3 T MAGNETOM Allegra system. Glu and Gln concentrations were quantified using the FPT algorithm by identifying the Glu 2.34/2.35 methylene resonance peaks and the Gln 2.43/2.46 methylene resonance peaks manually. The results are shown in Figure 7-13 for Glu and Figure 7-14 for Gln. Measurements of the Glu concentration *in vivo* with the FPT algorithm

are significantly different from results of LCMoel ( $p=0.0015$  with t-test). Measurements of the Gln concentration with the FPT algorithm are not significantly different from LCMoel ( $p=0.39$  with t-test). These findings agree with both simulation and phantom studies. The FPT algorithm is not a reliable method to quantify Glu and Gln signals by identifying only a couple of the resonance peaks.

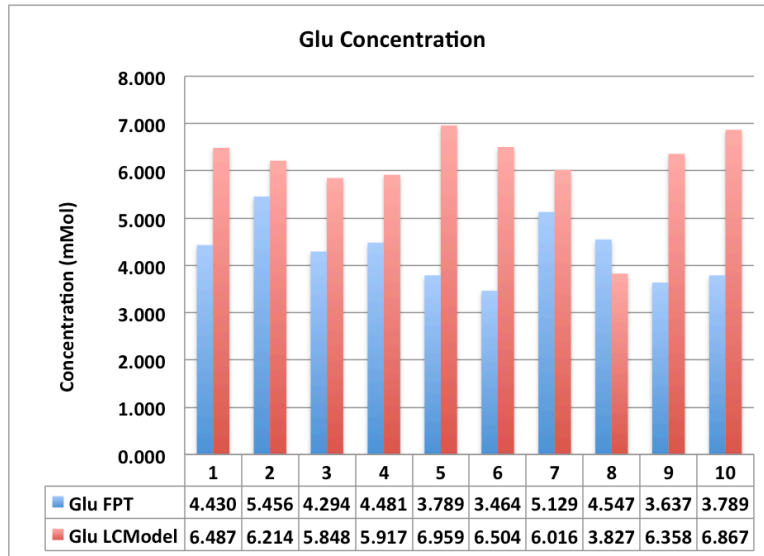


Figure 7-13: FPT measured Glu values across ten healthy subjects.

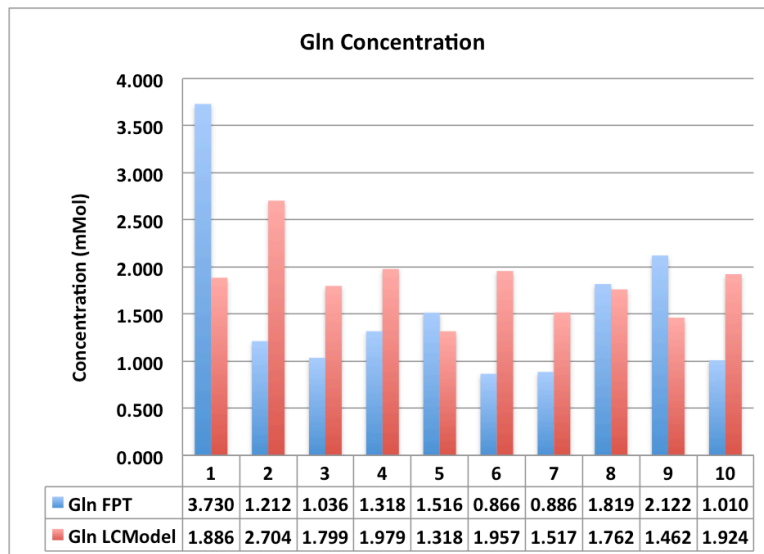


Figure 7-14: FPT measured Gln values across ten healthy subjects.



We also evaluated whether the FPT algorithm could be an accurate quantifying technique for edited spectra. Single voxel MEGA-PRESS (3 T Siemens Tim Trio, TR = 2000 ms, TE = 1/2J= 68 ms, 128 averages, 20x30x40 mm<sup>3</sup>, 8:34 min runtime, 12-channel phased array head coil, automatic shimming) acquisition was obtained in ten healthy adult human in the anterior cingulate (AC) region. Figure 7-15 shows an example of a Padé component shape spectrum generated by the FPT program. This spectrum was obtained using the *in vivo* human brain MEGA-PRESS acquisition and is the J-difference spectrum produced by subtracting the ‘edit-on’ spectrum from the ‘edit-off’ spectrum. The GABA doublet signals situated at 3.0 ppm are depicted in red. All other metabolite signals are depicted in grey (NAA is highlighted in yellow). The two doublet signals in red represent C-4 methylene group in the GABA molecule. FPT algorithm automatically calculates the signal amplitudes for these doublet signals as well as the water proton resonance signal. Figure 7-16 shows the GABA concentration levels measured by the algorithm in all ten human subjects. The mean and the standard deviation of the FPT measured GABA concentrations *in vivo* are 1.79 mMol and 0.25 mMol. The mean and the standard deviation are 1.5 mMol and 0.22 mMol for the LCModel measurements and 2.49 mMol and 0.36 mMol for the peak integration measurements. The inter-subject CV values for all three methods are 14.2% for FPT algorithm, 14.4% for peak integration, and 14.6% for LCModel (Table 7-2).

	<b>FPT</b>	<b>LCModel</b>	<b>Peak</b>
	<b>(mMol)</b>	<b>(mMol)</b>	<b>Integration</b>
			<b>(mMol)</b>
<b>Mean</b>	1.79	1.5	2.49
<b>S.D.</b>	0.25	0.22	0.36
<b>C.V.</b>	14.2%	14.4%	14.4%

**Table 7-2: Summary of the mean, standard deviation, and coefficient of variation values for the MEGA-PRESS GABA quantification made by the FPT, LCModel, and Peak Integration methods.**

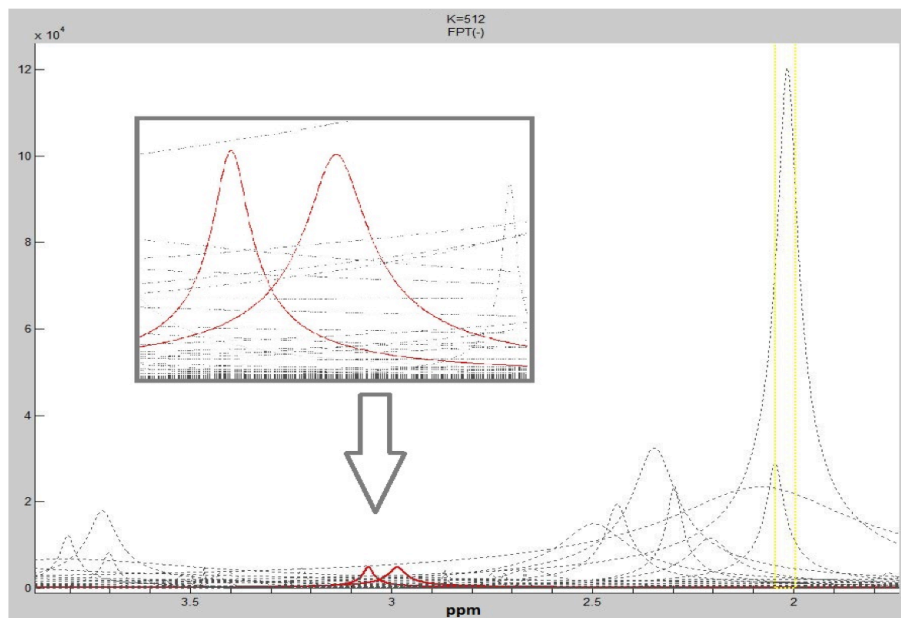


Figure 7-15: An example of the Padé shape spectrum of an in vivo J-difference spectrum.

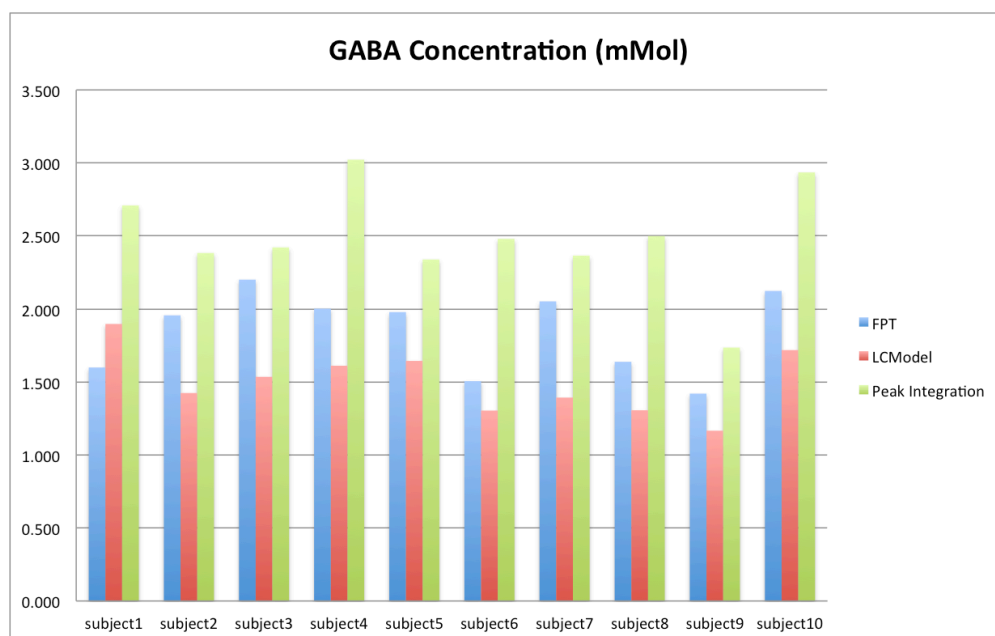


Figure 7-16: GABA concentration values measured by the FPT algorithm (blue) in comparison with values measured by LCModel (red) and Peak Integration (green).

## Conclusions

A method based on the Padé approximant is described and investigated in this chapter for the analysis of *in vivo*  $^1\text{H}$ -MRS signals. The goal was to apply the in-house build FPT algorithm to measure metabolite concentration values by quantify metabolite resonance peak amplitudes. The FPT algorithm with Froissart doublet denoising is a completely different procedure compared to the traditional Fourier transform for analysis and visualization of MRS data. We have demonstrated that the FPT algorithm offers an alternative parametric quantification technique that is capable of estimating metabolite concentrations. We have shown that the FPT algorithm is capable of quantifying resonance peaks of GABA, tNAA, tCr, and tCho with good agreement to the LCModel method, but there is no indication that FPT produces more accurate or precise concentrations. Performance of the FPT algorithm for Glu and Gln quantification was inferior to LCModel quantification. This is because only one of the many Glu or Gln signals was used in the FPT method while LC model uses signals from the entire molecule. An alternative design of the algorithm should be considered to include more resonance peak information for the amplitude calculation of Glu and Gln and a more automatic workflow should also be implemented to assign peak information to emolliate human errors and workload.

## References

- Belkić, D. (2001). Fast Padé transform for magnetic resonance imaging and computerized tomography. *Nuclear Instruments and Methods in Physics Research Section A: Accelerators, Spectrometers, Detectors and Associated Equipment*, 471, 165-69.
- Bessis, D. (1996). Padé approximations in noise filtering. *Journal of Computational and Applied Mathematics*, 66, 85-88.
- Dževad, B. (2006). Exact quantification of time signals in Padé-based magnetic resonance spectroscopy. *Physics in Medicine and Biology*, 51, 2633.

- Higinbotham, J., & Marshall, I. (2001). NMR lineshapes and lineshape fitting procedures. In *Annual Reports on NMR Spectroscopy* (Vol. Volume 43, pp. 59-120): Academic Press.
- Maltempo, M. M. (1986). Rational function approximations to generalized spectroscopic lineshapes and applications to electron paramagnetic resonance. *Journal of Magnetic Resonance*, 68, 102-11.
- Provencher, S. W. (1993). Estimation of metabolite concentrations from localized in vivo proton NMR spectra. *Magn Reson Med*, 30, 672-9.
- Roberts, D. E., Wu, Y. Z., Yusaf, R., Higinbotham, J., Shand, A. J., & Malcolm, I. C. (1997). New Form of Rational Function in NMR Lineshape Fitting: Application to Four Overlapping Resonances from a Three-Spin System. *Magnetic Resonance in Chemistry*, 35, 468-76.
- Williamson, D. C., Hawesa, H., Thacker, N. A., & Williams, S. R. (2006). Robust quantification of short echo time <sup>1</sup>H magnetic resonance spectra using the Pade approximant. *Magn Reson Med*, 55, 762-71.